Dependence of the Mechanical Behavior of Alloys on Electron Work Function—A
Promising Alternative Parameter for Materials Characterization and Design

by

Hao Lu

A thesis submitted in partial fulfillment of the requirements for the degree of

Doctor of Philosophy

in

Materials Engineering

Department of Chemical and Materials Engineering
University of Alberta

Abstract

With rapid advance in materials technology, structural material design has been required to rely on more fundamental principles. Conventional metallurgical rules have been successfully used in materials design for centuries but limitations are still there. Many expensive and time-consuming trial-and-error experiments are needed before a new material is successfully developed. It is known that the intrinsic mechanical behavior of metallic materials is largely governed by their electron behavior, which determines the atomic bond strength. Great effort has long been made to correlate mechanical properties of materials to their electron configurations based on quantum mechanics. However, the quantum theory of materials is complicated and not easily applied by materials engineers for materials design. Thus, it is highly desired to have a simple and fundamental parameter, which can largely reflect or characterize the electron behavior and can be easily used by materials developers to guide material design on a feasible electronic base.

Recent studies have shown that electron work function (EWF) is such a promising parameter. There has been growing interest in both experimental and theoretical investigation of the relationship between EWF and mechanical deformation of materials. Since EWF is related to many mechanical properties of

metals, it is desired to use EWF as an alternative parameter to guide designing and tailoring metallic materials on a feasible electronic base.

In this study, attempts are made to establish relationships between EWF and mechanical properties of metallic materials. EWF may reflect the depth of the potential well of electrons approximately. EWF reflects the stability of an electron state or the difficulty to break an atomic bond. A greater energy is required to change its electron state if the material has a higher EWF. This consequently generates higher barriers to any attempt to change its mechanical state, which are related to the electron state-governed atomic bond strength. Clear correlations between EWF and mechanical properties of materials, including pure metals, solid solution alloys and multi-phase alloys, have been shown experimentally and theoretically. Studies have demonstrated that the overall mechanical behavior is correlated with the overall EWF to a certain degree, although the former is microstructure dependent.

A method to extract the EWFs of binary solid solutions from their phase diagrams is proposed. And a single-parameter model using EWF as an indicator to evaluate the capability of solute atoms in solid solution hardening is suggested. An approach of using EWF as an indicator in evaluating fracture toughness and interfacial bonding strength of materials is also investigated. It demonstrates that

EWF could be used as a guiding parameter for material characterization and design. This parameter is promising to build a bridge towards the development of alternative or complementary approaches or methodologies for materials design on a feasible electronic base.

Preface

Results presented in Chapter 3 of this thesis have been published as Hao Lu and Dongyang Li, "Correlation between the electron work function of metals and their bulk moduli, thermal expansion and heat capacity via the Lennard–Jones potential," Physica Status Solidi (b) 251 (2014) 815-820.

Results presented in Chapter 4 of this thesis have been published as (1) Hao Lu, Xiaochen Huang, and Dongyang Li, "Understanding the bond-energy, hardness, and adhesive force from the phase diagram via the electron work function," Journal of Applied Physics 116 (2014) 173506. (2) Hao Lu, Guomin Hua, and Dongyang Li, "Dependence of the mechanical behavior of alloys on their electron work function—An alternative parameter for materials design," Applied Physics Letters 103 (2013) 261902.

Results presented in Chapter 6 of this thesis have been published as Hao Lu, Ziran Liu, Xianguo Yan, Dongyang Li, Leo Parent, and Harry Tian, "Electron work function–a promising guiding parameter for material design," Scientific Reports 6 (2016) 24366.

Results presented in Section 7.1 of this thesis have been accepted as Hao Lu, Chenxin Ouyang, Xianguo Yan, Jian Wang, Guomin Hua, Reinaldo Chung, and Dongyang Li, "Potential application of electron work function in analyzing fracture toughness of materials," Journal of Materials Science and Technology (2017). Dr. Chenxin Ouyang measured Young's modulus of the samples. Dr. Xianguo Yan and Dr. Jian Wang measured toughness of the samples and observed the sample surface

morphology. Dr. Guomin Hua proposed the Young's modulus model. Dr. Reinaldo Chung participated in the discussions and provided technical consultation.

Results presented in Chapter 8 of this thesis have been published as Jian Wang, Hao Lu, Bin Yu, Rongfeng Wang, Guomin Hua, Xianguo Yan, Leo Parent, Harry Tian, Reinaldo Chung and Dongyang Li, "Explore the electron work function as a promising indicative parameter for supplementary clues towards tailoring of wear-resistant materials," Materials Science and Engineering: A 669 (2016) 396-402. I was responsible for EWF measurements and EWF-related discussions in this paper. Dr. Jian Wang fabricated the samples, did the wear tests and composed the manuscript. Dr. Bin Yu assisted with the wear tests. Dr. Rongfeng Wang measured the toughness of the samples. Dr. Guomin Hua proposed the toughness model. Dr. Xianguo Yan, Leo Parent, Dr. Harry Tian and Dr. Reinaldo Chung participated in discussions and provided technical support.

I was responsible for fabricating samples, performing experimental tests, analyzing data, proposing theoretical models and composing manuscripts for the first five papers. Dr. Guomin Hua and Dr. Ziran Liu performed first-principles simulations in the papers presented in Chapter 4 and Chapter 6. Xiaochen Huang assisted with the data collection for the Journal of Applied Physics paper in Chapter 4. Dr. Xianguo Yan, Leo Parent, and Dr. Harry Tian participated in discussions and provided technical assistance and consultation for the paper in Chapter 6. Professor Dongyang Li contributed to data analysis and manuscripts revisions for all papers. All the research was conducted under Professor Dongyang Li's supervision.

Acknowledgement

I want to thank my supervisor, Dr. Dongyang Li, who gave me the opportunity to pursue my doctoral study. I gratefully appreciate his guidance, encouragement and valuable suggestions during my whole graduate study.

I also want to thank the committee members, who made comments and suggestions on my thesis.

I would also like to say thanks to all of my colleagues in Dr. Dongyang Li's group. I had the pleasure of working over the years with them. Thanks to Dr. Guomin Hua, Dr. Ziran Liu, and Dr. Lei Li for their collaborations in simulations studies. Thanks to Dr. Xinhu Tang, Dr. Ning Fu and Dr. Meisam Nouri for their assistances in my first year in Canada to help me get familiar to the life and research in University of Alberta.

I would also like to thank my parents for their support, thank my wife, who encourages and inspires me every day.

Table of Contents

List of Tables

List of Figures

List of Symbols

a	Lattice constant
b	Burgers vector
B	Bulk modulus
c	Concentration of solute
c_{11}, c_{12}, c_{44}	Elastic constants
C	Capacitance
C_v	Heat capacity
D	Dipole barrier potential
e	Elementary charge
E	Young's modulus
E_{abs}	Absolute electrode potential
E_{vacuum}	Vacuum level energy
E_F	Fermi level energy
F	Spring force
G	Shear modulus
H	Hardness
K	Spring constant
$\tilde{K}$	Bulk modulus
k_B	Boltzmann constant
K_{Ic}	Stress intensity factor
M	Mass of electron
n	Equilibrium valence electron density
N_v	Crack density

p	Lattice site occupation probability
r_e	Equilibrium distance between two adjacent atoms
r_s	Wigner-Seitz radius
T	Temperature
T_D	Debye temperature
U	Total energy of a crystal
z	Number of valence electron
α	Madelung constant
α_L	Linear thermal expansion coefficient
β	brittleness
γ	Surface energy
σ	Stress
σ_y	Yield strength
ε	Strain
ε_b	Bond energy
ε_0	Vacuum dielectric constant
ε_r	Relative dielectric constant in air
$\hbar$	Planck's constant
μ	Bulk chemical potential
υ	Poisson's ratio
φ	Electron work function
$\Delta\varphi_M^{EI}$	Potential drop at the metal/liquid surface

χ_s Surface potential of the liquid surface

ψ^M, ψ^S Volta potentials outside the metal and outside the solution

ω_D Debye frequency

List of Abbreviations

AFM   Atomic Force Microscope

CPD   Contact Potential Difference

CPS   Count Per Second

DFT   Density Functional Theory

EDX   Energy Dispersive X-ray Spectroscopy

ELF   Electron Localization Function

EWF   Electron Work Function

HCCI   High Chromium Cast Iron

KP   Kelvin Probe

KPFM   Kelvin Probe Force Microscope

MEMS   Microelectromechanical System

MFM   Magnetic Force Microscopy

SEM   Scanning Electron Microscope

SKP   Scanning Kelvin Probe

UPS   Ultraviolet Photoelectron Spectroscopy

XRD   X-ray Diffraction

Chapter 1 Introduction

As materials science is developing rapidly, more fundamental guidelines are highly desired for effective design of structural materials. Pure metals are generally either too soft, brittle or chemically reactive for practical use. Thus, alloying with elements to modify the properties of pure metals for desired characteristics is necessary. Conventional metallurgical rules have been successfully used in materials design for centuries but limitations are still there. Many expensive and time-consuming trial-and-error experiments are needed before a new material is successfully developed. With technological advances, it has been possible to develop more fundamental approaches for advanced materials design with higher accuracy and efficiency. It has long been a dream to design structural materials based more on the electron behavior, since the mechanical property of a material is essentially governed by electronic interactions. However, the electronic theory of materials is complicated and not easily applied by materials engineers for materials design. Thus, it is highly desired to have a simple and fundamental parameter, which can largely reflect or characterize the electron behavior and can be easily used by materials developers to guide material design on a feasible electronic base.

It is known that materials generally consist of multiple elements, phases and interphase boundaries in order to obtain an optimal combination of various desired properties. However, during metallurgical processes, different elements may react and form not only desired phases but also others which result in side effects. In some cases, it is difficult to tell which phases are desired or undesired in order to control materials design. Although X-ray diffraction (XRD) and electron

microscopy have a great power to characterize microstructures, data obtained does not provide simultaneous information on properties of individual phases and interfaces. New characterization techniques for analyzing mechanical properties of materials and identifying desired and undesired phases as well as interfaces are highly wished in order to help design advanced structural materials more efficiently.

It has long been recognized that the mechanical property of a material is governed by the electronic behavior of the material and empirical correlations between the electron number [1] or the electron to atom ratio [2] and mechanical properties of metallic systems have been established. These relationships demonstrate that the electron number and electron density are useful parameters for rationalizing the effect of solute additions and guiding materials design. However, these relationships are too rough and lack solid theoretical foundations. So they generally serve as the conceptual base for studying the mechanical properties of the metallic system. Nowadays, many studies are focused on computational materials design, using simulation methods, such as molecular dynamics and density functional theory, to correlate properties of materials to their electronic behavior. They have shown strong capability in understanding materials properties and explaining the mechanism. However, it is still hard to use the simulations in materials design, especially for structural materials, due to the lack of quantitative relationships between the electron behavior and overall properties.

During the last three decades, there has been growing interest in both experimental and theoretical investigation of the relationship between electron work function (EWF) and mechanical deformation [3-8] due to the wide application of the Kelvin probe (KP) technique [9]. EWF is defined as the minimum energy needed to

remove an electron from a solid to a point in the vacuum just outside the solid surface. It equals the difference in potential energy of an electron between the vacuum level and Fermi level [10]. EWF may reflect the depth of the potential well of electrons approximately. Many studies were also conducted in our group in the past fifteen years to investigate the correlation between EWF and mechanical properties of metals. For example, it has been demonstrated that EWF is a sensitive parameter to characterize elastic and plastic deformation [11-14], adhesion behavior of the material's surface [15], tribology phenomena [16,17], friction [18-21], *etc*. Since EWF is related to many mechanical properties of metals, it is expected that EWF can be used as an alternative parameter to design and tailor metallic materials on a feasible electronic base. However, although we have collected a large body of experimental data, the lack of established theoretical relationships between EWF and mechanical properties still hinders the application of using EWF as a simple and alternative parameter to design and tailor materials.

The objectives of this research are (1) demonstrating the relationships between EWF and properties, especially mechanical properties, of metallic materials (2) developing a new characterization technique based on EWF for analyzing mechanical properties of materials (3) applying the proposed characterization technique and the relationships between EWF and properties of materials in designing materials. The research is focused on exploration and application of EWF in materials characterization and design. It is expected to establish a new EWF-based materials characterization and design method.

This thesis comprises four parts which are organized in the following structure:

Chapter 1 and Chapter 2 present a brief introduction to the background of materials design research and relevant investigations of EWF. These two chapters provide an overview of methods used in materials design and applications of EWF.

Chapter 3 to Chapter 6 report the studies of relationships between EWF and mechanical properties of metallic materials, including pure metals, binary solid solutions or single phase alloys and multi-phase alloys. These studies demonstrate that EWF is a promising parameter which provides supplementary clues for element selection and materials tailoring.

Chapter 3 presents the study of using the Lennard-Jones potential as a bridge to correlate properties of pure metals with their EWFs. The approach is applied to several properties of metallic materials, including bulk modulus, thermal expansion and heat capacity (Debye temperature). It verifies the dependence of the properties on EWF, which helps generate complementary information for advanced material design, element selection and modification of bulk materials or phases based on EWF on a feasible electronic base.

Chapter 4 reports studies in binary solid solutions or alloys. A method is proposed first to extract EWFs of binary solid solutions or alloys from their phase diagrams. This simple approach is used to predict their mechanical strength and surface properties, such as adhesion. Using isomorphous nickel-copper alloys as an example material without involving microstructure complexity, it also demonstrates that there is clear correlation between EWF and Young's modulus as well as hardness of the alloy with respect to the composition. This chapter demonstrates that EWF could be used to guide element selection for effective solid solution

hardening practice.

Chapter 5 reports a study on the conventional solid solution hardening models and proposes a EWF based approach to guide selection of appropriate alloying elements for solution hardening. The proposed single-parameter model using EWF as an indicator simplifies solute selection with clearer selection criteria than the traditional models.

Chapter 6 reports a study of the correlations between EWF and mechanical properties of multi-phase alloys. The changes in Young's modulus and hardness show trends similar to that of the change in EWF no matter whether or not the second phase is present. The similar trends suggest that the overall mechanical behavior is correlated with the overall EWF to a certain degree, although the former is microstructure dependent.

Chapters 7 and 8 demonstrate the potential of EWF in materials characterization. Chapter 7 reports two studies of EWF applications in materials characterization, *i.e.*, evaluating fracture toughness of hard metallic materials and analyzing interfacial bonding strength. Chapter 8 presents a case study of EWF applications in materials characterization and design in high chromium cast irons fabrication.

Finally, Chapter 9 provides an overall summary of EWF applications in materials characterization and design. Areas for future studies are also discussed in this chapter.

Chapter 2 Literature Review

This chapter provides a literature review regarding material design and EWF, including two parts. The first part provides a brief introduction to conventional metallurgical rules in materials development and relevant studies in materials design methods based on electronic theories. Some computational materials design methods are also discussed. The second part reviews the studies related to EWF. Definition and measurement methods of EWF, relationships between EWF and other properties and some applications of EWF are discussed.

2.1 Materials Design

2.1.1 Conventional metallurgical rules in materials design

Materials are deep-seated in our culture and virtually every segment of our daily life is influenced by materials. The development and advancement of societies have been intimately tied to the ability to produce and manipulate materials. Early civilizations have been designated by the level of their material development, such as Stone Age, Bronze Age, and Iron Age [22]. The earliest humans had access to only a very limited number of materials which occur naturally, such as stone, wood, clay and skins. Gradually, people discovered techniques for producing materials with better properties than the natural ones and found that properties of materials could be altered by heat treatments and addition of other substances. Until recent centuries, people came to understand the relationships among the composition, structure and properties or performance of materials. Modern materials science involves studies

of the above-mentioned relationships. With the knowledge of chemical properties of elements and established phase diagrams, it has become a reality to design composition and microstructure, which is achieved through heat treatment and proper processing routes. Based on the conventional metallurgical rules, with optimized composition and heat treatment procedures, people can develop new materials having desired mechanical properties. However although conventional metallurgical rules have been successfully used in materials design and some new concepts have also been proposed, *e.g.*, metallic glasses [23], high entropy alloys [24], limitations are still there. Expensive and time-consuming trial-and-error experiments are generally needed before a new material is successfully developed without sufficient understanding of materials properties from a more fundamental physics aspect.

2.1.2 New materials design approaches based on electron interactions

Material properties are fundamentally determined by the electron behavior that governs the atomic bond strength and ultimately the overall mechanical properties [10]. Thus, it always desired to design structural materials using more fundamental approaches and based on the electron behavior.

2.1.2.1 Early studies in electron interaction-based material design

It has been recognized that material properties are fundamentally determined by the electron behavior since the beginning of the 20th century, and analyzed based on quantum mechanics. However, quantum mechanics is only useful in practice for simple systems due to the theoretical complexity when dealing with the many-body quantum effect [25]. It is difficult to apply quantum mechanics in material design. Thus, most of the early studies were conducted to correlate material properties to some parameters which are related to the electron behavior. In the 1950s, people started to realize that the valence number of solute atoms played an important role in solution hardening [1,26]. Another widely studied parameter is the ratio of the electrons to atoms or the electron concentration [2,27]. Hume-Rothery pointed out the importance of this parameter in controlling the phase stability in binary alloys [27]. Since then studies were conducted to investigate the relationships between this parameter and many physical properties of materials [2], such as the formation of defect phases, stacking fault energy, flow stress, elastic constant, *etc*. Figure 2.1 illustrates the correlation between the ratio of the electrons to atoms and elastic constants. An approximate linear relationship is demonstrated in Figure 2.1. The empirical correlations between the physical properties of materials and electron to atom ratio may be used to tailor material compositions in order to optimize the desired properties. However, due to the lack of theoretical analysis and sound models, the correlations generally serve as the base of first-principles simulations, instead of being directly used in materials design.
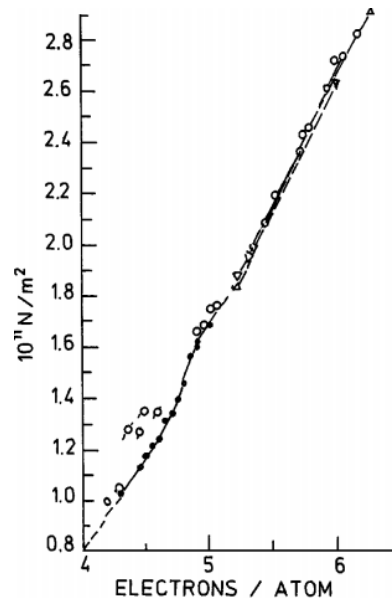
Figure 2.1 Composition dependence of K for Zr-Nb-Mo-Re and Nb-Ti, Nb-Hf, Nb-W

alloys on the ratio of electrons to atoms. $K = 0.5(C_{11} + 2C_{12})$. C_{11} *and* C_{12} *are elastic*

constants [2]

2.1.2.2 Computational materials design

The development of modern materials science has led to a growing need to understand the properties of materials and processes on the atomistic level. Molecular dynamics simulation and first-principles simulation are widely used to calculate and understand the mechanical properties of materials [25,28]. Despite significant advances in computational materials science which helps us to understand mechanical properties of materials from a fundamental aspect based on the electron behavior, it is still difficult to predict mechanical properties of materials or design materials with desired properties [29] since the properties are determined by

both material intrinsic behavior and microstructure. In the middle of the 1960s and the early 1970s, a so-called genetic algorithm method was proposed and started to try to be used in material design at the beginning of the21[st] century [30]. The genetic algorithm is a biological inspired optimization method and has wide applications in data mining. If the living thing and its environment are replaced by an alloy and a design rule, respectively, it is expected that alloy design could be accomplished by a method similar to biological evolution. Natural selection occurs according to the living thing's properties during evolution. As for alloy design, a specific form of the alloys' gene, *i.e.,* a specific composition, is assumed in the genetic algorithm and properties of the alloy are simulated by a variety of simulation methods. Based on the specific design rules or property requirements, the desired materials are chosen. The basic idea and procedure of the genetic algorithm method in material design is described as follows. A set of alloys with different compositions are chosen randomly first and new alloys are created by letting the existing alloys undergo natural evolution in the sense of breeding between the alloys (interchanging randomly chosen elements from "parent alloys" to give birth to two "children alloys"), and mutation (changing one element to another randomly for the existing alloys). Selection of the fittest alloys to survive to the next generation is based on the design rules. The steps are repeated until a convergence criterion is fulfilled. It provides optimization of compositions of materials under a given design rule by evaluating physical quantities using simulation methods and making an efficient global search [31,32]. The so-called genetic algorithm method is tandem to molecular dynamics and first-principles simulations now in materials design. Ikeda attempted to design nickel based superalloys. He studied two highly complicated systems, Ni–Al–Cr–Mo–Ta and Ni–Al–Cr–Co–W–Ti–Ta alloys, and predicted the optimum

compositions based on the designing rules involving a large number of physical parameters [31]. By considering the enthalpy of formation as an index of stability, Johannesson *et al.* identified the 20 most stable alloys, containing four components, out of a total of 192016 possible configurations of 32 transition, noble, and simple metal elements [32]. These two pieces of work demonstrate the promising prospect of computational materials design. However, a highly versatile and robust algorithm that can be readily applied to one problem after another in the materials research areas still needs to be investigated [30]. Recently, high-throughput computational materials design is an emerging area of materials science [33]. It exploits the power of current supercomputers and combines advanced thermodynamics and quantum mechanics methods with intelligent data mining and database constructions. With the help of the high-throughput computational materials design method, people manage and analyze enormous data repositories for the discovery of novel materials in a more efficient way. The concept is simple: create a large database containing the calculated thermodynamic and electronic properties of existing and hypothetical materials, and then intelligently interrogate the database in the search of materials with the desired properties. The high-throughput computational materials design method is powerful, but it has high requirements on a high speed supercomputer, data storage and sharing, and data mining techniques, which still require investigation.

2.2 Overview on EWF

There has been growing interest in both experimental and theoretical investigations of the relationship between electron work function (EWF) and

mechanical properties of materials. It is expected to use EWF as an alternative parameter to design and tailor metallic materials on a feasible electronic base. This section provides an overview of studies in EWF.

2.2.1 Definition of EWF

In solid state physics, electron work function (EWF, sometimes shortened as work function, φ) is defined as the minimum energy needed to remove an electron from a solid to a point in the vacuum just outside the solid surface. It equals the difference in potential energy of an electron between vacuum level (E_{vaccum}) and Fermi level (E_F) [10]. The vacuum level is the energy of an electron at a point sufficiently far outside the surface so that the electrostatic image force may be neglected. The Fermi level is the electrostatic potential of the electrons in the solid[34]. EWF is a fundamental parameter that characterizes the electron behavior of materials, which depends on the chemical composition of the materials and the surface conditions. Chemical composition can be reflected by the bulk chemical potential (μ) of the materials and surface conditions influence the surface dipole barrier potential (D) [35]. Thus, EWF is expressed as Eq. (2.1).

$$\varphi = E_{vaccum} - E_F = -\mu + D \tag{2.1}$$

Figure (2.2) gives the physical meaning of EWF, which approximately reflects the shallowest potential well depth of electrons [15].
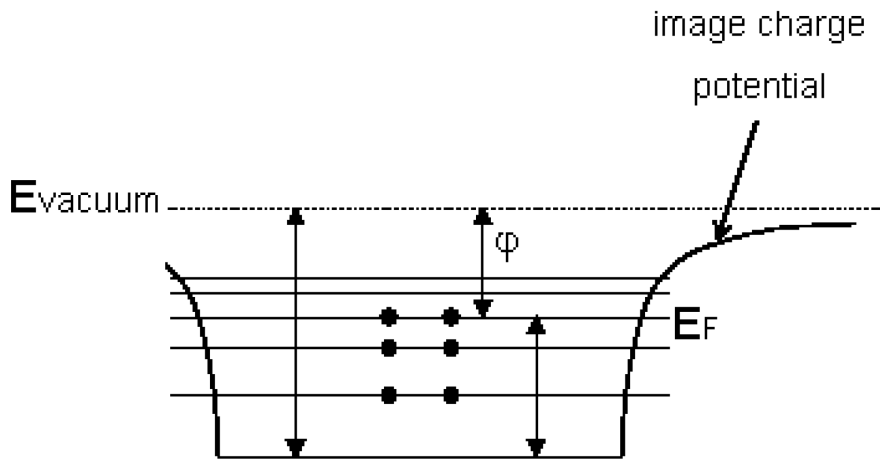
Figure 2.2 A schematic definition for EWF

EWF is sensitive to surface conditions, such as adsorption [36-39], surface composition and segregation [40,41], surface morphology, corrosion behavior [42,43], *etc*. Thus, EWF has been widely used to analyze surface chemical and physical phenomena [9]. Although EWF appears to mainly represent the behavior of electrons at the surface, it fundamentally characterizes the atomic interactions or the involvement of electrons in the electrostatic interaction between electrons and positively charged nuclei in a metal. Thus, EWF is a fundamental property that could be used to predict and evaluate the bulk properties of materials, including the mechanical behavior of metals [44, 45].

2.2.2 Theoretical analysis of EWF

Over the last century, EWF of a surface had been examined for almost all elements and many alloys as well as conducting compounds. However, EWF was not strictly defined and no theoretical models could precisely predict EWFs of

materials satisfactorily. At the beginning of the 20th century, it was assumed that the image force could be the main reason for the barrier at the metal surface and the main contribution to EWF. However, the distance from which image force could be integrated was not clear. Many proposed methods of calculating EWF dealt with its relations to other physical properties. Empirical formulas were established to correlate EWF to density, atomic weight, electronic valance and heat of sublimation[46]. In further development of solid state physics, greater emphasis was paid to the role of dipole layer [47] in EWF calculation. Some ab-initio studies, such as jellium model [48] and self-consistent Green's function technique [49], were proposed to calculate EWF. However, the nature of EWF was lost in complex and approximate calculations.

At the end of the 20th century or beginning of the 21st century, the idea of image potential as the main contribution to EWF was restored [50-52]. The distance from which the image force could be integrated was found from the length of spontaneous metallic plasma polarization. The method of image charges is a basic method for dealing with issues in electrostatics, in which certain elements in the original layout are replaced by the imaginary charges to replicate the boundary conditions of the problem. The EWF values obtained from this model were in good agreement with experimental data for polycrystalline surfaces of pure metals. This method is also effective in calculating EWF of conducting solids [53]. As expressed in Eq. (2.2), EWF is related to Fermi level and Wigner-Seitz radius (r_s) of the materials,

$$\varphi = \frac{\alpha}{r_s^{3/2} E_F^{1/2}} \qquad (2.2)$$

where α is a constant. Since both r_s and E_F are correlated to the electron density of the materials, EWF is determined by the electron density

$$\frac{4}{3}\pi r_s^3 = \frac{1}{n} \qquad (2.3)$$

$$E_F = \frac{\hbar^2}{2m}(3\pi^2 n)^{2/3} \qquad (2.4)$$

$$\varphi \propto n^{1/6} \qquad (2.5)$$

where m is the mass of electron, $\hbar$ is Planck's constant, n is the electron density

2.2.3 Measurement of EWF

The experimental methods for measuring EWF may be classified into two groups, absolute and relative [9]. Absolute measurements employ electron emission from the sample induced by photon absorption (photoemission), thermal energy (thermionic emission) or electric field (field emission), while, relative methods make use of the electric field created between the sample and a reference electrode to measure their contact potential difference (CPD).

Ultraviolet photoelectron spectroscopy (UPS) and scanning Kelvin probe (SKP) are commonly used to measure EWF of materials nowadays. UPS is a kind of

absolute method based on photoemission [54], as Figure 2.3 illustrates. Since the energy of ultraviolet light is relatively low, it can only emit valence electrons to reveal valence band structure and EWF of material without exciting core electrons. As illustrated in Figure 2.3 (b), the spectrum consists of three features. Fermi level is located at 0 eV binding energy and manifests itself as a step to separate occupied states and empty states. At low binding energy regions, valence band structure of the material is visible. Then the spectrum ends at the high binding energy cutoff. Electrons close to the cutoff edge are the slowest electrons which just have enough energy to overcome EWF of the material. Thus, EWF of the material can be determined by the energy difference between ultraviolet photons and the binding energy of the cutoff.
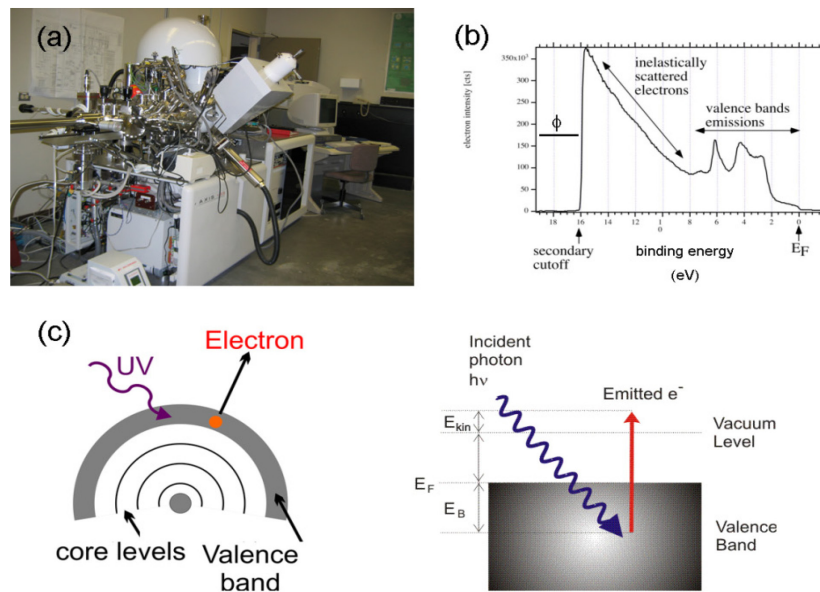
Figure 2.3 (a) A picture of UPS instrument (b) UPS experimental spectroscopy (c) UPS working principle, determines valence structure and work function by measuring kinetic energy of the emitted electrons

SKP is a relative method which measures the CPD between the sample and a reference electrode by forming a parallel plate capacitor between them [55,56], as illustrated in Figure 2.4. When two metals are in contact ($\varphi_1 > \varphi_2$), electrons of higher electrochemical potential in metal 2 will flow to metal 1 until the electrochemical potentials of the two metals are equal. Thus, metal 1 becomes more negative than metal 2 by an amount equal to the difference in EWF between the two metals. This potential is called the CPD and is defined by Eq. (2.6)

$$e \cdot V_{CPD} = \varphi_1 - \varphi_2 \tag{2.6}$$

where e is the elementary charge

The electric field between the sample and the reference electrode induces charges with opposite signs on two metals. Using an external voltage V_b, the induced charges can be adjusted to zero. Under this condition

$$V_{CPD} = -V_b \tag{2.7}$$

By maintaining EWF of the reference electrode as a constant and testing the CPD between sample and the reference electrode, SKP can measure the EWF of the samples. The CPD is highly dependent on the nature of the surfaces, surface cleanliness and surface roughness, *etc*. Thus, it is essential to make sure the samples' surface conditions are the same when using SKP to measure EWF of different materials for comparable results.
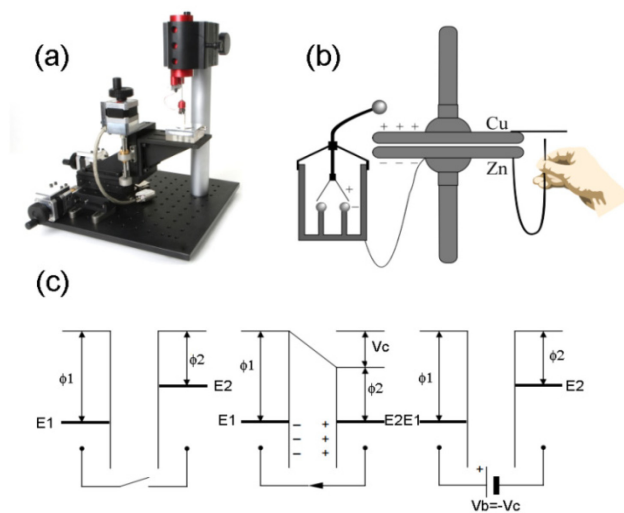
Figure 2.4 (a) A picture of SKP instrument (b) Original used apparatus (c) SKP working principle, CPD between sample and reference is determined by V_b

SKP determines the mean EWF of a surface and is not biased towards low EWF phases as in UPS experiments. The value of EWF measured by photoelectric emission gives a weighted mean that favors the phases of lower EWF [57]. Thus, the EWF of samples may not be compared appropriately if they are not measured using the same technique, especially for multiphase samples.

Recently, Kelvin probe force microscope (KPFM), a non-contact variant of atomic force microscope (AFM), has been developed [58]. It allows measuring EWF of surfaces at atomic or molecular scales to distinguish different phases in samples. Mapping of surface EWF and topography can be conducted simultaneously by KPFM. Figure 2.5 illustrates a typical KPFM image of a cast iron surface. It distinguishes carbides and matrix phases in cast iron by scanning surface topography and EWF simultaneously. As shown in Figure 2.5 (b), phases with

higher EWF are brighter than those with lower EWF.
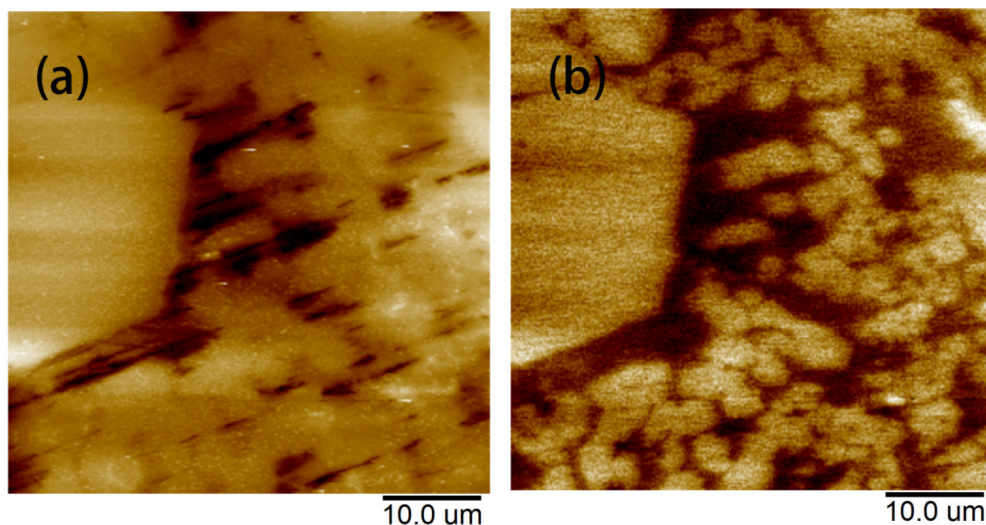
Figure 2.5 Typical KPFM images (a) cast iron surface topography (b) cast iron EWF map at the same area as topography image

2.2.4 Correlation of EWF with material properties

Since EWF is a fundamental electronic property of metallic materials, it is expected that EWF is correlated to physical and chemical properties of materials. It has been known that EWF correlates well with many atomic properties such as ionization energies and electronegativity [59]. It is reported that the ionization energy is approximately twice the value of EWF [47]. Many empirical relationships between electronegativity and EWF were also derived, which showed approximately linear relationships [60].

2.2.4.1 Periodicity of EWF

It is well recognized that EWF is a periodic function of the atomic number, like other chemical and physical properties of the elements [61]. The currently accepted EWF values of elements are given in Figure 2.6, which shows a well defined periodicity [47]. The periodicity of EWFs of elementary solids is similar to the periodicity of the electronic structure of the atoms. In each period of the table of elements, EWF values tend to rise with increasing atomic number as electron shells and subshells gradually become filled. In each group of the table, EWF values generally decease as atomic number increases. The periodicity becomes complex for transition metals somewhat. The sequence and periodicity of EWF is the basis for empirical relationships between EWF and many other atomic properties.

Each element cell lists: ionization energy (upper), EWF value (middle), electron affinity (lower), in eV/atom.

1	2	3	4	5	6	7	8	9	10	11	12	13	14	15	16	17	18
1H 13.598 / / 0.7542																	2He 24.58 / / −0.22
3Li 5.39 / 2.9 / 0.6182	4Be 9.32 / 4.98 / −0.19											5B 8.30 / 4.45 / 0.227	6C 11.26 / 5.0 / 1.2629	7N 14.54 / / −0.07	8O 13.61 / / 1.462	9F 17.42 / / 3.399	10Ne 21.56 / / −0.3
11Na 5.14 / 2.75 / 0.5479	12Mg 7.64 / 3.66 / −0.22											13Al 5.98 / 4.28 / 0.442	14Si 8.15 / 4.85 / 1.385	15P 10.55 / / 0.7464	16S 10.36 / / 2.077	17Cl 13.01 / / 3.615	18Ar 15.76 / / −0.36
19K 4.34 / 2.30 / 0.5015	20Ca 6.11 / 2.87 / 0.0215	21Sc 6.56 / 3.4 / 0.189	22Ti 6.83 / 4.33 / 0.080	23V 6.74 / 4.3 / 0.526	24Cr 6.76 / 4.5 / 0.667	25Mn 7.43 / 4.1 / <0.005	26Fe 7.90 / 4.5 / 0.164	27Co 7.86 / 5.0 / 0.662	28Ni 7.63 / 5.15 / 1.157	29Cu 7.72 / 4.51 / 1.228	30Zn 9.39 / 4.33 / 0.093	31Ga 6.00 / 4.15 / 0.31	32Ge 7.89 / 5.0 / 1.23	33As 9.81 / 4.77 / 0.81	34Se 9.75 / 5.9 / 2.0208	35Br 11.84 / / 3.364	36Kr 14.00 / / <0
37Rb 4.18 / 2.16 / 0.4859	38Sr 5.69 / 2.59 / 0.11	39Y 6.38 / 3.1 / 0.308	40Zr 6.95 / 4.05 / 0.427	41Nb 6.88 / 4.3 / 0.894	42Mo 7.18 / 4.6 / 0.747	43Tc 7.28 / 4.9 / 0.55	44Ru 7.36 / 4.71 / 1.05	45Rh 7.46 / 4.98 / 1.138	46Pd 8.343 / 5.12 / 0.558	47Ag 7.57 / 4.26 / 1.303	48Cd 8.99 / 4.22 / 0.260	49In 5.78 / 4.12 / 0.30	50Sn 7.34 / 4.42 / 1.15	51Sb 8.64 / 4.55 / 1.07	52Te 9.01 / 4.95 / 1.9708	53I 10.45 / / 3.059	54Xe 12.13 / / <0
55Cs 3.893 / 2.14 / 0.4716	56Ba 5.21 / 2.7 / 0.17	57La 5.57 / 2.96 / 0.518	72Hf 7.00 / 3.9 / ≥0.1	73Ta 7.89 / 4.25 / 0.323	74W 7.98 / 4.55 / 0.816	75Re 7.87 / 4.87 / 0.12	76Os 8.70 / 4.83 / 1.12	77Ir 9.0 / 5.27 / 1.566	78Pt 8.96 / 5.65 / 2.128	79Au 9.22 / 5.1 / 2.309	80Hg 10.43 / 4.49 / 0.186	81Tl 6.11 / 3.84 / 0.3	82Pb 7.41 / 4.25 / 0.364	83Bi 7.29 / 4.22 / 0.946	84Po 8.43 / 5.0 / 1.9	85At 9.64 / / 2.8	86Rn 10.74 / / <0
87Fr 3.98 / 2.1	88Ra 5.28 / 2.8 / 0.17	89Ac 5.17 / 3.2															

58Ce	59Pr	60Nd	61Pm	62Sm	63Eu	64Gd	65Tb	66Dy	67Ho	68Er	69Tm	70Yb
5.466 / 2.97 / 0.518	5.42 / 2.96 / ≥0.1	5.49 / 3.2 / ≥0.05	5.54 / 3.1	5.6 / 2.85 / ≥0.05	5.67 / 2.5 / ≥0.05	6.14 / 3.17 / ≥0.1	5.85 / 3.15 / ≥0.1	5.93 / 3.25 / 0.15	6.02 / 3.22 / <0.005	6.10 / 3.25 / <0.005	6.18 / 3.1 / 0.035	6.25 / 3.0 / 0.010

90Th	91Pa	92U	93Np	94Pu	95Am	96Cm	97Bk	98Cf	99Es	100Fm	101Md	102No
6.08 / 3.4 / >0.05	5.89 / 3.7 / >0.05	6.05 / 3.63 / >0.05	6.19 / 3.9	6.06 / 3.6 / ≥0.05	6.00 / 3.7	6.02 / 3.9	6.23 / 3.8	6.30 / 4.0	6.42 / 3.3			

Figure 2.6 The periodical table of elements with the ionization energies (upper row), EWF values (middle row) and electron affinities (lower row), given in eV/atom [47]

2.2.4.2 EWF and surface energy

Surface energy and EWF are two important properties of metallic surfaces, and their determination is of significance to understanding of a wide range of surface phenomena [49], including growth rate, adsorption, surface segregation, *etc.* Since both surface energy and EWF can be related to the electron density [62,63], a certain relationship between surface energy and EWF is expected. Kalazhokov [64] developed a relationship between surface energy and EWF as expressed in Eq. (2.8)

$$\gamma_i = (2 - \frac{\varphi_i}{\varphi_0})\varphi_0 \qquad (2.8)$$

where γ_i and φ_i are, respectively, the surface energy and EWF of the studied surface, φ_0 is the EWF of the polycrystalline sample.

Based on Eq. (2.8), materials with higher EWFs generally have larger surface energies. It should be pointed out that both EWF and surface energy are crystal orientation-dependent. The crystal plane with higher EWF possesses smaller surface energy. Such relationship has also been demonstrated by first-principles calculation[49,65].
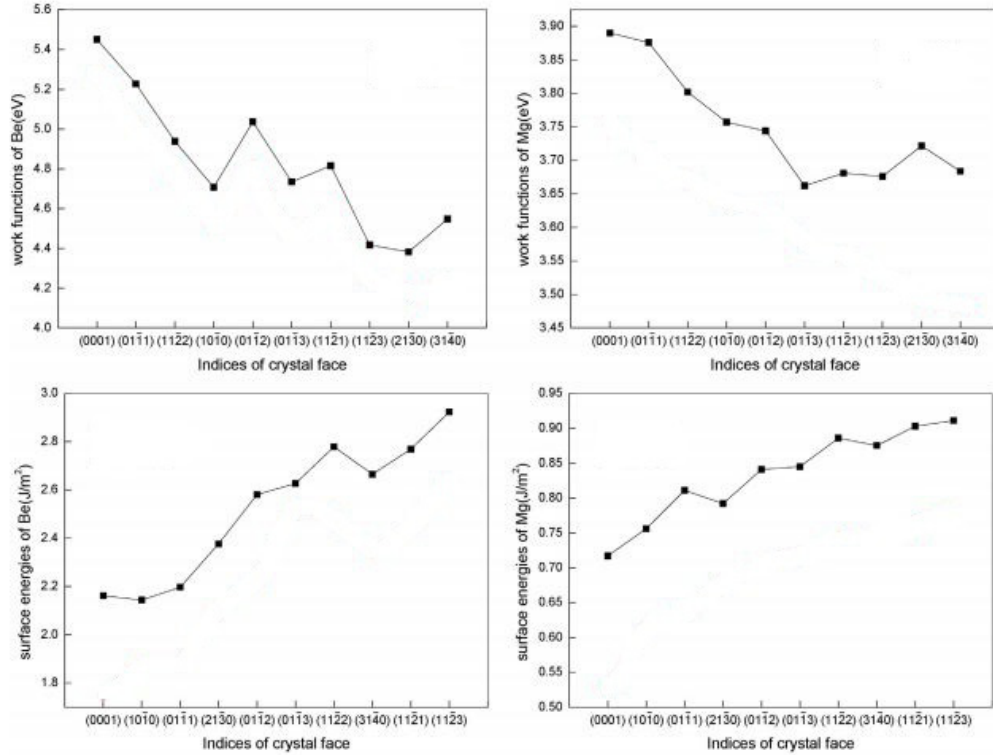
Figure 2.7 Simulated surface energies and EWFs of Be (left figures) and Mg (right figures) as a function of surface crystallographic orientation [65]

2.2.4.3 EWF and adhesion

Adhesion is the tendency of two different surfaces to cling to each other, which plays an important role in many surface processes, such as friction, wear, bacterial binding [66,67], *etc*. Surface damage caused by adhesive wear is one of the common modes encountered in industry. The behavior of adherent and growing bacteria on surfaces has received increasing attention in the food industry and usage of medical devices. Both adhesion and EWF are strongly dependent on the arrangement and nature of atoms on the surface, so EWF can reflect the adhesion characteristics of

the surface. It is doable to correlate EWF with the adhesive force via surface energy as a bridge. A surface with a larger surface energy is more reactive, corresponding to a larger adhesive force when in contact with or approaching a counter-face. As discussed in section 2.2.4.2, according to experimental and theoretical studies, the material with higher EWF has larger surface energy. Thus a material with higher EWF shows larger adhesive force when in contact with a counter-face. It was demonstrated that austenite exhibited higher EWF and a larger adhesive force with the AFM tip than ferrite in a duplex stainless steel [68].

It has also been found that both EWF and adhesive force are dependent on the crystallographic orientation. Table 2.1 shows EWF and adhesive force of different crystallographic planes of copper [15]. It is demonstrated that EWF decreases as the surface atomic packing density decreases in the following order: (011), (112), (321) and (413). A closely packed plane has a higher EWF since an electron is subjected to a higher attractive force from the positive nuclei that have a higher surface packing density according to the electrostatic force model [69]. Based on the "broken bond" model of surface energy [70], a closely packed plane has fewer broken bonds than a loosely packed plane, and thus fewer active positions to interact with foreign atoms when in contact with another surface. So a closely packed plane has a lower surface energy, leading to a lower adhesive force when in contact with the counter-face. The measurements and analysis of EWF and adhesive force have demonstrated a clear relationship between EWF and adhesion. As shown in Table 2.1, the lower the EWF, the higher is the adhesive force for different crystallographic planes of a material.

Table 2.1 EWFs and adhesive forces of different crystallographic planes of single crystal copper when in contact with the AFM tip (Si_3N_4) [15]

Orientation	(011)	(112)	(321)	(413)
EWF (eV)	4.59	4.12	4.56	4.00
Adhesive force (nN)	17.3	19.4	17.4	21.3

2.2.4.4 EWF and Young's modulus

A generic relation between Young's modulus and EWF of polycrystalline metals has been established [71]. Young's modulus is defined as the second-order derivative of interaction potential with respect to the equilibrium distance. The interaction potential of one valence electron is expressed as

$$U = \frac{\alpha z e^2}{a} \tag{2.9}$$

where α is the Madelung constant, e is elementary charge, z is the number of valence electrons, a is the equilibrium distance between a pair of adjacent positive and negative charges. According to the definition of Young's modulus, one may obtain Young's modulus described in terms of equilibrium distance

$$E = \frac{d^2 U(r)}{dr^2}\bigg|_{r=r_0} = \frac{2\alpha z e^2}{a^3} \tag{2.10}$$

EWF is derived based on the image model as discussed in section 2.2.2

$$\varphi = \frac{e^3 m^{1/2} n^{1/6}}{16\sqrt[3]{3}\pi^{5/3}\hbar\varepsilon_0^{3/2}} \qquad (2.11)$$

where n is the equilibrium valence electron density, m is the electron mass, ε_0 is the

vacuum permittivity, $\hbar$ is Planck constant.

Since the electron density is inversely proportional to lattice distance

$$n = \frac{z}{a^3}$$

EWF can be expressed as

$$\varphi = \frac{e^3 m^{1/2} z^{1/6}}{16\sqrt[3]{3}\pi^{5/3}\hbar\varepsilon_0^{3/2} a^{1/2}} \qquad (2.12)$$

Since the parameters z and a are related to Young's modulus, the relationship

between EWF and Young's modulus may established as

$$E = 2\alpha z e^2 (\frac{16\sqrt[3]{3}\pi^{5/3}\hbar\varepsilon_0^{3/2}}{e^3 m^{1/2} z^{1/6}})^6 \varphi^6 \propto \varphi^6 \qquad (2.13)$$

This formula shows a six power relationship between Young's modulus and

EWF, which is validated by the collected experimental data shown in Figure 2.8.
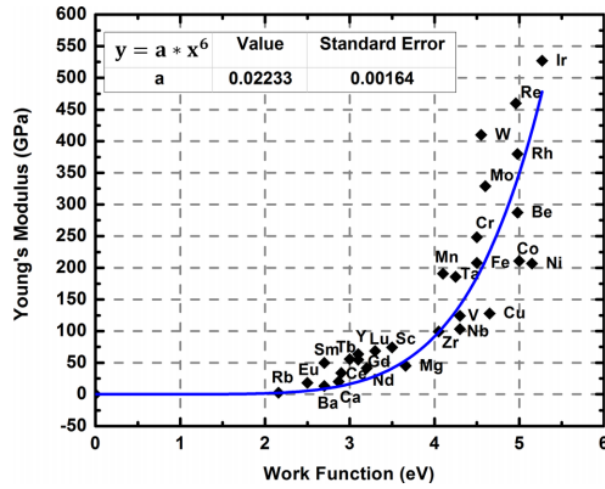
Figure 2.8 Collected experimental data and theoretical curve of Young's modulus and EWF relationship of polycrystalline metals [71]

2.2.4.5 EWF and yield strength

Yield strength is the critical stress above which dislocations are generated, which results in plastic deformation. Although yield strength is influenced by many other factors such as the activated slip system, yield strength is intrinsically dependent on atomic bonding. Based on the Peierls–Nabarro model, yield strength can be expressed as

$$\sigma_y = \frac{2G}{(1-\upsilon)\cos\theta\cos\phi}\exp(-\frac{4\pi\zeta}{b})$$

(2.14)

where σ_y is yield strength, G is shear modulus, υ is Poisson's ratio, b is Burgers vector, $\zeta = a/2(1-\upsilon)$ is a parameter measuring the width of a dislocation (a is lattice constant), the angles θ and ϕ represent the slip direction and slip plane

26

normal, respectively, relative to the applied tensile force.

Since shear modulus and Young's modulus have the relationship

$$G = E \Big/ 2(1+\upsilon) \qquad\qquad (2.15)$$

Eq. (2.14) becomes

$$\sigma_y = \frac{E}{(1-\upsilon^2)\cos\theta\cos\phi}\exp(-\frac{4\pi\zeta}{b}) \qquad\qquad (2.16)$$

Since Young's modulus has a six power relationship with EWF, yield strength can be expressed as [72]

$$\sigma_y \propto \frac{1}{(1-\upsilon^2)\cos\theta\cos\phi}\exp(-\frac{4\pi\zeta}{b})\varphi^6 \qquad\qquad (2.17)$$

Yield strength has a six power dependence on the EWF and it is also influenced by the operation of slip systems related to applied stress orientation, Poisson's ratio, Burger's vector, and the dislocation width. Figure 2.9 illustrates the relationship between EWF and yield strength.
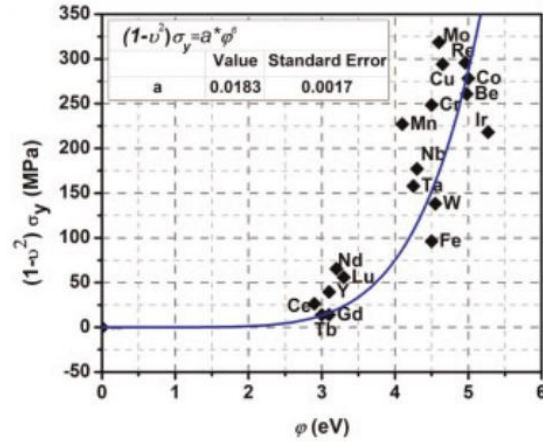
Figure 2.9 Relationship between EWF and yield strength [72]

2.2.4.6 EWF and hardness

Hardness is the resistance of a solid to plastic deformation. Although hardness is an integrated property of many mechanical properties such as elastic stiffness, plasticity, strength and toughness, it is approximately proportional to the yield strength. Thus, one may correlate hardness to EWF as [72]

$$H \propto \frac{1}{(1-\upsilon^2)\cos\theta\cos\phi}\exp(-\frac{4\pi\zeta}{b})\varphi^6 \tag{2.18}$$

Due to the linear relationship between hardness and yield strength, the dependence of hardness on EWF is similar to that of yield strength. It should be noted that yield strength and hardness are also influenced by many other extrinsic factors, such as possible texture, heat treatment, cold working, *etc*. The physical mechanism responsible for the correlations between EWF and intrinsic yield

strength and hardness is explainable. It is known that the activation energies for dislocation motion, which determines the yield strength and hardness, are closely related to the electronic state. A higher EWF corresponds to a higher stability of electron state in metallic bonds, and thus a larger driving force is required for dislocation movement and electron rearrangement. Therefore, the resistance of a metal to mechanical deformation should be consequently larger when its EWF is higher.

2.2.4.7 EWF and ductility

Relationship between EWF and intrinsic ductility of transition metals was established recently by first-principle simulations [73]. Brittleness, β, of transition metals was determined by

$$\beta = \frac{W_{shear}}{W_{tensile}} \tag{2.19}$$

where W_{shear} and $W_{tensile}$ are shear strain energy density and tensile strain energy density stored in the unit volume.

The parameter β as a measure a brittleness is explainable. Dislocation emission is easy at the crack tip if shear occurs easily (small W_{shear}), and thus gives ductile characteristics. The situation is reversed when the crack propagation needs less energy (small $W_{tensile}$). Larger β corresponds to brittle materials with poor ductility. Figure 2.10 illustrates the relationship between calculated brittleness and

EWF. The dependence of ductility on EWF could be separated into two categories. When EWF is lower than about 4.6 eV, ductility of a metal is insensitive to the variations in EWF. However, when EWF is larger than 4.6 eV, ductility decreases rapidly as EWF increases. The underlying mechanism responsible for such behavior could be explained based on how the property of valence electrons changes during the deformation process. It is suggested that paired valence electrons in a metal with low EWF are easily redistributed to accommodate the external deformation, thus showing good ductility. Whereas for metal with high EWF, it prefers to have unpaired valence electrons in order to release the strain energy, which corresponds to poor ductility.
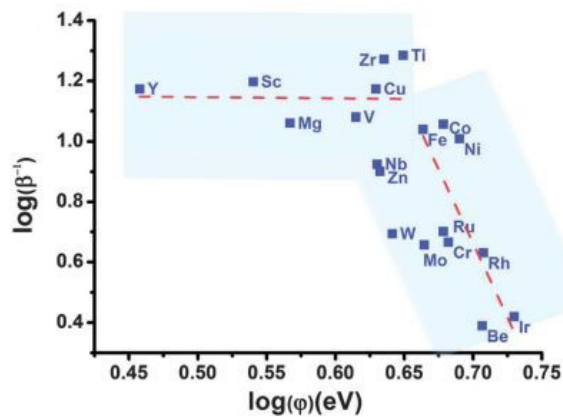
Figure 2.10 Relationship between the reciprocal of calculated brittleness and EWF[73]

2.2.4.8 EWF and toughness

As discussed in section 2.2.4.5 and section 2.2.4.7, EWF could be a parameter that reflects intrinsic mechanical strength and ductility of metallic materials. Thus, it

is expected that EWF can be related to toughness of materials. It was recently demonstrated that fracture toughness of transition metals can be correlated to their EWF [73]. The fracture toughness K_{IC} was calculated as

$$K_{IC} = (\beta^{-1})^{1.4} B(\Omega_0 / N)^{1/6} \qquad (2.20)$$

where β is a parameter that reflects brittleness of the material, B is bulk modulus, Ω_0 is the volume of cells, N is the number of atoms in the supercell
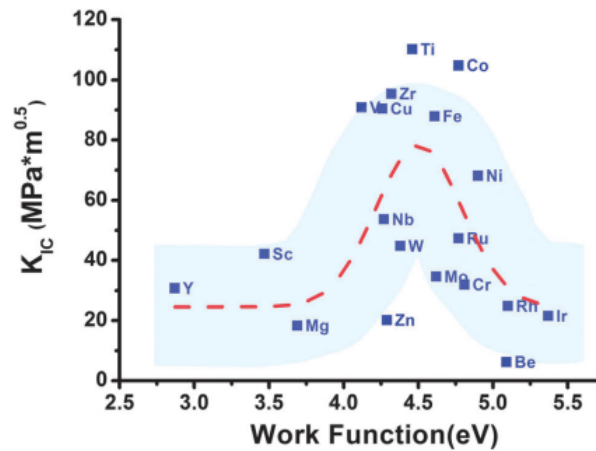
Figure 2.11 Relationship between EWF and fracture toughness [73]

Figure 2.11 demonstrates the relationship between EWF and fracture toughness. As shown, fracture toughness increases as EWF increases when EWF is smaller than about 4.6 eV. For metals with EWFs larger than 4.6 eV, fracture toughness decreases dramatically with an increase in EWF. It is known that fracture toughness of a material is dependent on both of its strength and ductility synergistically. As

discussed in section 2.2.4.5, a lower EWF corresponds to poor strength. Thus for an element with a smaller EWF, the lower fracture toughness results from lower mechanical strength. Whereas, for an element with a larger EWF, although it has high mechanical strength, the lower fracture toughness results from poor ductility as discussed in section 2.2.4.7. Therefore, transition metals with EWFs around 4.6 eV possess maximal fracture toughness due to appropriate strength and ductility at the same time.

2.2.4.9 EWF and atomic size

The empirical relationship between atomic size and EWF was proposed by fitting the experimental data [74]. Figure 2.12 illustrates the fitted secondary polynomial relationship. The decrease in atomic radius with EWF is understandable, since higher EWF corresponds to stronger atomic bonding and thus smaller spacing between adjacent atoms.
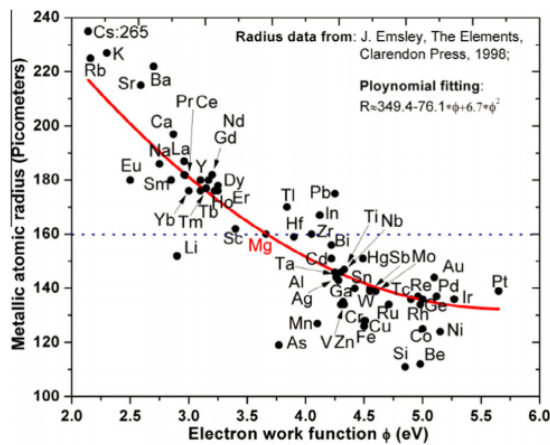
Figure 2.12 The atomic radius of solid solutes versus EWF, which shows a secondary polynomial relationship [74]

2.2.4.10 EWF and surface roughness

The relationship between EWF and surface roughness was studied theoretically and experimentally [75,76]. Surface roughness and EWF were measured by AFM and SKP, respectively. As discussed in section 2.2.3, EWF measured by SKP is dependent on the difference in electronic energy levels between two electrodes. If EWFs of probe tip and sample are φ_T and φ_S, the CPD is written as

$$e \cdot V_{CPD} = \varphi_T - \varphi_S \tag{2.21}$$

For a parallel plate capacitor, $V_{CPD} = e/C$ and the capacitance $C = \dfrac{\varepsilon_0 \varepsilon_r S}{d}$, ε_0, ε_r, S, d are the vacuum dielectric constant, the relative dielectric constant in air, the area of the plate capacitor and the distance between the tip and the sample surface. Therefore, EWF of the sample can be expressed as

$$\varphi_S = \varphi_T - \frac{e^2 d}{\varepsilon_0 \varepsilon_r S} \tag{2.22 a}$$

Generally, the term $\dfrac{e^2}{\varepsilon_0 \varepsilon_r}$ is a constant, and the distant d between tip and sample keeps constant during measurement; thus EWF of the sample can be expressed as

$$\varphi_S = \varphi_T - \frac{C}{S} \tag{2.22 b}$$

On a rough surface, the effective capacitor is mainly formed by the tip and the bulged part of the sample surface. As a result, with an increase of surface roughness,

the effective area in the microcapacitor consisting of the tip and the sample surface is reduced, which corresponds to a decrease in EWF as shown in Figure 2.13.
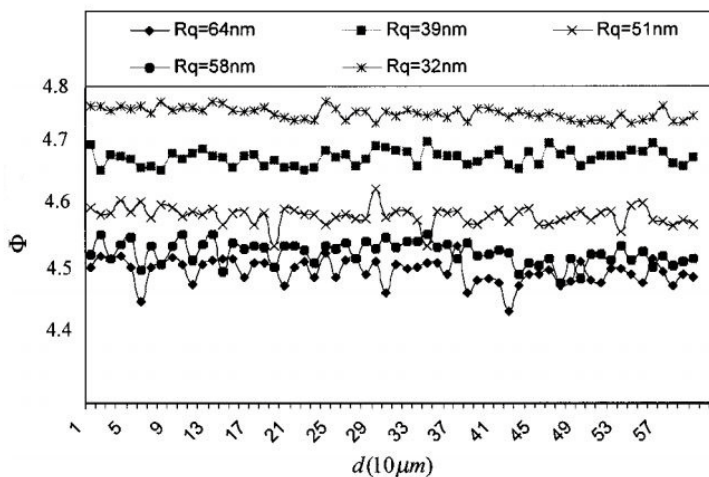
Figure 2.13 Variations of EWFs of different sample surfaces as a function of roughness [76]

2.2.4.11 EWF and electrode potential

Electrode potential is the potential drop at the metal/solution interface, which is not directly measurable. That is the reason why electrode potentials are often referred to a standard, *e.g.*, the standard hydrogen electrode. The absolute electrode potential (E_{abs}) of a sample covered by a liquid layer is an analogy to the definition of EWF. It is defined as the minimum energy to extract an electron from the Fermi level of the sample through the solid/liquid interface, through the liquid, through the surface of the liquid, to a position just outside the liquid [77]. The absolute electrode potential can be expressed as

$$E_{abs} = \frac{\mu}{e} + \Delta\varphi_M^{EI} + \chi_s \tag{2.23}$$

where μ is chemical potential of the sample, $\Delta\varphi_M^{EI}$ is the potential drop at the metal/liquid interface, χ_s is surface potential of the liquid surface. It is not difficult to derive the following relation

$$E_{abs} = \frac{\varphi}{e} + (\psi^M - \psi^S) \tag{2.24}$$

where ψ^M and ψ^S denote the Volta potentials outside the metal and outside the solution, φ is EWF of the metallic sample

As expressed by Eq. (2.24), EWF is a component and correlates to the electrode potential of a material.

When considering the case when a metallic probe is positioned near the surface of the electrolyte,

$$E_{abs} = \frac{\mu}{e} + \Delta\varphi_M^{EI} + \chi_s = \frac{\varphi^M}{e} + (\psi^M - \psi^S) = \frac{\varphi^{KP}}{e} + (\psi^{KP} - \psi^S) \tag{2.25}$$

where φ^M and φ^{KP} denote EWF of the metallic sample and the metallic probe, ψ^{KP} is the Volta potential outside the probe

Thus, if the EWF value of the probe is known, the measurement of the Volta potential difference $(\psi^{KP} - \psi^S)$ provides the absolute electrode potential of the

sample. The Kelvin probe technique provides a way to measure the Volta potential difference and the electrode potential of a material.

2.2.5 Applications of EWF

EWF is a characteristic parameter for metals and semiconductors. It is sensitive to surface conditions, such as deformation, adsorption, corrosion, *etc*. Due to its high sensitivity to surface condition, EWF has attracted increasing interest from materials scientists and engineers. The Kelvin probe technique makes it possible for non-contact monitoring of changes in the EWF of materials. It has provided invaluable information to understanding surface and interface physics and chemistry[9], which is crucial for development of advanced materials. With the help of SKP and KPFM, monitoring EWF is applied in studies in many areas, such as wear and corrosion [77,78].

2.2.5.1 Applications in determining yielding point

Studies of the effects of mechanical force on the behavior of electrons inside a solid are of both fundamental and practical importance [79]. The Kelvin probe technique was applied to investigate the effect of deformation on EWF and its physical mechanism [3-5,13,80]. Experimental results showed that tensile strain decreased EWF in the elastic deformation range, while compressive strain increased EWF. However, EWF in the plastic deformation range always decreased with plastic strain no matter whether it was tensile or compressive [11,12,14,81]. Figure 2.14 demonstrates typical curves of EWF variations during deformation processes. As shown by the simultaneous measurements of EWF, yield point can be related to

the critical stress for the transition of EWF from smooth variation to steep variation. It demonstrates that the Kelvin probe technique could be used for determining the onset of yielding since EWF is a parameter sensitive to the yielding process. Yielding behavior is usually determined by tensile testing; however, yielding of a metal could be very complicated when it occurs under complex stress states and there are no sound theoretical models and it is difficult to determine the onset of yielding under complex conditions. EWF measurement by the Kelvin probe technique provides a promising way to determine the yield point of materials, especially under complex working conditions.
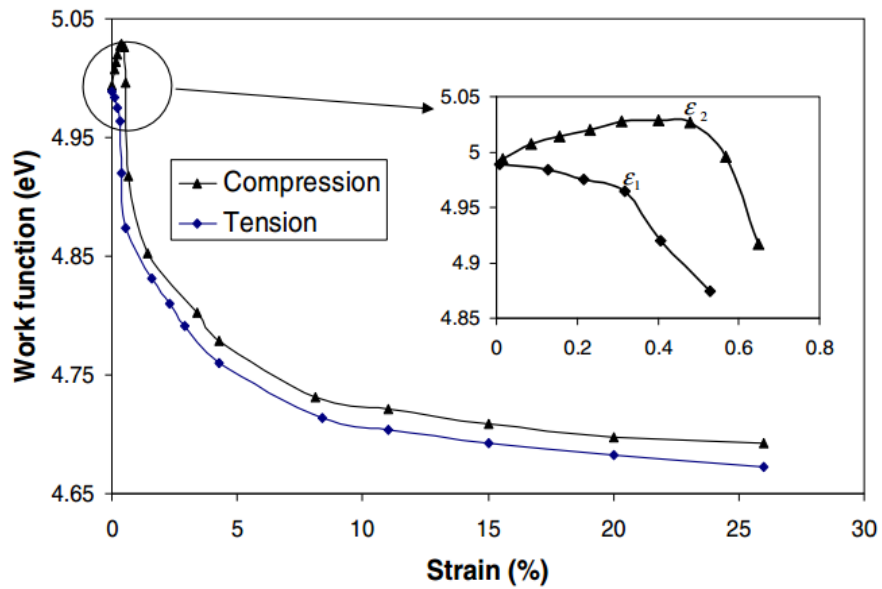
Figure 2.14 Variations in EWF of Cu with respect to plastic strain. The inset shows variations in EWF with respect to elastic strain [13].

Theoretical studies of the effect of deformation on EWF are quite scarce. DeVechio and Bhushan suggested that when a crystalline sample was structurally

altered, the Fermi energy level would vary, thus leading to changes in EWF [82]. However, details of the theoretical treatment and an in-depth discussion were not given. An electrostatic interaction model to correlate EWF with deformation was proposed, which readily explains the effect of deformation on EWF [13,14,83]. In the electrostatic interaction model, EWF is defined as the depth of the potential well, and a one dimensional lattice is considered. EWF can be expressed as [83]

$$\varphi = \sum_{-n}^{n} \frac{ze^2}{4\pi\varepsilon_0 |x_i - x_{ei}|} \qquad (2.26)$$

where z is the charge number of a nucleus, ε_0 is the permittivity constant. x_i and x_{ei} represent the equilibrium position of the ith nucleus and the position of the electron between x_i and $x_{i\text{-}1}$ in the shallowest electron potential well, respectively.

In the elastic deformation region, if a lattice is in tension, the spacing between nuclei as well as that between nuclei and electrons is increased. As a result, EWF will decrease according to Eq. (2.26). The result is reversed if the lattice is in compression. If the material suffers from plastic deformation and dislocations are generated, it can be proved that EWF decreases based on relevant analysis of Eq. (2.26) and dislocation models.

2.2.5.2 Applications in wear research

SKP has been adapted for continuous non-destructive monitoring of changes in EWF of a rubbing surface [78]. The method can be used to investigate tribological

materials for a wide range of conditions, including changes in load, sliding speed, and environment due to EWF is sensitivity to deformation, adsorption, phase changes and redistribution of components, *etc*.

The onset of wear and the history prior to measurable wear are of importance to fundamental understanding of tribological processes and have attracted increasing interest [17]. Weight loss measurement, morphological observation and EWF measurement for the sample surface by SKP were applied to study the early stage of wear under different loads [16]. It was found that EWF measurement was the most sensitive technique to changes in surface condition and could be used to investigate the history prior to the occurrence of measurable wear. Figure 2.15 illustrates the sensitivities of the three methods to wear schematically. As shown, EWF measurement provides a promising approach to investigate the onset of wear, especially under low load, which is difficult to detect by traditional techniques, such as weight loss measurement and morphological observation.
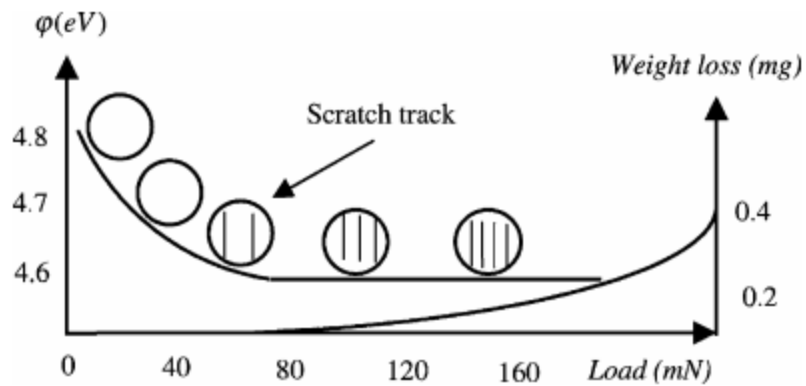
Figure 2.15 A schematic illustration of the sensitivities of three methods to wear: weight loss measurement, morphological observation, and EWF measurement [16]

Since EWF is sensitive to the onset of wear and could be used for diagnosis of wear under light loads, it has attracted increasing interest from the nano/micro-device industry in studying the wear on a nanometer size scale of magnetic recording device, microelectromechanical systems (MEMS), *etc* [78,84]. In MEMS wear depths of a few nanometers can be critical and any wear debris could be an indication of catastrophic failure. EWF can detect atomic scale structural changes and chemical changes at the surface exposed to wearing forces. It was demonstrated that even in the case of no visible deformation of the surface detected by AFM, a large change of EWF could be observed [82] as shown in Figure 2.16.
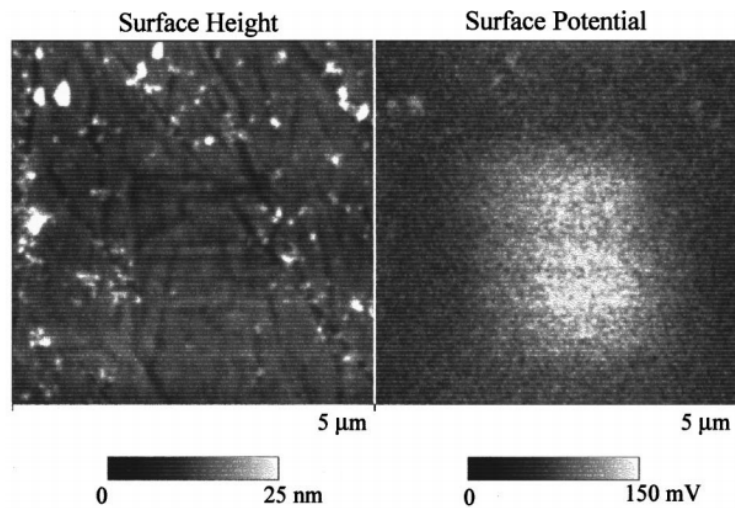
Figure 2.16 Surface height and EWF maps of wear regions generated at 1 μN on a single crystal aluminum sample [82]

The relationship between EWF and friction under low load was also investigated. It was demonstrated that a smooth metal surface with lower EWF showed a larger frictional force when in contact with a ceramic counter-face [18]. For metal-metal contact, an energy consumption friction model was proposed to

calculate the friction coefficient and express the friction coefficient as a function as EWF and mechanical properties of the metals [19,21].

2.2.5.3 Applications in corrosion research

EWF is a measure of electrochemical stability of a material and has a close relationship with corrosion behavior of materials. Materials with higher EWFs generally have higher corrosion resistance. SKP is a useful tool to investigate corrosion behavior of materials [85-87]. SKP was used to determine EWFs of the passivated surfaces of different stainless steel specimens [87]. It was found that the sample surface with highest EWFs has the most positive corrosion potential as shown in Figure 2.17. The nanocrystalline surface produced using a sandblasting and annealing process was superior and was more resistant to corrosion than the original stainless steel.
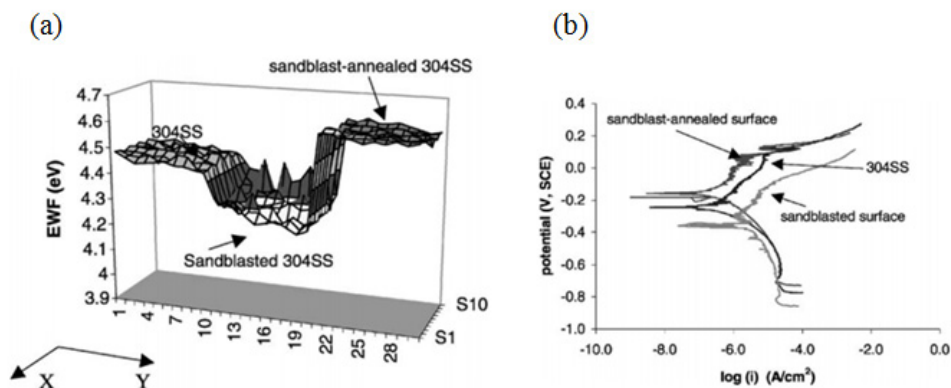
Figure2.17 (a) Surface EWF of different specimen (b) Polarization curves of different specimens in a 3.5% NaCl solution [87]

With the help of KPFM, Volta potential which is related to EWF can be mapped for material surfaces to analyze relative nobility of different phases in the materials. KPFM or EWF mapping technique is widely used in corrosion studies and analysis [77]. Considerable studies have been conducted to investigate the corrosion behavior of steels using KPFM [88-90]. As shown in Figure 2.18, ferrite has a lower EWF and is expected to be more prone to corrosion. As for the finely dispersed chromium nitride in the ferrite matrix, the chromium nitride particles and clusters have higher EWF than the matrix and are nobler than ferrite. The relative nobility of different phases interpreted from EWF maps is verified by line profile of AFM topography of the material after a corrosion test. It is demonstrated that phases with lower EWFs are more easily corroded.
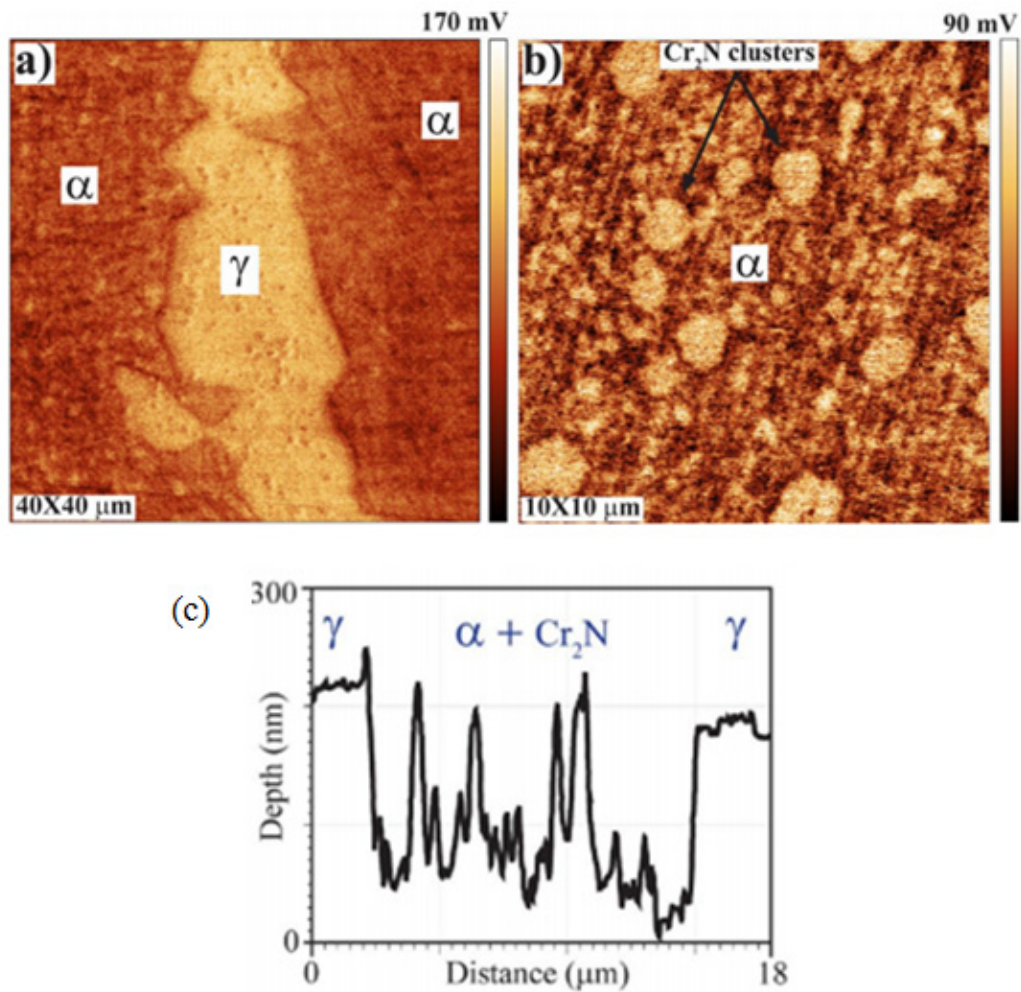
Figure 2.18 EWF maps of heat treated 2205 duplex stainless steel with (a) ferrite and austenite (b) ferrite matrix with finely dispersed and clusters of quenched-in chromium nitride and (c) line profile of AFM topography of the material after corrosion test [89]

In addition to studies on steels, extensive work has also been conducted for many other materials, such as aluminum alloys [91], copper alloys [92], Ti/Mg-Al dissimilar materials [93], *etc*. KPFM technique and EWF measurements provide

invaluable information to understand the corrosion behavior of the materials.

2.2.5.4 Applications in adsorption research

It has long been recognized that adsorption and interaction of gas atoms with clean metal surfaces may change the EWF of metals [37,40]. Figure 2.19 illustrates how the interaction of oxygen with copper nickel alloys changes EWFs of the alloys. Reconstructions of the surface structures and nucleation of oxides may be the reason why the surface EWFs change when the alloys interact with oxygen.
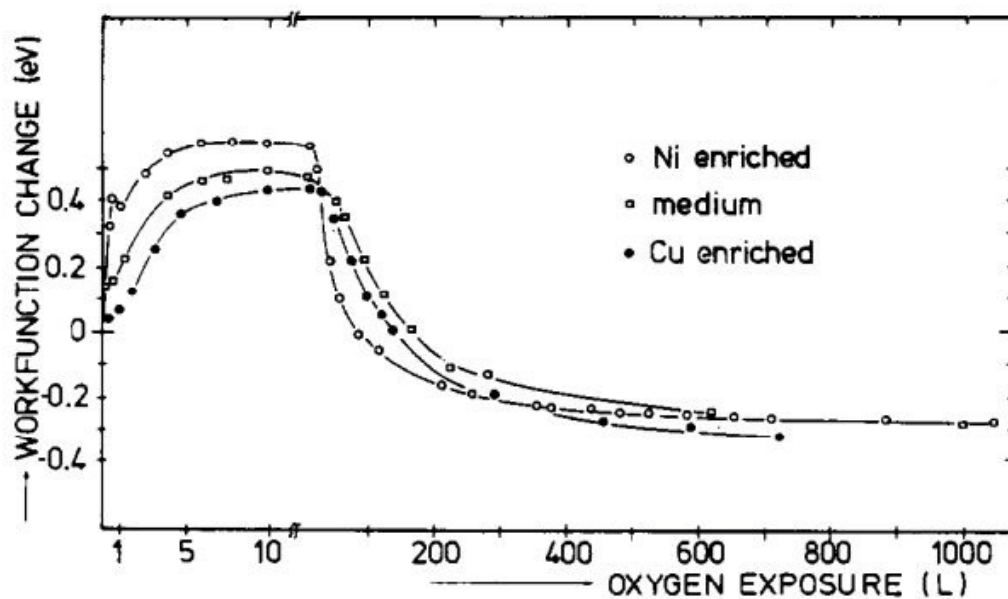
Figure 2.19 EWF changes during oxygen interaction with copper nickel alloy [40]

Since EWF of the material surface is gas sensitive, applications of EWF monitoring in a gas sensor have attracted considerable attention [94]. Due to the fact that EWF responds to atmosphere sensitively, it provides an approach to

manufacture gas sensors for a wide range of industrial and domestic applications.

2.2.5.5 Applications in materials and devices design

It is known that EWF dominates the oriented mobility of positive and negative charges, which is important to the heterogeneous junctions in microelectronics [95], photocatalysis [96], solar cells [97], *etc.* By choosing materials with proper EWF values, significant charge transfers may occur in the heterogeneous junctions. It is expected to improve the performance of the devices if one can modulate EWFs of the materials. Geonwook Yoo, *et al.,* demonstrated over 20-fold enhanced photoresponsivity of multilayer MoS2 field-effect transistor by using thin sub-stoichiometric molybdenum trioxide overlayer, which is known as a high EWF material [96].

Although EWF has long been recognized as an important parameter in heterogeneous junctions and functional materials design, little attention has been paid to the application of the EWF concept in structural materials design up to date. Recently, William Yi Wang, *et.al,* investigated solid solution hardening in aluminum alloys and magnesium alloys via the density functional theory and EWF approaches[98, 99]. EWF, bonding charge density and hardness of the materials were analyzed. It was demonstrated that materials with higher EWFs possessed higher hardness, which is consistent with the theoretical model discussed in section 2.2.4.6. Mechanical strength, ductility and EWF were also calculated by first-principles methods for magnesium alloys [74]. It is predicted that adding elements with lower EWFs may improve both mechanical strength and ductility of magnesium; however, adding elements with higher EWFs resulted in higher mechanical strength but lower

ductility. With the help of computational simulation, relationships between EWF and mechanical properties of materials have been demonstrated, which also shows that EWF is a very promising parameter for materials design. However, these studies have not yet been proved by experimental observations and still need further analysis.

Chapter 3 Correlations between EWF and properties of pure metals

Mechanical and thermal properties of metals are intrinsically determined by the atomic bond strength which is governed by the electron behavior, though also influenced by other factors such as activated slip systems. One may expect that there should be generic relationships between EWF and the properties. If the atomic interaction or atomic bond energy can be correlated to EWF in a straightforward way, in-depth understanding of intrinsic mechanical and thermal properties on an electronic base could be readily achieved. This would also provide an alternative approach and complementary clues for advanced materials design. This chapter presents a theoretical study of the correlations between properties of pure metals and their EWFs. A simple approach to establish the correlations is proposed using the Lennard-Jones potential as a bridge. The approach is applied to several properties of metallic materials, including bulk modulus, thermal expansion and heat capacity (Debye temperature). The work reported in this chapter has been published in Lu, H. & Li, D. Correlation between the electron work function of metals and their bulk moduli, thermal expansion and heat capacity via the Lennard–Jones potential. Physica status solidi (b) 251, 815-820 (2014).[100]

3.1 Relation between EWF and the atomic bond energy

Lennard-Jones(L-J) potential is a mathematically simple model to represent the interaction between a pair of atoms and associated bond energy. Due to its simplicity, the L-J potential has been often used in physical calculation and

computer simulation to reveal material phenomena and processes, although it is not a very accurate potential expression [101]. Many material properties can be easily related to the atomic bond energy through the L-J potential [102,103].

A common expression of Lennard-Jones potential is

$$V(r) = \varepsilon_b \left[\left(\frac{r_e}{r} \right)^{12} - 2 \left(\frac{r_e}{r} \right)^6 \right] \tag{3.1}$$

where ε_b is the depth of the potential well, *i.e.*, the bond energy, and r_e is the equilibrium distance between a pair of adjacent atoms. Considering that two adjacent atoms are connected by a spring with a spring constant of k, in the vicinity of r_e, Taylor expansion of the L-J potential gives

$$\begin{aligned} V(r) &= V(r_e) + \frac{V'(r_e)}{1!}(r - r_e) + \frac{V''(r_e)}{2!}(r - r_e)^2 + \dots \\ &\approx V(r_e) + \frac{1}{2}V''(r_e)(r - r_e)^2 \end{aligned} \tag{3.2}$$

$$k = \left. \frac{d^2V}{dr^2} \right|_{r=r_e} = \frac{72\varepsilon_b}{r_e^2} \tag{3.3}$$

Thus, the spring force (F) and consequently Young's modulus (E) can be calculated as,

$$F = k\Delta r = k(r - r_e) \tag{3.4}$$

$$E = \frac{\sigma}{\varepsilon} \tag{3.5}$$

where σ and ε are stress and strain. Let each atom have an approximate occupied area of r_e^2, thus

$$\sigma = \frac{F}{r_e^2} = \frac{k\Delta r}{r_e^2} = E \cdot \varepsilon = E\left(\frac{\Delta r}{r_e}\right) \tag{3.6}$$

$$\therefore E = \frac{k}{r_e} = \frac{72\varepsilon_b}{r_e^3} \propto \frac{\varepsilon_b}{r_e^3} \tag{3.7}$$

It has been shown that Young's modulus has a sixth power relation with the EWF, $E \propto \varphi^6$ (Figure 3.1 (a)) [71]. Since Young's modulus increases linearly with the bond energy increases as expressed in Eq. (3.7) (also see Figure 3.1(b)), the bond energy should also have a sixth power relationship with EWF, which is supported by reported experimental measurements as illustrated in Figure 3.2.
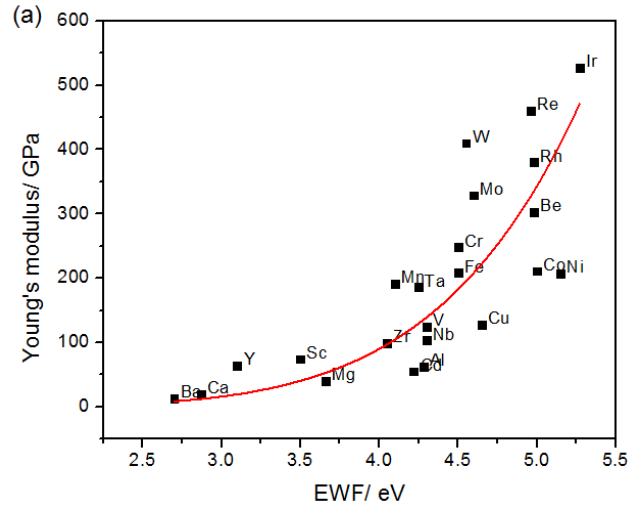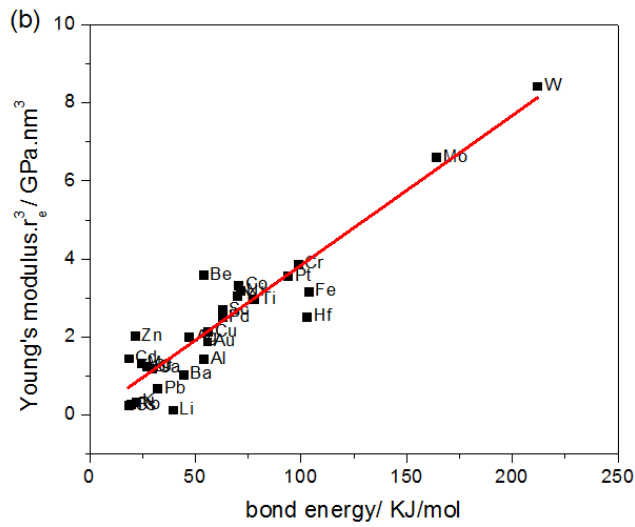
Figure 3.1(a) Relation between Young's modulus and EWF. (b) Relation between Young's modulus and bond energy. Experimental values are given in Table 3.1.
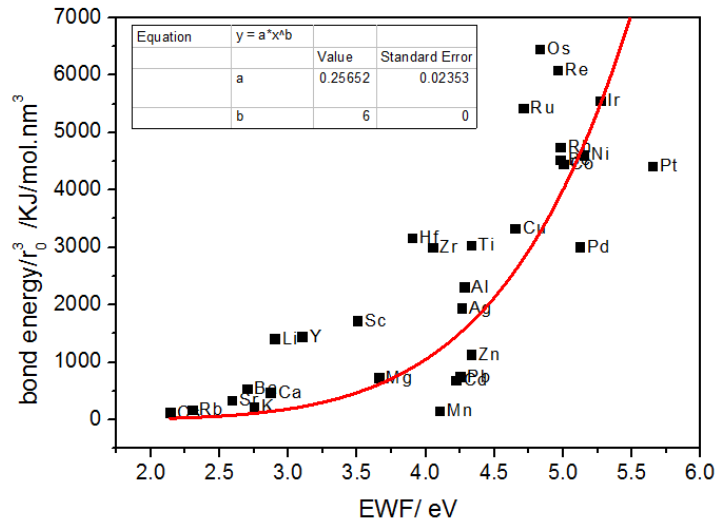
Figure 3.2 Relation between EWF and the bond energy. Experimental values are given in Table 3.1.

Table 3.1 Experimental data used to fit curves, data are cited from [10,61,104,105]

Element	Electron work function (eV)	Bond energy (KJmol^{-1})	Young's modulus (GPa)	Bulk modulus (GPa)	Thermal expansion (μmm^{-1}K^{-1})	Debye Temperature (K)
Li	2.9	39.22	4.9	11	56	344
K	2.75	21.26	3.53	3.1	83	91
Rb	2.3	19.6	2.4	2.5	90	56
Cs	2.14	18.4	1.7	16	284	38
Be	4.98	53.69	303	130	11.6	
Mg	3.66	24.2	40	45	25.2	400
Ca	2.87	29.29	19.6	17	22.3	230
Ba	2.7	44.38	12.8	9.6	18	110
Al	4.28	53.99	62	26	23.6	428
Sc	3.5	62.55	74.4	57	10.2	360
Ti	4.33	77.9	116	110	10.2	420
V	4.3	127.93	124	160	8	
Cr	4.5	98.53	248	160	6.2	630
Mn	4.1	69.56	191		21.7	
Fe	4.5	103.46	208.2	170	11.8	470
Co	5	70.37	211	180	13.8	445
Ni	5.15	71.2	207	180	13.3	450
Cu	4.65	55.97	128	140	16.5	343
Zn	4.33	21.38	108	70	39.7	327
Y	3.1	69.8	63.5	41	10.6	280
Zr	4.05	101.05	99.3		5.85	
Nb	4.3	180.86	103	170	7.31	275
Mo	4.6	163.91	329	230		450
Rh	4.98	92.4	380		8.3	
Ru	4.71	106.7		220		600
Re	4.96	127.9	460		6.6	
Ir	5.27	110.47	527		6.8	
Pd	5.12	62.62	121	180		
Ag	4.26	47.01	83	100	19	225
Hf	3.9	102.79	78	110		
Cd	4.22	18.26	55	42	31.3	209
Ta	4.25	194.88	186	200	6.5	240
W	4.55	211.73	410			400

3.2 Relation between EWF and bond strength related properties

After the relation between EWF and the bond energy is established, bond-related properties of materials can be correlated to their EWFs. In this study, the effectiveness of this approach is demonstrated by correlating bulk modulus, thermal expansion and heat capacity of metals to their EWF via an L-J potential approach.

3.2.1 Relation between EWF and bulk modulus

The bulk modulus is a measure of the material's resistance to uniform compression, which is defined as the derivative of pressure with respect to the volume,

$$\tilde{K} = -V \frac{\partial P}{\partial V} = V \frac{\partial^2 U}{\partial V^2} \tag{3.8}$$

where U is the total energy of a crystal with N atoms and can be expressed in the form of L-J potential,

$$U = 2N\varepsilon_b \left[\left(\sum_{i \neq j}^{N} \frac{1}{P_{ij}^{12}} \right) \left(\frac{\sigma}{r_e} \right)^{12} - \left(\sum_{i \neq j}^{N} \frac{1}{P_{ij}^{6}} \right) \left(\frac{\sigma}{r_e} \right)^{6} \right] \tag{3.9}$$

Using BCC structure as an example, we have

$$\sum_{i \neq j}^{N} \frac{1}{P_{ij}^{12}} = 9.11, \sum_{i \neq j}^{N} \frac{1}{P_{ij}^{6}} = 12.25, \quad r_e = 1.07\sigma \tag{3.9}$$

For a BCC crystal with its volume equal to

$$V = \frac{1}{2}a^3 N = \frac{4\sqrt{3}}{9}r_e^3 N \tag{3.10}$$

$$r_e = \left(\frac{9V}{4\sqrt{3}N}\right)^{1/3} \tag{3.11}$$

we have

$$U = 2N\varepsilon_b \left[9.11 \left(\frac{\sigma}{(\frac{9V}{4\sqrt{3}N})^{1/3}} \right)^{12} - 12.25 \left(\frac{\sigma}{(\frac{9V}{4\sqrt{3}N})^{1/3}} \right)^{6} \right] = \frac{A}{V^4} - \frac{B}{V^2} \tag{3.12}$$

where $A = 6.4N^5\sigma^{12}\varepsilon_b$, $B = 14.5N^3\sigma^6\varepsilon_b$. Since

$(\frac{\partial U}{\partial V})_{V_\circ} = 0$ and $V_0 = \left(\frac{2A}{B}\right)^{1/2}$, we thus have

$$\tilde{K} = -V\frac{\partial P}{\partial V} = V(\frac{\partial^2 U}{\partial V^2})_{V_\circ} = \sqrt{2}\frac{B^{5/2}}{A^{3/2}} = 69.9\frac{\varepsilon_b}{\sigma^3} \propto \frac{\varepsilon_b}{r_e^3} \tag{3.13}$$

The linear relation of $\tilde{K} \propto \varepsilon_b / r_e^3$ is general, not only valid for BCC structure but also for other crystal structures. Figure 3.3 illustrates the linear relationship

53

between bond energy and bulk modulus for BCC metals and that for metals with different crystal structures as well.
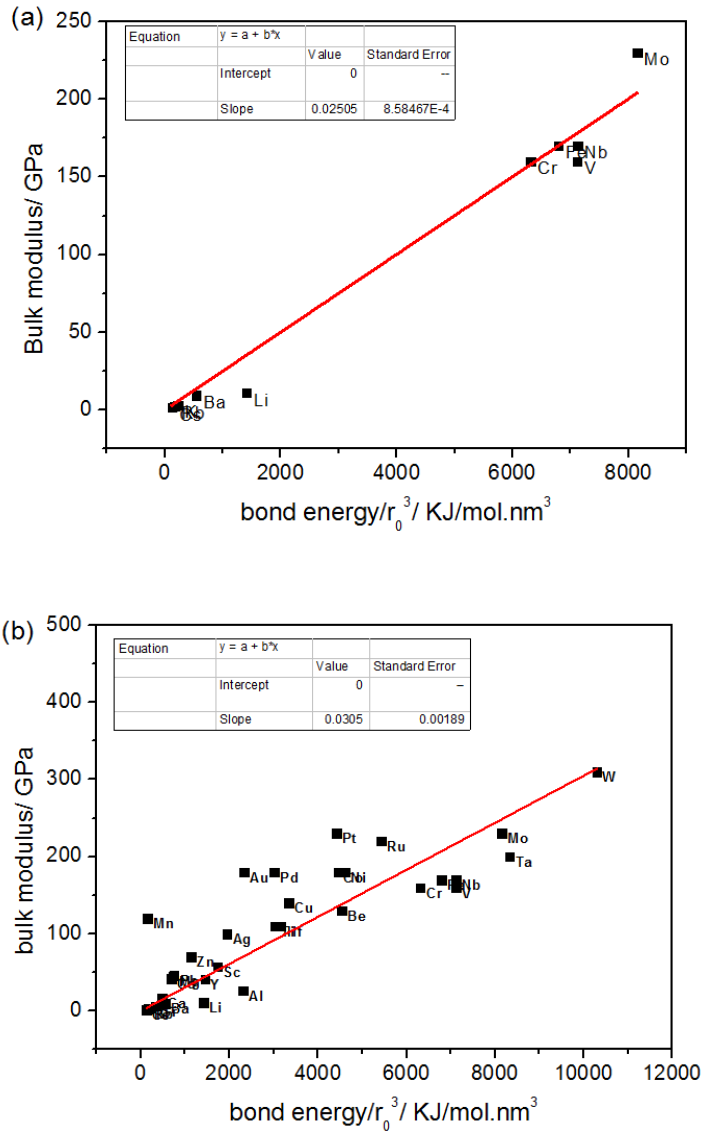
Figure 3.3(a) Relationship between the bond energy and bulk moduli of BCC metals. (b) Relationship between the bond energy and bulk moduli of metals with different crystal structures. Experimental values are given in Table 3.1.

As demonstrated earlier, the bond energy divided by r_e^3 is proportional to sixth power of EWF; thus we have $\widetilde{K} \propto \varphi^6$ as Figure 3.4 illustrates.
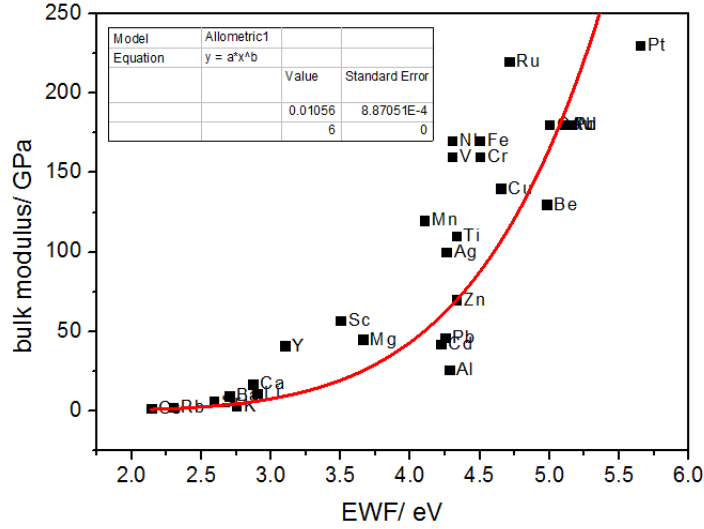
Figure 3.4 Relationship between EWF and bulk modulus. Experimental values are given in Table 3.1.

3.2.2 Relation between EWF and thermal expansion

Thermal expansion coefficient describes the tendency of materials to change in volume in response to a change in temperature, which can be treated by considering oscillation of atoms [10]. Here we only consider one-dimensional situation or linear thermal expansion. The linear thermal expansion coefficient is expressed as

$$\alpha_L = \frac{1}{L}\frac{\partial L}{\partial T} \tag{3.14}$$

where L is the length of an object and T is the temperature. The oscillation can be

calculated based on the L-J potential. With Taylor expansion, the potential energy at a displacement δ from the equilibrium distance r_e, can be expressed as

$$V(r) = V(r_e + \delta) = V(r_e) + \frac{V'(r_e)}{1!}(r - r_e) + \frac{V''(r_e)}{2!}(r - r_e)^2 + \frac{V'''(r_e)}{3!}(r - r_e)^3 + ...$$

(3.15)

Let

$$f = \frac{V''(r_e)}{2!} = 36\frac{\varepsilon_b}{r_e^2} \text{ and } g = -\frac{V'''(r_e)}{3!} = 252\frac{\varepsilon_b}{r_e^3}$$

the coefficient of linear thermal expansion can be expressed as [10]

$$\alpha_L = \frac{1}{L}\frac{\partial L}{\partial T} = \frac{1}{r_e}\frac{\partial \bar{\xi}}{\partial T} = \frac{3g}{4f^2}k_B \propto \frac{1}{\varepsilon_b}$$

(3.16)

The relation of $\alpha_L \propto 1/\varepsilon_b$ has been illustrated in Figure 3.5 (a). Since Young's modulus is proportional to the bond energy, the linear thermal expansion coefficient should thus be inversely proportional to Young's modulus, which can also be demonstrated from thermodynamics [106]. As Young's modulus has a sextic relation with EWF, the reciprocal of thermal expansion coefficient obeys a sixth power relationship with EWF, as illustrated in Figure 3.5 (b).
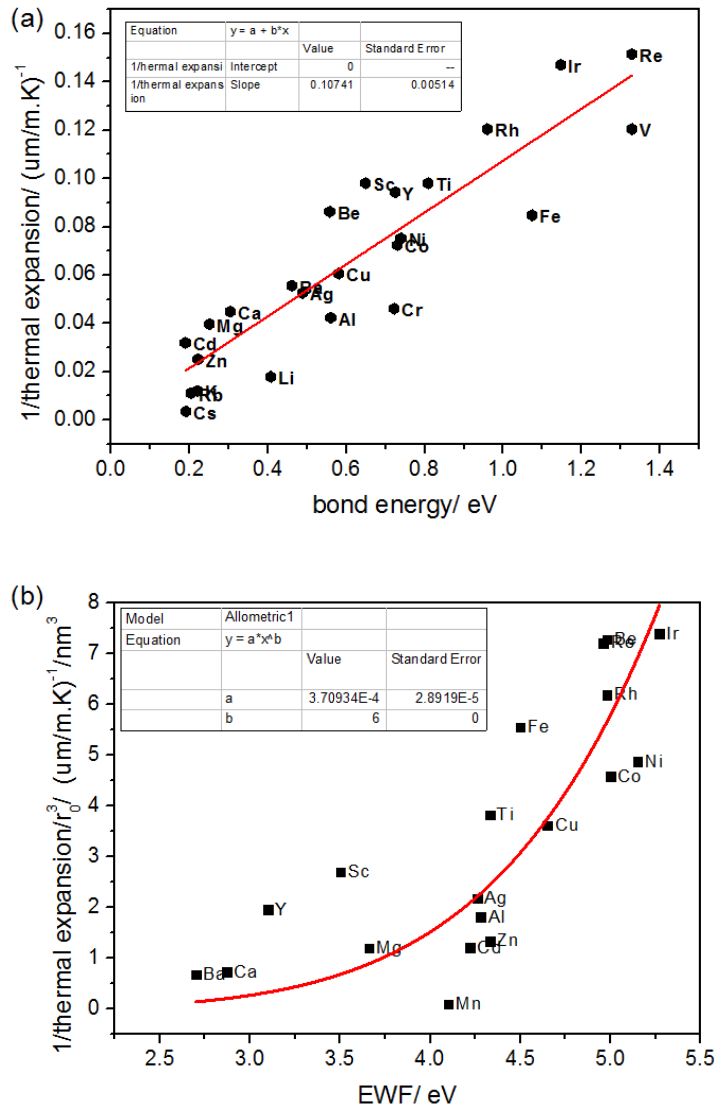
Figure 3.5 (a) Relationship between the bond energy and thermal expansion. (b) Relationship between the EWF and reciprocal of thermal expansion coefficient. Experimental values are given in Table 3.1.

3.2.3 Relation between EWF and heat capacity

Heat capacity is the amount of heat required to change the temperature of a material, which is often described using the Debye model [10],

$$C_V = 9Nk_B \left(\frac{T}{T_D}\right)^{T/T_D} \int_0^{T/T_D} \frac{\xi^4 e^\xi}{\left(e^\xi - 1\right)^2} d\xi \qquad (3.17)$$

where $\xi = \hbar\omega / k_B$ and C_V is the heat capacity at constant volume, k_B is Boltzmann constant. $T_D = \hbar\varpi_D / k_B$ is known as the Debye temperature. ω_D is the Debye frequency, which is proportional to the velocity of elastic waves in a solid or the square root of Young's modulus of the solid. When temperature is much higher than the Debye temperature, the heat capacity is a constant equal to $3Nk_B$ (J.K^{-1}mol^{-1}) for all materials, while it is proportional to T^3 when temperature is much lower than Debye temperature (below $T_D/50$ [10]). When the Debye temperature or Debye frequency of a solid is known, its heat capacity can be calculated using Eq. (3.17). Or in other words, Debye temperature is a characteristic property of a solid, with which one can calculate the heat capacity of the solid at various temperatures. Debye temperature can also be correlated to EWF. Since $\varepsilon_b / r_e^3 \propto E \propto \varphi^6$, we have $T_D \propto \varepsilon_b^{1/2} / r_e^{3/2}$ and thus $T_D \propto \varphi^3$. Such a relationship is consistent with experimental observations as shown in Figure 3.6.
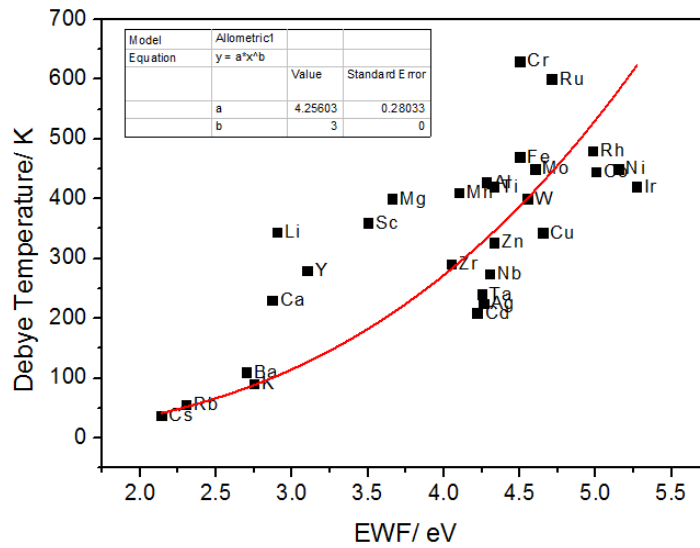
Figure 3.6 Relation between EWF and Debye temperature. Experimental values are given in Table 3.1.

3.3 Discussion

Using the Lennard-Jones potential as a bridge, we have correlated several important material properties to EWF. The relationships between EWF and bulk modulus, thermal expansion and Debye temperature are consistent with reported experimental results. Although data scattering is relatively large (contributed by a number of factors, *e.g.,* experimental error, texture of polycrystalline materials, surface condition, and the simplicity of L-J potential), basic trends are reflected, which demonstrates the effectiveness of the proposed approach and verifies the dependence of the properties on EWF.

The correlation between the bond energy and EWF can be extended to investigate other bond energy-related properties using L-J potential as a bridge. This

new methodology helps generate complementary clues for advanced material design, element selection and modification of bulk materials or phases on a feasible electronic base. As an example, adding appropriate elements with higher EWFs to a material may increase the overall EWF, leading to elevated stiffness and consequently a lowered thermal expansion coefficient.

Although the primary attempt of this study is to demonstrate a simple L-J approach in developing basic or general correlations between EWF and material properties, this approach allows further studies involving crystallographic factors. Since the L-J potential is an inter-atomic pair potential, influences of crystallographic orientations and planes on properties of a solid can be analyzed using the L-J approach as long as (ε_b, r_e) are determined based on the structure and properties of the solid. However, if there is a structural change *i.e.* phase transformation (corresponding to changes in the electron density and thus EWF), ε_b and r_e would be influenced. Thus, (ε_b, r_e) need to be re-determined or re-calculated based on some measured properties of the new structure if one wants to study the new phase using the L-J approach with a certain degree of accuracy.

3.4 Summary

In this study, a simple approach to correlate properties of materials to their EWF is proposed using the Lennard-Jones potential as a bridge. Based on the dependence of Young's modulus on EWF, several bond energy-related properties including bulk modulus, thermal expansion and Debye temperature are correlated to EWF. The established correlations are consistent with reported experimental data.

With this simple and effective approach, it is possible to use EWF as an alternative parameter to depict material behavior and provide complementary clues in advanced materials design and modification.

Chapter 4 Correlations between EWF and properties of solid solutions

Previous studies have demonstrated that mechanical properties of pure metals can be correlated to their EWFs. For instance, Young's moduli, yield strength and hardness of pure metals have a six-power relationship with their EWFs [71,72]. Studies in Chapter 3 correlate EWF to atomic bond energy using Lennard-Jones potential as a bridge. Several bond energy-related properties of pure metals including bulk modulus, thermal expansion and Debye temperature are correlated to EWF [100]. It foresees the possibility to use EWF as an alternative parameter to depict material behavior and provide complementary clues in advanced materials design and modification. However, whether such relationships between EWF and mechanical properties are true for alloys is unclear. This limits the application of EWF in design of realistic materials, which generally consist of multi-elements.

This chapter presents studies of relationships between EWF and mechanical properties of binary solid solutions. The chapter consists of two sections. (1) A method is proposed first to extract EWFs of binary solid solutions or alloys from their phase diagrams. This simple approach is used to predict their mechanical strength and surface properties, such as adhesion. (2) Using isomorphous nickel-copper alloys as an example material without involving microstructure complexity, correlations between EWF and Young's modulus as well as hardness of the alloy with respect to the composition are investigated. How EWF could be used in materials design is also discussed.

4.1 EWF calculations for binary solid solutions based on phase diagram

Phase diagrams provide valuable information on microstructure of materials, which strongly influences material properties. Since the phase diagram can be theoretically determined based on principles of thermodynamics, *e.g.*, free-energy minimization, which are mainly related to atomic interactions, material properties could thus be predicted from the phase diagram. As discussed in Chapter 3, the atomic bonding is intrinsically governed by EWF; thus it is expected that EWF can be extracted from the phase diagram and material properties can be predicted based on the EWF obtained from the phase diagram without involved complicated thermodynamic treatments. In this section, a method to extract the EWFs of binary solid solutions from their phase diagrams is proposed. This study has been published in Lu, H., Huang, X. & Li, D. Understanding the bond-energy, hardness, and adhesive force from the phase diagram via the electron work function. Journal of Applied Physics 116, 173506.[107]

4.1.1 Theoretical details

From the solvus line in a binary phase diagram with the quasi-chemical treatment [108], several important thermodynamic quantities can be determined, including the interaction parameter (Ω) and bond energy between the two elements (ε_{AB}) for a solid solution [70]. According to statistical thermodynamics, the saturated mole fraction of B in the host lattice of element A (phase α), X_B^{sat} (or the

solubility of B in A) shown in Figure 4.1, can be expressed as [109,110]

$$\ln X_B^{sat} = \frac{\Delta S_B}{k_B} - \frac{\Delta H_B}{k_B T} \qquad (4.1)$$

where k_B is Boltzmann constant, T is absolute temperature, ΔH_B is the change in enthalpy when pure B is added to the solution α, and ΔS_B is the excess entropy as the solute B is dissolved into the solution, which is approximately independent of temperature and can be treated as a constant. Thus, the solubility of B in α phase is expressed as

$$\ln X_B^{sat} = C - \frac{\Delta H_B}{k_B T} \qquad (4.2)$$

where C is a constant independent of temperature and ΔH_B consists of two parts, $\Delta H_B^{\alpha\beta}$ and Ω. $\Delta H_B^{\alpha\beta}$ is the change in enthalpy when converting B from crystal structure β to structure α; or in the other word, it is the difference in enthalpy between B in α form and B in β form. If B has the same crystal structure as the host element A (α), then $\Delta H_B^{\alpha\beta}$ is zero. The solubility is generally expressed as

$$\ln X_B^{sat} = C - \frac{\Delta H_B^{\alpha\beta} + \Omega}{k_B T} \qquad (4.3)$$

When $\ln X_B^{sat}$ is plotted versus $\frac{1}{T}$ (data come from the solvus line in the phase diagram), a straight line is obtained and $\Delta H_B = \Delta H_B^{\alpha\beta} + \Omega$ can be determined from the slope of the line. $\Delta H_B^{\alpha\beta}$ is mainly contributed by the internal energy of the crystal or the cohesive energy, which is equal to [10]

$$E_{FCC} = 8.6 N \varepsilon_b, E_{BCC} = 5.6 N \varepsilon_b^{'} \qquad (4.4)$$

where N is the number of atoms in the crystal and ε_b is the atomic bond strength.
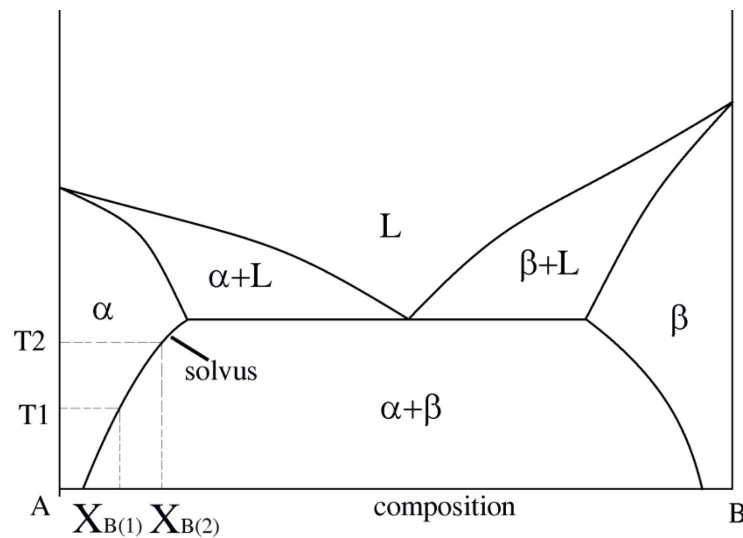
Figure 4.1 Schematic binary phase diagram, X_B is the solubility of B in α phase at temperature T.

Once ΔH_B, $\Delta H_B^{\alpha\beta}$ are determined from Eqs. (4.2) and (4.4), it is possible to determine the interaction parameter, Ω, which is expressed as

$$\Omega = z \cdot \varepsilon \tag{4.5}$$

$$\varepsilon = \varepsilon_{AB} - \frac{1}{2}(\varepsilon_{AA} + \varepsilon_{BB}) \tag{4.6}$$

where z is coordination number of the crystal; ε_{AB}, ε_{AA} and ε_{BB} are bond energies of A-B, A-A, B-B bonds, respectively. ε_{AA} and ε_{BB} can be calculated from the heat of sublimation or heat of vaporization approximately, thus one may determine A-B bond energy, ε_{AB}, from the solubility of element B in phase α or phase diagram using Eqs. (4.1)-(4.6).

According to previous studies and discussions in Chapter 3, Young's modulus of pure metal is related to the atomic bond energy [100] and EWF [71]

$$E \propto \frac{\varepsilon_b}{r_e^3} \quad and \quad E \propto \varphi^6 \tag{4.7}$$

where E is the Young's modulus, ε_b the atomic bond energy, r_e the bond length and φ is EWF. Thus one may correlate EWF to the bond energy as the following equation expressed by

$$\varphi^6 = \xi \cdot \frac{\varepsilon_b}{r_e^3} \tag{4.8}$$

where ξ is the fitted constant based on experiment data for pure metals.

Applying differential treatment to Eq. (4.8), one may estimate the potential errors associated with Eq. (4.8)

$$6\varphi^5 \Delta\varphi = \zeta r_e^{-3} \Delta\varepsilon_b \tag{4.9}$$

Using iron as an example, EWF of Fe is about 4.5 eV, bond length is around 0.25 nm. In general, variations in experimentally measured EWF are usually within 50 meV. Thus, potential errors of calculated bond strength using Eq. (4.8) due to various experimental factors such as the instrument stability and environmental interference in measuring EWF could be around 0.08 eV. Since the bond energy of Fe is 1.07 eV, the relative error would be around $0.08/1.07 = 7.5\%$. Thus, it is reasonably reliable to use Eq. (4.8) to correlate bond energy with EWF.

Statistically, one may calculate the average bond energy of the phase from A-A, B-B, A-B bonds as [70]

$$\overline{\varepsilon_b} = x^2 \cdot \varepsilon_{BB} + (1-x)^2 \cdot \varepsilon_{AA} + 2x(1-x) \cdot \varepsilon_{AB} \tag{4.10}$$

where x is molar fraction of element B in the calculated phase. According to Vegard's law, we may let the average bond length approximately equal to the weight average of the bond length of constituents A and B. Thus, EWF of a solid solution having the host element A with dissolved element B can be calculated from the phase diagram and Eq. (4.11), that is

$$\varphi^6 = \xi \cdot \frac{x^2 \cdot \varepsilon_{BB} + (1-x)^2 \cdot \varepsilon_{AA} + 2x(1-x) \cdot \varepsilon_{AB}}{[x \cdot r_{e,B} + (1-x) \cdot r_{e,A}]^3} \tag{4.11}$$

where $r_{e,A}$ and $r_{e,B}$ are equilibrium atomic spacing of A and B before mixing.

4.1.2 Experimental details

As an example, the above established relationships were used to determine EWF of Fe-Ni solid solutions from a Fe-Ni phase diagram. In this study, Ni was added into X70, a low-carbon steel (0.07 wt% C, 0.5 wt% Mn, 0.3 wt% Cr), using an arc melting furnace. Although minor elements are present, this steel with added Ni more or less represents Fe-Ni solutions. During sample melting and solidification, each sample/ingot was turned over and remelted for a few times in order to minimize the compositional inhomogeneity.

Up to 10wt% Ni was added to the steel to make the Fe-Ni samples. X-ray diffraction (Rigaku XRD Ultimate IV with Cu $K\alpha$ radiation) and scanning electron microscope (Tescan Vega 3 SEM, Czech Republic, with EDX detector provided by Oxford Instrument) analyses were carried out to examine the samples in order to confirm that they are solid solutions without formation of second phases or compositional inhomogeneity.

EWFs of the samples were measured in air at room temperature using a scanning Kelvin probe (SKP 5050, KP Technology Ltd. UK) with a spatial resolution of 400 nm and an energy resolution of 1-3 meV. A reference gold tip with 1 mm diameter was used to measure the contact potential difference between the tip and the sample, and corresponding EWF was calculated. The SKP system does not directly provide absolute EWF of the sample but a value relative to EWF of a standard gold sample (5.1 eV). The absolute EWF of a metal sample can be

calculated by subtracting its relative EWF value from EWF of a standard gold sample. The samples under study were polished using 400, 600, 800, 1200 grit silicon carbide sand papers successively and finally polished in a slurry containing 1μm diamond to get a mirror finish. The polished surface was cleaned using an ultrasonic cleaner with reagent alcohol for 3 min, and its EWF was measured immediately after it was dried in order to minimize the influence of contamination and oxidation. During the measurement, the sample surface was scanned using the SKP over an area of $16\mu m \times 16\mu m$ which covered 25 points. At least three different regions on the samples surface were measured.

Hardness of samples was measured using a micro-indenter (Fisherscope H100C Micro hardness Measurement System, Fisher Technology, Germany). A cone-shaped diamond indenter tip was used and the load was increased linearly up to 600 mN at a rate of 30 mN/s. From the load-indentation depth curve, hardness was calculated automatically. Each sample was measured at least five times. The adhesive force between a silicon nitride tip and the sample surface was measured using an AFM (Digital Instruments Multimode AFM with LFM-2 model). During the test, the tip was in contact with the sample surface first and then pulled away from the surface. The maximum force that held the tip before it left the surface was used to represent the adhesive force.

4.1.3 Results and discussion

4.1.3.1 EWF calculations from phase diagram

XRD patterns and SEM backscattered images of the Fe-Ni samples are illustrated in Figures 4.2 and 4.3, respectively. As shown, no second phases were observed in the XRD patterns and SEM images of X70 samples containing Ni. The sample surfaces were homogeneous without patches resulting from possible second phases or compositional inhomogeneity. Thus, the measured EWF is an average EWF value of a homogeneous solid solution. Experimental and calculated EWFs of the samples are presented in Table 4.1. One may see that EWF increases with increases in Ni content. The EWF calculated from the phase diagram shows the same trend with experimental data, which validates the approach for determining EWF from the phase diagram.
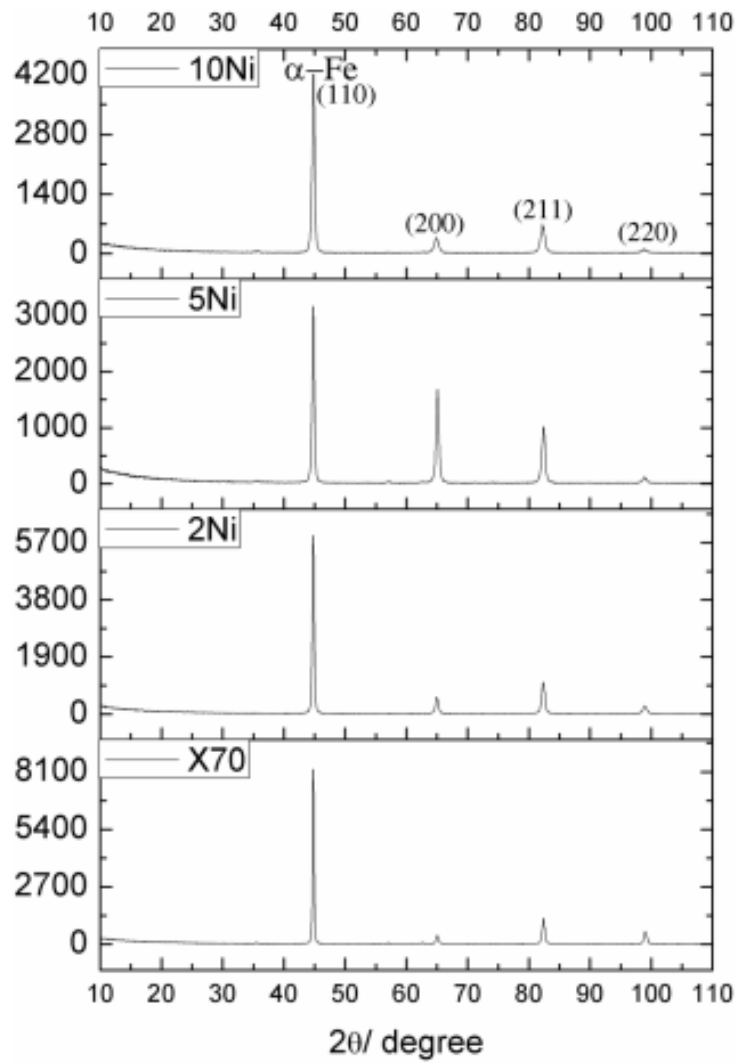
Figure 4.2 XRD patterns of Ni added X70 samples made by arc melting method
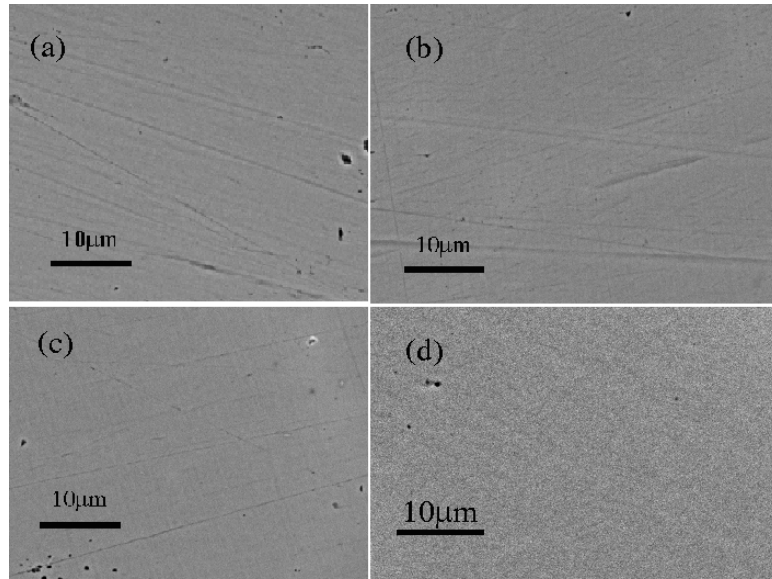
Figure 4.3 SEM backscattered images for (a) X70 (b) X70-2Ni (c) X70-5Ni (d) X70-10Ni

Table 4.1 Calculated EWFs from Fe-Ni phase diagram and measured ones, and corresponding experimental micro-hardness and adhesive force (between the target surface and a Si_3N_4 tip) for the Fe-Ni alloys

	X70 (Fe)	X70 (Fe)-2Ni	X70 (Fe)-5Ni	X70 (Fe)-10Ni
EWF (exp.) / eV	4.260 ± 0.023	4.33 ± 0.034	4.41 ± 0.028	4.445 ± 0.023
EWF (cal.)/ eV	4.127	4.141	4.158	4.185
Hardness/ HV	190.7 ± 8.5	259.4 ± 8.7	266.5 ± 16.5	319.7 ± 16.4
Adhesion/ nN	16.125	12.750	9.750	8.375

However, the calculated EWFs are systematically lower than the measured values with an average difference of -0.21eV or an average percent deviation of

-4.8%. This difference could be attributed to the following possible factors:

1) Surface oxidation – although EWF of the samples were measured right after polishing and cleaning, oxidation could more or less occur on surface of carbon steel, which may slightly raise its EWF by blocking electron escape from the surface when a potential is applied.

2) Possible surface adsorption – Since the sample was exposed to air, adsorption likely occurred as a result of surface energy minimization. An adsorption layer usually stabilizes the surface and could thus raise the surface EWF. A dipole layer may form on surface, which could lead to an increase in EWF.

3) Deviation from equilibrium – The sample was, having a button shape with a diameter of 1 cm, prepared in an arc melting furnace. After melting, it was cooled in a copper bath at a high cooling rate. Thus, the solidification process was apart away from the thermodynamic equilibrium state. Since the phase diagram only deals with the equilibrium state, the realistic solubility is higher than that shown in the phase diagram. Such a difference in solubility could influence the calculated EWFs, resulting in deviation from measured ones.

4) Influence of minor elements on EWF – X70 steel contains minor elements (0.5 wt% Mn, 0.3 wt% Cr), while the calculation was conducted for a pure Fe-Ni system. This may also lead to difference in EWF between calculated and measured values.

In order to further confirm or verify the feasibility of the approach proposed to determine EWF from phase diagram, Cu-Zn system was also studied as another

sample material. All performed tests and calculation are similar to those for studying the Fe-Ni system. The calculated and experimentally measured EWFs are presented in Table 4.2.

Table 4.2 EWFs calculated from a Cu-Zn phase diagram and measured ones

	Cu	Cu-2Zn	Cu-5Zn	Cu-10Zn
EWF (exp.) / eV	4.673 ± 0.026	4.634 ± 0.022	4.563 ± 0.025	4.478 ± 0.038
EWF (cal.)/ eV	4.858	4.846	4.828	4.796

The calculated and measured EWFs have similar trend, both of them decrease as the amount of added Zn is increased. This further validates the approach for determining EWF from the phase diagram.

4.1.3.2 Prediction properties based on calculated EWF

Once EWF of an alloy is determined from the phase diagram, one may predict properties of the alloy. In this study, hardness and adhesive force are analyzed as examples.

If a metal or alloy has a higher EWF, a greater energy is required to change its electron state. This consequently generates a larger barrier to any attempts to change its other states or properties, including mechanical strength and corrosion resistance, which are related to the bond strength and electron activity [111,112]. For instance, metals having higher EWFs possess stronger atomic bonds, corresponding to higher Young's moduli [71]. The stronger bonds also make it harder to activate dislocations, leading to increased hardness [72]. In this study, hardness of the Ni-added samples

was tested using the micro-indentation method and results are shown in Table 4.1. One may see that when Ni is added, both EWF and hardness of the steel increase, and hardness has an intrinsic sixth power relationship with the EWF as demonstrated previously [72].

$$H = \alpha \cdot \varphi^6 / (1 - \upsilon^2) \tag{4.13}$$

where υ is the Poisson's ratio, α is a constant which is equal to 0.011. A fitted hardness ~ EWF curve is illustrated in Figure 4.4, in which an experimental curve is also presented for comparison. The calculated and experimental curves are consistent. Differential treatment was also applied to Eq. (4.13) to analyze potential error.

$$\left(1 - \upsilon^2\right) \cdot \Delta H = \alpha \cdot 6 \varphi^5 \cdot \Delta \varphi \tag{4.14}$$

The measured EWF is around 4.3 eV and the experimental errors are about 30meV, Poisson's ratio for steel is about 0.29. Thus, based on Eq. (4.14) the potential error of hardness is around 3.2 or potential percent error around 1%-1.6%, which is smaller than the experimental data deviation. This indicates the feasibility of using EWF to predict hardness using Eq. (4.13).
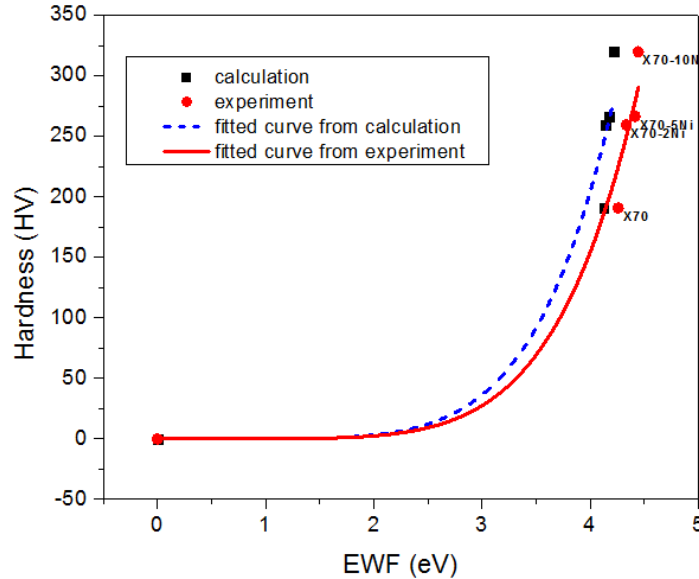
Figure 4.4 Correlation between EWF and hardness

Adhesion is the tendency of two different surfaces to cling to each other, which plays an important role in many surface processes, such as friction, wear, and bacterial binding [66,67,113], *etc*. Adhesion can be evaluated using the atomic force microscope (AFM). The adhesive force between the sample and an AFM tip is determined by measuring the deflection of the AFM cantilever when the tip is in the vicinity of the sample surface (or more precisely the adhesive force is the maximum force that attracts/holds the tip before it leaves the surface). The higher the EWF of a surface, the lower is its adhesive force, as shown in Table 4.1 and Figure 4.5. This trend is ascribed to the fact that the adhesive force is related to the surface reactivity or electron activity [18,114], which can be characterized by EWF. A higher EWF corresponds to a stronger atomic bond and higher surface energy [64,65,100]; thus the surface with higher EWF is easier to react with the environment to form a passive film. The passive film blocks the electrons for further reactions and thus the surface

with higher EWF has lower activity and thus lower adhesion. Adhesion is crucial to friction and wear of materials, especially for components in nano/micro-devices where the contact forces are rather light and deformation is negligible. Thus, the correlation between EWF and adhesion could be used to study friction and tribology phenomenon under light loads or in micro/nano-machines with contact forces.
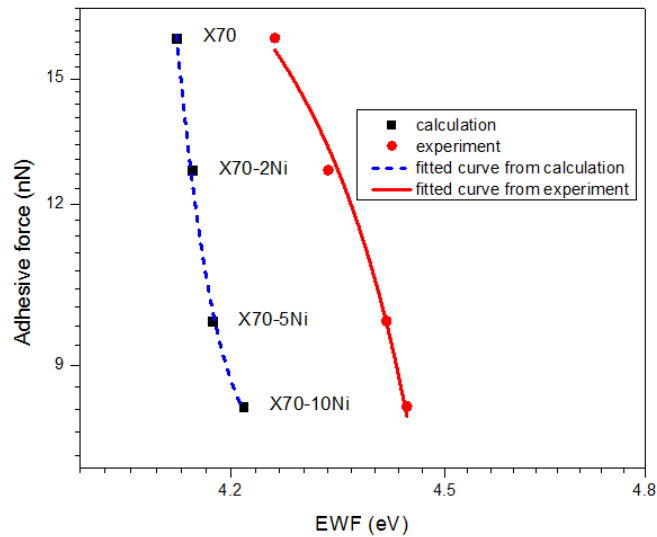
Figure 4.5 Correlation between EWF and adhesive force

4.1.4 Remarking comments

EWF of a solid solution could be extracted from its phase diagram and used to evaluate or predict mechanical properties, surface activity such as adhesion, and other properties that are related to EWF. Using Ni added X70 low-carbon steel and Cu-Zn alloys as sample materials, EWFs of the materials were calculated from their phase diagrams, which showed trends similar to those that were experimentally measured. Corresponding hardness and adhesive force were analyzed, results of

which were consistent with experimental measurements. This study demonstrates an alternative approach to predict materials properties based on EWF extracted from the phase diagram. This approach would also help maximize the power of phase diagram for material design and development.

4.2 Dependence of the mechanical behaviors of solid solutions on EWF

A method to extract the EWFs of binary solid solutions from their phase diagrams was proposed in section 4.1. The study demonstrates an alternative approach to predict materials properties based on EWF extracted from the phase diagram. However, it still lacks theoretical analysis of the relationships between EWF and mechanical properties of binary solid solutions, which limits the application of EWF in predicting materials properties and design of realistic materials. The objectives of this study are to investigate and demonstrate the correlation between EWF and mechanical properties of the alloy and to discuss how EWF could be used in materials design. This study has been published in Lu, H., Hua, G. & Li, D. Dependence of the mechanical behavior of alloys on their electron work function—An alternative parameter for materials design. Applied Physics Letters 103, 261902 (2013).[115]

4.2.1 Experimental details

Pure copper (99.9 wt %) and pure nickel (99.9 wt %) provided by Strem Chemicals were used to synthesize Cu-Ni alloy samples with different compositions

using an arc melting method. All samples were annealed (homogenization) in argon atmosphere at 600 °C for 3 h and slowly cooled down in the furnace. The annealed samples were polished using 400, 600, 800, 1200 grit sand papers successively and finally polished in a slurry containing 1 μm diamond to get a mirror finish.

EWF of samples was measured by ultraviolet photoelectron spectroscopy (UPS). UPS analysis was made in ultrahigh vacuum and ultraviolet light was used as the excitation light source. Absolute EWF of a sample was determined by measuring the kinetic energy of photoelectrons emitted from samples. Helium I was used as the light source for the UPS measurement. The pass energy of the instrument was 5 eV and a 110 μm aperture was used to collect light. All the sample surfaces, each of which had an area of 2.5 mm × 2.5 mm, were sputtered using argon ion for 4 min to remove any possible adsorbed substances on the surface before measurement, since the EWF is very sensitive to surface contamination. The measurement was conducted immediately after sputtering to make sure that the sample surfaces were clean without contamination. The instrument was operated in ultra high vacuum of 3×10^{-8} torr.

Cu-Ni samples with various Ni concentrations were polished under the same condition and sputtered by argon ions before their EWFs were measured, so that the influences of surface roughness, oxide film, and a possible adsorption layer on the EWF were minimized in order to obtain reproducible EWF measurement results.

Young's modulus and hardness of Cu-Ni alloys with respect to the concentration of Ni were measured using the micro-indentation method. A cone-shaped indenter tip was used and the load was applied to the indenter with a

linear increase of 300 mN/20 s. From the load-indentation depth curve, hardness and Young's modulus were determined automatically.

4.2.2 Results and discussion

4.2.2.1 Experimental results

Figure 4.6 illustrates SEM images of three representative Cu-Ni samples, in which no second phases are present. Thus, the measured EWFs are the overall values of the isomorphous alloy samples.
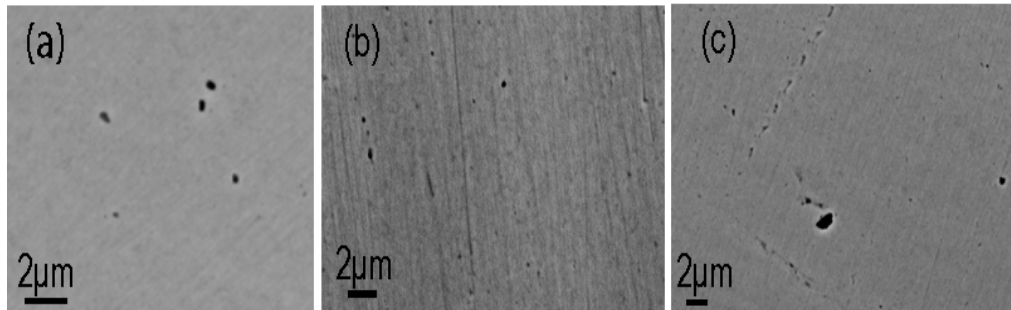
Figure 4.6 SEM backscattered images of samples with (a)90 wt% Ni, (b) 50 wt% Ni, and (c)20 wt% Ni

The EWFs of samples with different compositions were determined from the UPS spectra. Figure 4.7(a) presents measured EWF values with respect to the concentration of Ni (at %), which illustrates that the EWF increases as the Ni concentration increases. Figure 4.7(b) and (c) show EWF calculated using the image model [51,52,116] and the first-principles method, respectively. The calculated influence of Ni on the EWF is consistent with that determined experimentally.
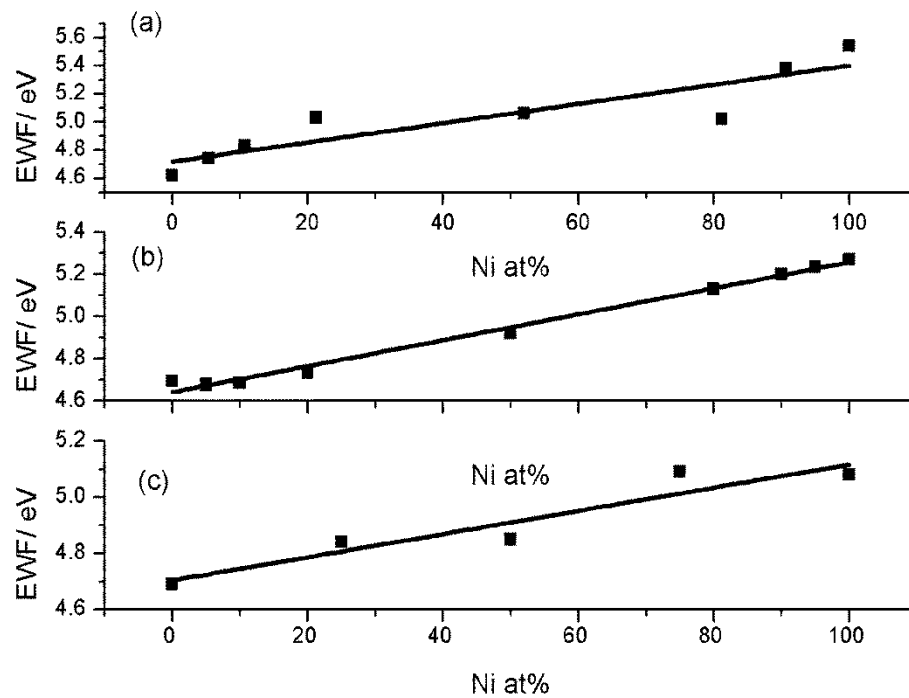
Figure 4.7 (a) EWFs measured with UPS; (b) EWFs calculated using the image model; and (c) EWFs calculated using the first-principles method [for (111) plane].

As shown in Figure 4.8, both Young's modulus and hardness increase with an increase in %Ni. Such changes are related to an increase in overall EWF as the Ni concentration increases. The relationships between the mechanical properties and EWF can be fitted by sixth-power curves as Figure 4.9 illustrates *i.e.*, $E = \beta\varphi^6$, where β is a constant for metals [71,72]. It should be pointed out that since the values of EWF fall into a small range with respect to at%Ni, the sixth-power relationships may not be seen clearly. However, it has previously been demonstrated such relationships based on theoretical analysis and collected experimental data as

81

discussed in section 2.2.4.4 and section 2.2.4.6.
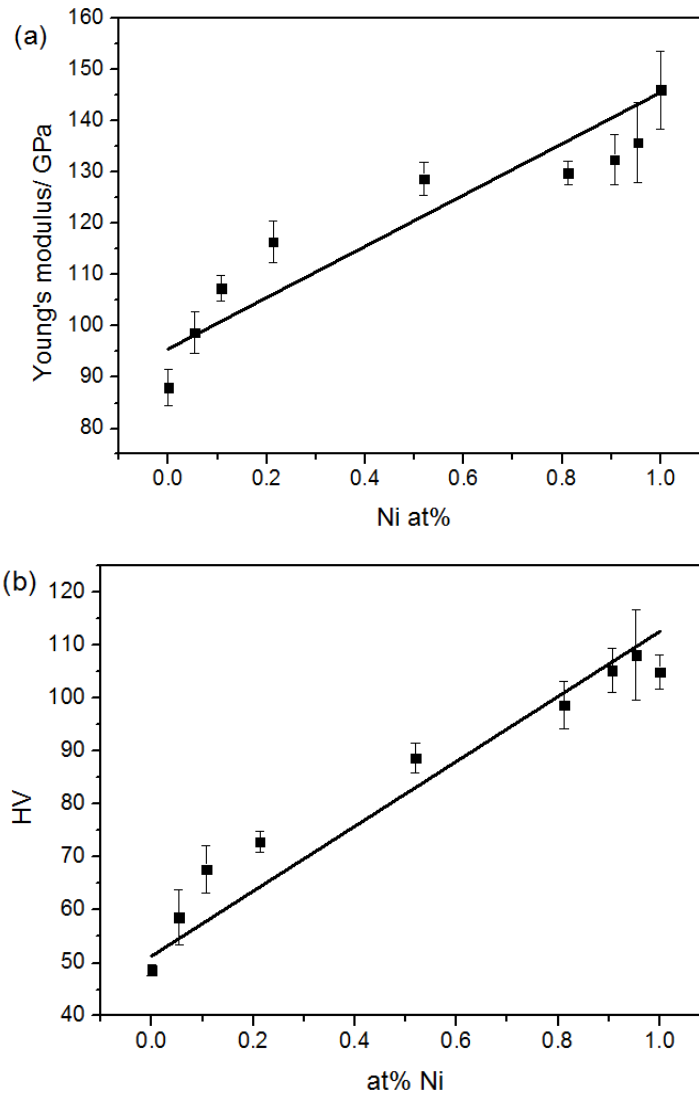
Figure 4.8 Young's modulus (a) and hardness (b) of Cu-Ni alloys as a function of at%Ni, measured using the micro-indention method.
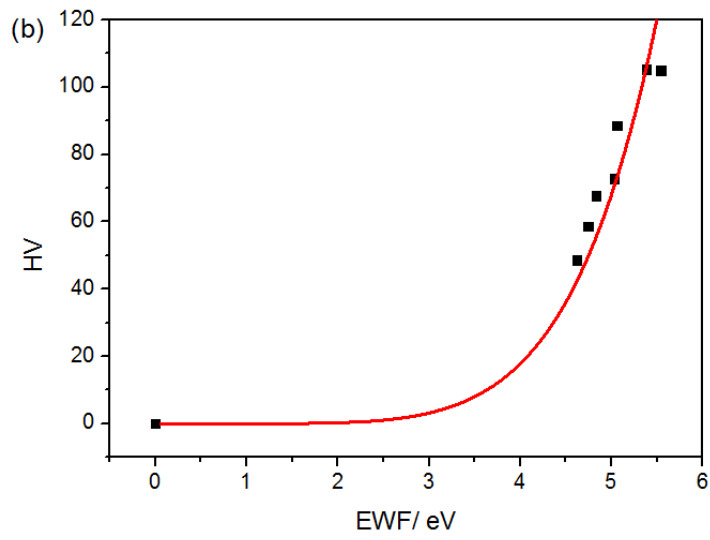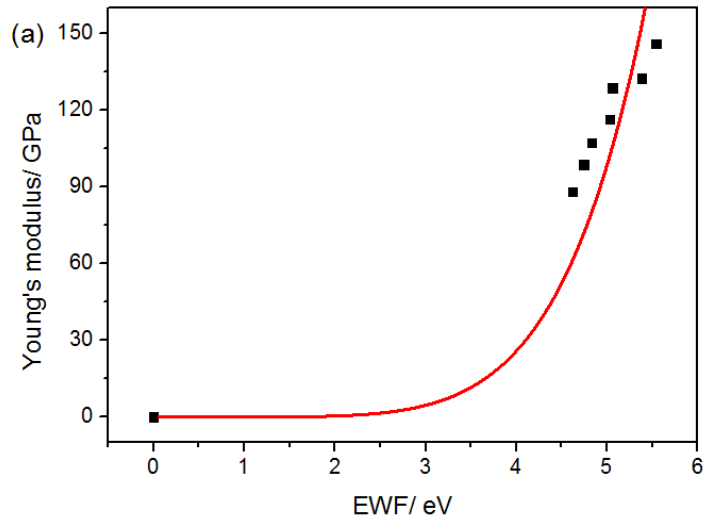
Figure 4.9 The fitted curve of Young's modulus (a) and hardness (b) as a function of the EWF of alloys based on the experimentally obtained data.

4.2.2.2 Theoretical analysis

In order to analytically describe the trend of EWF *vs.* composition, we may express the EWF (φ_{AB}) of an alloy, A_xB_{1-x}, using the following equation derived based on an image charge model,

$$\varphi_{AB} \propto n_{AB}{}^{1/6} \approx 7.8 n_{AB}{}^{1/6} = 7.8 \frac{z_{AB}{}^{1/6}}{a_{AB}{}^{1/2}} \tag{4.15}$$

where z_{AB} is the valence number of the alloy and n_{AB} is the corresponding electron density. a_{AB} is the lattice constant of the alloy. Since $Z_{AB} = X_A Z_A + X_B Z_B$ and $a_{AB} = X_A a_A + X_B a_B$ according to Vegard's Law [117], we have

$$\varphi_{AB}^6 \propto \frac{X_A Z_A + X_B Z_B}{(X_A a_A + X_B a_B)^3} \approx 7.8[\frac{X_A n_A}{(X_A + X_B a_B / a_A)^3} + \frac{X_B n_B}{(X_B + X_A a_A / a_B)^3}] \tag{4.16}$$

where X_A, X_B are molar fractions of A and B, respectively, and $X_A + X_B = 1$. For the Cu-Ni system, $Z_{Cu} = 2$ and $Z_{Ni} = 2.5$ [51] were used for EWF calculation. The lattice constants of Ni and Cu are 0.352 nm and 0.361 nm, respectively.

Since lattice constants of two components, which can be homogeneously dissolved in each other forming an isomorphous solution, are generally close, one may approximately let $a_A = a_B$, so that

$$\varphi_{AB}^6 \approx 7.8[X_A n_A + X_B n_B] = X_A \varphi_A^6 + X_B \varphi_B^6 \qquad (4.17)$$

According to Eq. (4.17), when a metal with a higher EWF is added to the host metal, the overall EWF increases. It is consistent with the experimental observations shown in Figure 4.7.

The sixth-power relationship between EWF and Young's modulus of pure metals should also apply to isomorphous alloys and we may have the following equation to explain the experimental observation as shown in Figures 4.8 and 4.9:

$$E_{AB} = \beta \varphi_{AB}^6 = \beta(X_A \varphi_A^6 + X_B \varphi_B^6) = X_A(\beta \varphi_A^6) + X_B(\beta \varphi_B^6) = X_A E_A + X_B E_B \quad (4.18)$$

This equation is consistent with the experimental observations, which verifies the sixth-power relationship for the isomorphous alloy.

The demonstrated relationships between the mechanical properties and EWF can be explained based on the fact that when a metal has a higher EWF, a greater energy is required to change its electron state. This consequently generates higher barriers to any attempts to change its mechanical state, electrochemical state or other ones, which are related to the electron state-governed atomic bond strength. Young's modulus is regarded as an intrinsic property, since it is directly related to the atomic bond strength. When Ni with a higher EWF is added to Cu, the overall EWF increases, corresponding to a stronger atomic bond between adjacent Cu and Ni atoms or a larger barrier to the separation of a Cu-Ni atomic pair. Stronger bonds also raise barriers to generation and movement of dislocations, leading to elevated hardness. It should be indicated that the increase in hardness is, however, less

intrinsic, since it is influenced by other factors related to dislocation generation and movement.

4.2.2.3 The significance of EWF-property-composition relationships in materials design

EWF reflects the stability of electron state or the difficulty to break an atomic bond. Thus, EWF could be a parameter for predicting or determining mechanical and electrochemical stabilities of a solid, particularly for metallic materials. Logically, adding an element having a higher EWF to a host metal may raise the overall EWF as Eq. (4.17) suggests and could thus enhance the atomic bonding and consequently the mechanical strength. For instance, an interface between substances A and B could be strengthened by adding an element C based on its EWF as a simple parameter for the third element selection. The selected element should have its EWF higher than those of both components A and B. Thus the interfacial zone in which a portion of A-A, B-B and A-B bonds are replaced by A-C, B-C and C-C bonds has elevated EWFs and bond strengths. Such a criterion should also be applicable for selection of elements for solution-strengthening without generating second phases, and could be extended to tailoring bulk alloys and phases with more complicated structures.

To determine whether this hypothesis works, we added small amounts of yttrium ($\varphi_Y = 3.1$eV, which is lower than those of Cu and Ni) and platinum ($\varphi_{Pt} =$ 5.32-5.65 eV, which is higher than those of Cu and Ni [61]) respectively to the Cu-Ni alloy, and then determined corresponding changes in EWF and mechanical

properties of the Cu-Ni alloys. Pure yttrium (99.9 wt %) from Aldrich and pure platinum (99.9 wt %) from Strem Chemicals were used to synthesize Cu-Ni alloy samples with respectively added Y and Pt. 4%Y and 4%Pt were added to 50%Ni-50%Cu, respectively. All samples were made by arc melting method and homogenized under argon atmosphere at 800 °C for 3 h. EWF were measured with UPS after polishing under the same condition as described earlier. There were no visible second phases observed in the samples, so the measured EWF basically reflects the overall EWF of each sample.

Variations in EWF and Young's modulus of 50Cu-50Ni caused by Y and Pt, respectively, were measured. Results of the measurements are illustrated in Figure 4.10 with an attached table in which values of the measurement are presented. As shown, adding yttrium with a lower EWF decreases the overall EWF and corresponding Young's modulus, while adding Pt with a higher EWF increases both EWF and Young's modulus.

It should be pointed out that the present study is focused on homogeneous materials without the presence of second phases in order to avoid microstructure complexity. As the small amount of Y or Pt was added to the isomorphous Cu-Ni alloy, respectively, no obvious second phases were observed under a scanning electron microscope. Thus, possible microstructure effects could be excluded or minimized.

	50Cu-50Ni	4%wt Y	4%wt Pt
EWF (eV)	5.01	4.90	5.06
E (GPa)	125.9	107.3	134.3
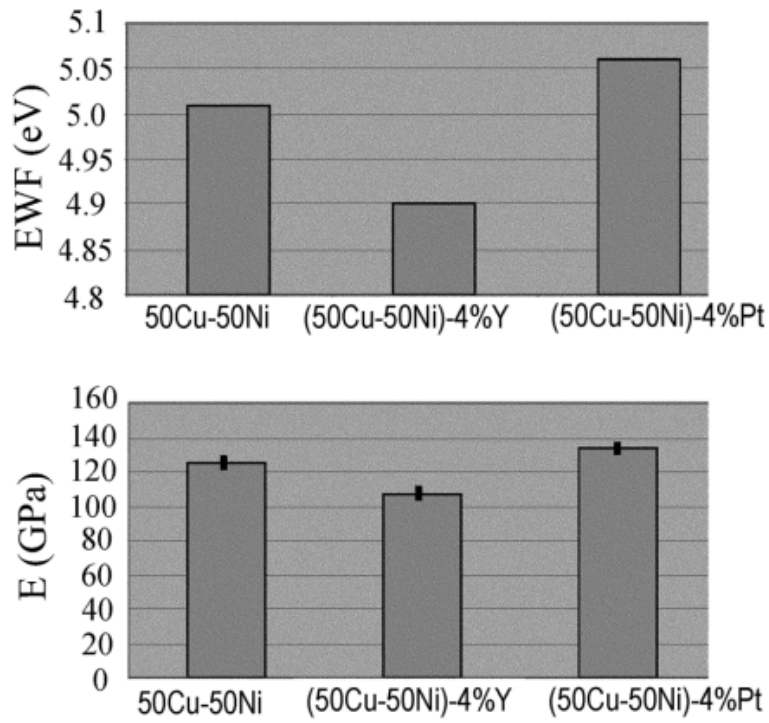
Figure 4.10 Effects of Y and Pt on EWF and Young's modulus of 50Cu-50Ni. The given values of Young's modulus are averaged over at least five measurements for each. The given values of EWF are averages over three UPS scans, which are almost the same (i.e., very reproducible).

4.2.3 Concluding comments

Using isomorphous nickel-copper alloys as an example material without involving microstructure complexity demonstrates that there is a clear correlation between EWF and Young's modulus as well as hardness of the alloy with respect to the composition. As shown experimentally and theoretically, Young's modulus and hardness of the alloy increase as the EWF increases in a sixth power relationship approximately. The EWF of a Cu-Ni alloy was modified by adding a third element with a higher (Pt) or lower (Y) EWF, leading to corresponding increases and decreases in the mechanical strength. This study demonstrates that EWF could be used as a guiding parameter for material design, *e.g.*, selection of appropriate alloying elements for solution-hardening. This promising parameter could build a bridge towards the development of alternative or complementary approaches or methodologies for materials design on a feasible electronic base.

4.3 Summary

In this chapter, relationships between EWF and mechanical properties of binary solid solutions are investigated. A method is proposed first to extract EWFs of binary solid solutions or alloys from their phase diagrams. This simple approach is used to predict alloy properties based on their EWFs. Then using isomorphous nickel-copper alloy as an example material without involving microstructure complexity, correlations between EWF and Young's modulus as well as hardness of the alloy with respect to the composition are investigated. Clear correlations between EWF and Young's modulus as well as hardness of the alloy with respect to

the composition are shown both experimentally and theoretically. How EWF could be used in advanced materials design, *e.g.*, selection of appropriate alloying elements for solution-hardening is also discussed. It demonstrates that EWF could be used as a guiding parameter for material design. This promising parameter could provide an alternative or complementary approaches or methodologies for materials design on a feasible electronic base.

Chapter 5 An EWF based mechanism for solid solution hardening

Solid solution hardening is one of common methods to increase hardness of metals by adding solute atoms. Studies in Chapter 4 propose a simple approach to extract EWFs of binary solid solutions or alloys from their phase diagrams. Clear correlations between EWF and Young's modulus as well as hardness of the solid solution alloy with respect to the composition are demonstrated both experimentally and theoretically. As shown, EWF reflects the stability of the electron state or the difficulty to break an atomic bond and suggests that adding an element with higher EWF than the host element may raise the overall EWF and thus enhance the mechanical strength of the material. However, this study does not consider the influence of size difference between the solute and host atoms in solution hardening. It is known that the mechanism for solution hardening is ascribed to the differences in atomic size and elastic modulus between the host and the solute. In this chapter, the conventional solid solution hardening mechanism is re-examined and a single-parameter model using EWF as an indicator to evaluate the capability of solute atoms in solid solution hardening is proposed.

5.1 Introduction

The resistance of a metal to plastic deformation depends on its barrier to dislocation movement. The basic principle for strengthening metallic materials is to block dislocation motion [22]. Solid solution hardening is one of the most used methods to increase hardness of metals by adding solute atoms, which pin

dislocations, leading to raised yield strength and hardness.

Although solution hardening is widely used to strengthen materials, the selection of alloying elements is largely based on experience. Trial-and-error experiments are generally needed, which are time-consuming and costly. Considerable studies have been conducted to investigate the mechanism for solution hardening. The strengthening of metals by solute atoms is often attributed to the difference in atomic size between solute and host atoms, which help reduce the strain introduced by dislocations and thus pin the dislocations. The classic theory proposed by Mott [118,119] analyzes the average magnitude of stress in the matrix of a dilute solid solution with the alloying element having its atomic size different from that of the host. The effectiveness of solution hardening is related to the magnitude of local distortion, caused by atomic size misfit as $\delta_a = \left(\frac{1}{a}\right) \cdot \left(\frac{da}{dc}\right)$, where a is lattice constant and c is the concentration of the solute. Another contributing factor is the modulus misfit [26] or the difference in elastic modulus between the host and the solute, which is related to the valence number of solute atoms [26]. By taking into account the interaction between dislocation and solute atoms with different values of stiffness [26,120], Fleisgher indicated that the effectiveness of solution hardening through the interaction between dislocation and solute atom was governed by the differences in both rigidity and atomic size between the solute and solvent elements. The effect of modulus misfit on the solution hardening is evaluated as defined as $\delta_G = \left(\frac{1}{G}\right) \cdot \left(\frac{dG}{dc}\right)$, where G is shear modulus. It is suggested that $\delta_h = \left|\delta_G - \alpha\delta_a\right|$ is a measure of the solution hardening effectiveness, where α is an experimentally determined constant through data fitting and the α value is also influenced by the type of dislocations [121,122]. The model indicates the solute-hardening mechanism but

does not show the mutual influences of these two factors and how to maximize the hardening effectiveness by selecting an appropriate solute. It should also be noted that the modulus misfit $\delta_G = \left(1/G\right) \cdot \left(dG/dc\right)$ may be experimentally measureable but it is difficult to be calculated theoretically, since the misfit is influenced by not only the electron-nuclei interactions but also the size misfit δ_a, which distorts the crystal lattice and thus affects the resistance of the crystal to plastic deformation. Although considerable studies were conducted to identify effective approaches to optimally balance the size misfit and modulus misfit such as application of the formula, $\delta_h = \left|\delta_G - \alpha\delta_a\right|$, for different categorized conditions [121], it still does not provide clear guidelines for optimal solute selection. Due to the uncertainty of the constant α and complex dislocation-solute interactions, it is difficult to determine how the size misfit and the modulus misfit synergistically influence the solution hardening [123]. Inaccurate or incorrect predictions could occur.

Furthermore, it is often stated that both larger and smaller solute atoms, relative to the solvent or host atom, can strengthen metals. A larger solute may stay in the tensile region of an edge dislocation while the smaller one may stay in its compressive region, so that the dislocation can be pinned. However, it must be indicated that elements with small atomic sizes are generally stronger with high elastic modulus than those with larger atomic sizes [74], meaning that the size factor and modulus factor are intrinsically related. Thus, these two factors cannot be taken into account separately. This often results in conceptual misinterpretation and makes it difficult to determine the optimal balance between the two factors for maximized strengthening effectiveness. It is therefore highly desired to have a more

straightforward theory or approach to guide element selection for solid solution hardening with more precise understanding.

Efforts have been made to correlate solution hardening to electron configurations based on quantum mechanics with the help of first-principles calculations [29,124] and classic approaches [1,2]. These treatments are, however, complicated and difficult to be used in material design. Identifying a simple but fundamental parameter which characterizes the electron behavior of materials would be greatly helpful. Since EWF reflects the metallic bond strength and is related to atomic size of elements, it is, therefore, possible to use EWF as a bridge to connect the size misfit and modulus misfit in order to obtain clues for maximized hardening effectiveness. Confirmation of this hypothesis and development of a corresponding theoretical base are objectives of this study.

5.2 Experimental details

Pure copper, nickel, zinc and gallium, provided by Alfa Aesar and Strem Chemicals with at least 99.9% purity, were used to make Cu-X solid solution samples (X=Ni, Zn, Ga) with solute atomic concentrations of 2%, 5%, 10%, up to 20%, respectively. The samples were made using an induction furnace provided by MTI Corporation (U.S.). All samples were made under the same condition and melted twice in order to reduce the microstructural inhomogeneity. Rockwell hardness tests using a 1/16'' tungsten carbide ball were performed under a load of 15 kg. Two samples for each alloy and at least five different regions on each sample were analyzed for statistically reliable results. Microstructures of the alloys were characterized using a Vega-3 TESCAN scanning electron microscope and a Rikagu

X-ray diffractometer with Cu Kα radiation in order to make sure the alloys are homogeneous solid solutions without the formation of second phases.

5.3 Experimental results

X-Ray diffraction patterns of all samples and the scanning electron microscope backscattered electron images of the samples with highest concentration of solute atoms are illustrated in Figures 5.1 and 5.2, respectively. No second phases were observed in the XRD patterns of all samples. SEM examination also confirms that the samples are homogeneous without patches resulting from possible second phases or compositional inhomogeneity (Figure 5.2), indicating that the samples are solid solutions. Since all as-cast samples were made under the same condition, the strengthening discussed below should result from solution hardening without other strengthening mechanisms being involved.
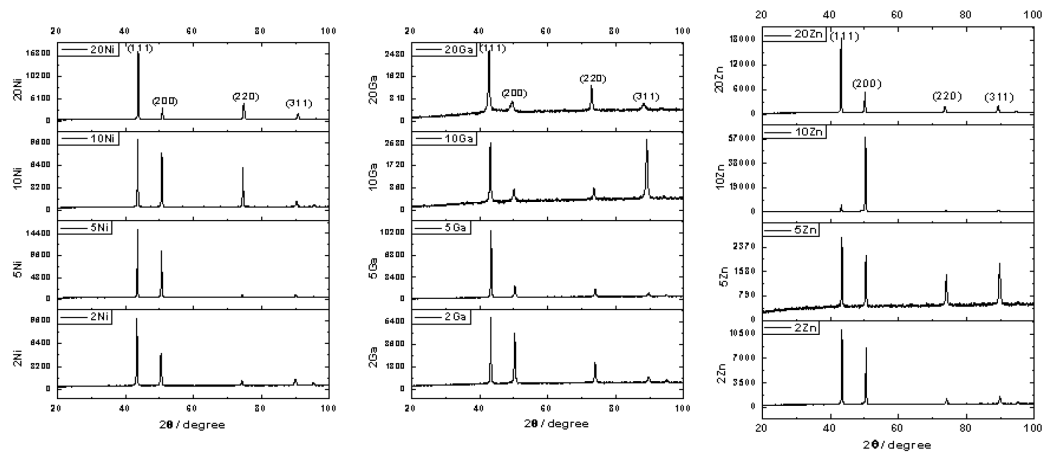
Figure 5.1 XRD patterns of Cu-X samples (X=Ni, Ga, Zn) gotten from Rikagu X-ray diffractometer with Cu Kα radiation. Concentrations of the solute atoms are2%, 5%, 10%, 20%, respectively. No peaks for second phases are detected.

95
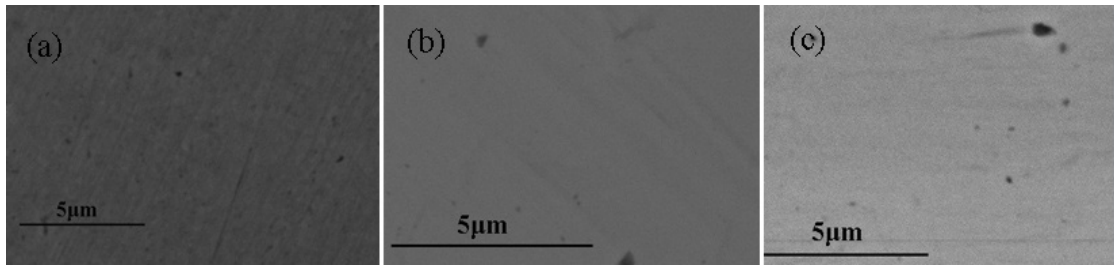
Figure 5.2 Backscattered electron images of samples with highest concentration of solute atoms (a) Cu-20Ni (b) Cu-20Ga (c) Cu-20Zn. All samples are homogeneous without any patches resulting from possible second phases or compositional inhomogeneity.

Hardness of the samples is shown in Figure 5.3. As illustrated, all the solute elements hardened copper. The effectiveness of solution hardening increases as the concentration of solution atoms increases. Nickel is the most effective solute to harden copper, followed by gallium; zinc shows the weakest effect to harden copper, which is consistent with general experience [125].
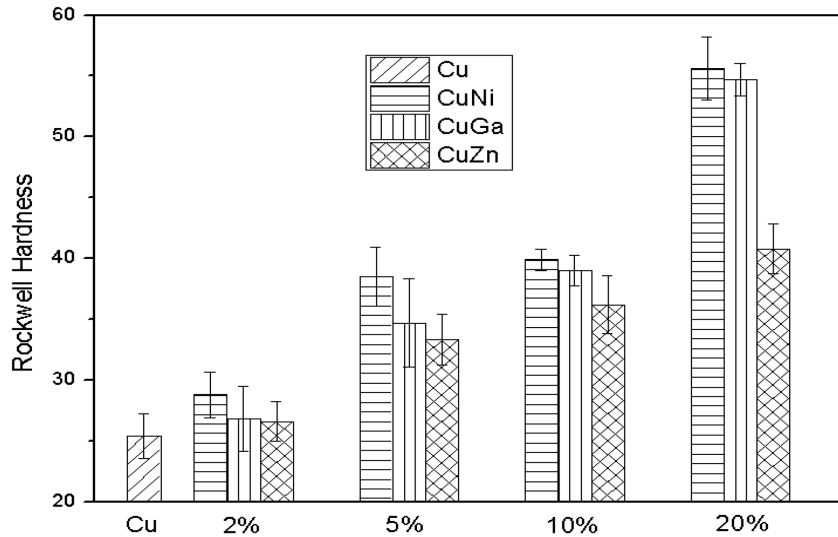
Figure 5.3 Hardness of samples with different compositions. Hardness was tested under a load of 15kg with a 1/16" tungsten carbide ball. All solutes harden pure copper. Nickel is most effective solute to harden copper, followed by gallium, and zinc is the least effective. The effectiveness of solution hardening increases as the concentration of solution atoms increases.

According to the classical theory [26,118-122], the order of strengthening effectiveness is influenced by both the atomic size misfit and modulus misfit. However, although this is known in principle, it is difficult to directly determine such an order based on the size misfit, modulus misfit and unknown constant α (an empirical constant) in the equation of $\delta_h = \left|\delta_G - \alpha\delta_a\right|$. Table 5.1 lists atomic sizes and moduli of the elements under study. If only considering the differences in atomic size and modulus, one may see that Ni has a larger modulus misfit but smaller size misfit with Cu, compared to Zn, implying that the modulus misfit may have a larger influence on the strengthening effectiveness. Thus, Ga should be more

effective than Ni to strengthen copper according to $\delta_h = |\delta_G - \alpha\delta_a|$. This appears not to be the case. Furthermore, the sign of misfit δ_a affects $\delta_h = |\delta_G - \alpha\delta_a|$, meaning that smaller and larger solute atoms, relative to the host atom, would generate different strengthening effects. This is inconsistent with current interpretation regarding how the solute atoms pin dislocations for solid solution hardening. Although efforts were made to suggest different ways to combine the two hardening effects of size misfit and modulus misfit [121], it is difficult to extract clear clues from the previous theory to analyze the present experimental observations.

Table 5.1 Atomic size misfit, modulus misfit and EWF of different solute atoms, atomic sizes are cited from [22], moduli are cited from [22,126], EWF cited from [61]

Solute	Atomic size (radius) misfit	Radius (pm)	Shear modulus G (ΔG), GPa	Young's modulus, GPa	Electron work function (φ), eV	$\Delta\varphi$, eV
Ni	-2.3%	125	76 (30)	207	5.15	0.50
Zn	3.9%	133	43 (- 3)	108	4.33	-0.32
Ga	-4.7%	122	~ 0 (- 46)*	9.8	4.15-4.20	-(0.5-0.45)
Cu		128	46	110	4.65	-

*The melting temperature of Ga is 29.76 °C; its G is very low at room temperature.

5.4 EWF model for solid solution hardening

In order to identify an appropriate balance between the size misfit and modulus misfit, an approach is proposed to connect he two strengthening effects using EWF

as a bridge. EWF of a metal is related to its atomic bonding strength [45] and reflects the confinement of valence electrons to the nucleus. Thus, EWF is correlated not only to atomic bonding or elastic modulus but also atomic size. Previous studies have demonstrated that EWF is related to bond strength and adding elements with higher EWFs raises the overall EWF and the hardness of the host metal as discussed in Chapter 4 [115].The atomic size of elements is also related to their EWFs [74] as discussed in section 2.2.4.9 and shown in Figure 5.4. A model for evaluating the solid-solute hardening effectiveness can be achieved through the following two paths.
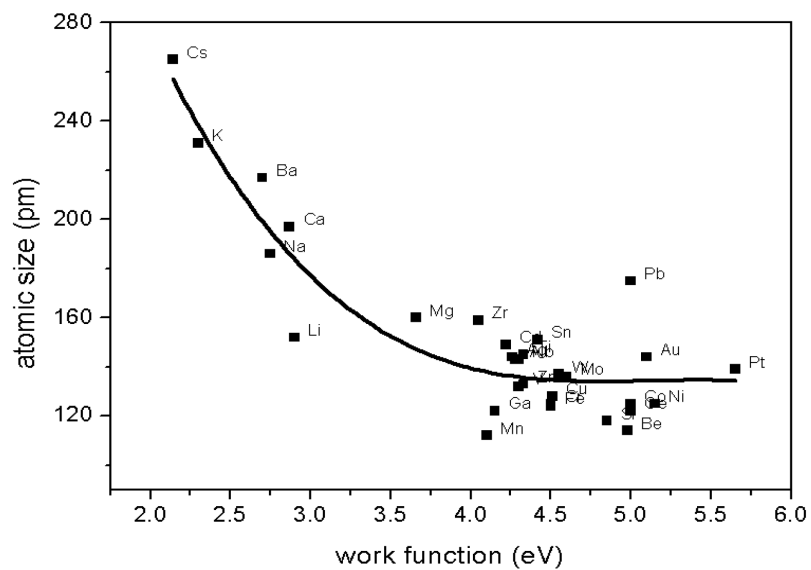
Figure 5.4 Atomic radius of elements vs. EWF, atomic sizes are cited from [22], EWF cited from [47]

5.4.1 Path one: effectiveness based on dislocation driving force

According to the Fleischer's continuum elasticity scheme model [26,120], the interaction energy of a solute atom with dislocations is expressed as

$$E_b^{\text{e}} = \frac{Gb^4 \omega_b y}{2(x^2 + y^2)} \qquad (5.1)$$

$$E_G = \begin{cases} E_G^e = \dfrac{\Delta Gb^5}{8\pi^2(1-\upsilon)(x^2+y^2)} & \text{For edge dislocation} \\[3mm] E_G^s = \dfrac{\Delta G(b/2)^3 b^2}{6\pi^2(x^2+y^2)} & \text{For screw dislocation} \end{cases} \qquad (5.2)$$

where G is shear modulus, b is atomic diameter, x and y represent the distance between the solute atom and dislocation, $\omega_b = \left(1/b\right) \cdot \left(db/dc\right)$ is the size misfit, and υ is Poisson's ratio. E_b^e and E_G^e are interaction energies with an edge dislocation resulting from the size misfit and modulus misfit, respectively. E_G^s is the interaction energy with a screw dislocation resulting from the modulus misfit. According to the linear elasticity theory, there is no interaction between a screw dislocation and the solute atom due to size misfit [26,120]. Thus, the force required to drive the dislocation away from the solute atom in the x direction is

$$f(x) = \frac{\partial(E_b + E_G)}{\partial x} = f_b(x) + f_G(x) \tag{5.3}$$

For edge dislocation,

$$f(x) \approx G_0 b_0^3 (b - b_0) \frac{xy}{(x^2 + y^2)^2} + \frac{(G - G_0)b_0^5}{4\pi^2(1 - \upsilon_0)} \cdot \frac{x}{(x^2 + y^2)^2} \tag{5.4}$$

The total force required to drive the edge dislocation away from the solute atom along the x-direction to a distance where the force becomes zero can thus be expressed as

$$f_{disl-solute} = \kappa \Delta b + \tau \Delta G \tag{5.5}$$

Since $G = \frac{E}{2(1+\upsilon)}$, Young's modulus is related to EWF expressed as $E = \alpha \cdot \varphi^6$, where $\alpha \approx 0.02(GPa)/(eV)^6$[71], and the atomic diameter (equal to the length of the Burger's vector) has a certain relation with EWF, represented as[74],

$$b = 2 \times [6.7\varphi^2 - 76.1\varphi + 349.4] \tag{5.6}$$

Thus, we may define the hardening effectiveness based on the force, $f_{disl-solute}$

$$F \approx |\kappa \Delta b + \tau \Delta G| = \left| 2\kappa(13.4\bar{\varphi} - 76.1)\Delta\varphi + \tau \frac{3\alpha\bar{\varphi}^5}{(1+\upsilon_0)}\Delta\varphi \right| \tag{5.7}$$

$$= \left| [A(13.4\bar{\varphi} - 76.1) + B\bar{\varphi}^5]\Delta\varphi \right|$$

where $\Delta\varphi$ is the difference in EWF between the solute and host, $\bar{\varphi}$ is the average EWF of solute and host atoms, G_0, b_0 and φ_0 are constants of the host material. A and B are material constants of the host.

Eq. (5.7) indicates that the solution hardening effectiveness can be related to the solute's EWF and the difference in EWF between solute and host. The larger the difference in EWF, the stronger is the solute-strengthening effectiveness. In addition, solutes with higher EWFs raise the average EWF, $\bar{\varphi}$, further benefiting the strengthening effectiveness. Based on Eq. (5.7) and information given in Table 5.1, it may explain the order of effectiveness for solutes Ni, Zn, Ga to strengthen Cu as shown in Figure 5.3. EWF difference between zinc and copper is smallest; thus zinc is the weakest to strengthen copper. Among the three solutes, nickel has the largest EWF value and the largest EWF difference to copper, rendering it the most effective solute to strengthen copper.

The above proposed model demonstrates that it is possible to use EWF as an indicative parameter to evaluate the solution hardening effectiveness.

5.4.2 Path two: effectiveness based on the energy barrier to dislocation movement

The strengthening effectiveness expressed in Eq. (5.7) may also be derived from the interatomic potential, e.g., the simplest Lennard-Jones potential,

$$\phi(r) = \varepsilon_b \left[\left(\frac{r_e}{r} \right)^{12} - 2 \left(\frac{r_e}{r} \right)^{6} \right] \qquad (5.8)$$

where ε_b is the atomic bond energy or the depth of the potential well, and r_e is the atomic spacing at equilibrium. A higher EWF corresponds to a deeper interatomic potential well and thus a stronger atomic bond, which results in stronger confinement for valence electrons and consequently smaller spacing between adjacent atoms in a crystal with a larger elastic modulus. Thus, EWF could be used to help select suitable solute elements based on this parameter (EWF or φ) without involving complicated calculation or analysis regarding the solute-dislocation interaction and the synergistic effect of the size misfit and modulus misfit on the strengthening effectiveness.

The strain energy of a dislocation may be generally expressed as

$$U = \frac{1}{2} E \varepsilon^2 \qquad (5.9)$$

where E is the elastic modulus and ε is a general term of strain associated with lattice distortion caused by the dislocation. The change in strain energy when the solute interacts with the dislocation

$$\Delta U_{disl-solute} = \frac{1}{2} (\varepsilon^2 \Delta E + 2 E \varepsilon \Delta \varepsilon) \qquad (5.10)$$

where ΔE is the difference in elastic modulus between the solute and host, and $\Delta \varepsilon \propto (\Delta r_e / r_e)$. When a dislocation is pinned by a solute atom, the decrease in strain

energy is $\Delta U_{disl-solute}$. Thus, the energy barrier to the dislocation movement would be

$$\left|\Delta U_{dislo-solute}\right| = \left|\frac{1}{2}(\varepsilon_0^2 \Delta E + 2E_0\varepsilon_0\Delta\varepsilon)\right| = \left|\frac{1}{2}(\varepsilon_0^2 \Delta E + 2E_0\varepsilon_0 \frac{\Delta r_e}{r_e})\right| \qquad (5.11)$$

According to the previous studies discussed in section 2.2.4.4 and section 2.2.4.9, $E = \alpha'\cdot\varphi^6$, $r_e = 6.7\varphi^2 - 76.1\varphi + 349.4$, we have

$$\left|\Delta U_{dislo-solute}\right| = \left|\frac{1}{2}(\varepsilon_0^2 \Delta E + 2E_0\varepsilon_0\Delta\varepsilon)\right| = \left|\frac{1}{2}\alpha'(\varepsilon_0^2 6\overline{\varphi}^5\Delta\varphi + 2\varphi_0^6\varepsilon_0 \frac{\Delta r_e}{r_e})\right|$$
$$= \left|[A'(13.4\overline{\varphi} - 76.1) + B'\overline{\varphi}^5]\Delta\varphi\right| \qquad (5.12)$$

where ε_0, E_0, φ_0 are general terms of strain associated with lattice distortion, Young's modulus and EWF of the host material, which are constants of the material, and $\overline{\varphi}$ is the average EWF of solute and host atoms. Eq. (5.12) has the same form as that of Eq. (5.7). (A, B) or (A', B') are constants which can be determined by fitting experiment data for metals. Since the atomic size and Young's modulus are intrinsically related due to the fact that both are correlated to EWF, they should not be treated separately. The contributions of these two factors to the hardening effectiveness vary with EWF. As an example, Figure 5.5(a) illustrates the relationship between EWF and the effectiveness of hardening copper by solute based on Eq. (5.12). Experimental data used for curve fitting are collected from the literature [127]. As shown, the larger the EWF difference between solute atom and host atom, the more effective is the solute for hardening, and the solute with larger EWF is more effective. The predicted solution hardening effectiveness also explains our

experimental measurements (*i.e.*, Ni is the most effective to harden Cu, followed by Ga, and Zn shows the lowest effectiveness to harden Cu; $\varphi_{Ni} = 5.15eV, \varphi_{Ga} = 4.15eV, \varphi_{Zn} = 4.33eV$), which supports the proposed model. Figure 5(b) provides another example, showing solute-hardening of Mg, to validate the proposed model. Experimental data used for curve fitting are collected from the literature [128].
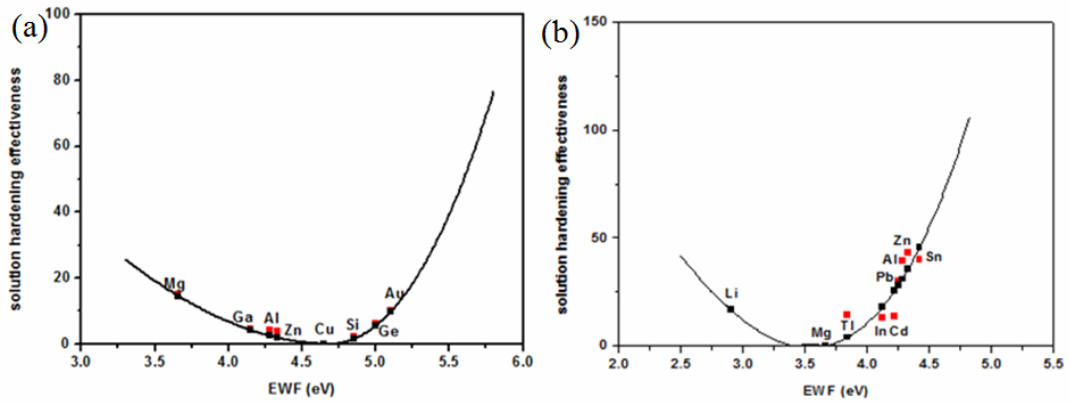
Figure 5.5 Predicted solid solution hardening effectiveness (black squares) in comparison with experimental data (red squares), (a) host atom is copper (b) host atom is magnesium. Experimental data are cited from references [127,128]

5.5 Summary

The solid solution hardening is affected by the size misfit and elastic modulus misfit. These two factors are mutually related but the classic theory is somehow ambiguous without clear clues for optimizing the balance between the two factors for maximized hardening effectiveness. In this study, the conventional mechanism is re-examined and a single-parameter model using EWF as an indicator to evaluate

the capability of solute atoms in solid solution hardening is proposed. With demonstrated relationships between EWF and elastic modulus and atomic size, this model may facilitate solute selection with a new view on the strengthening mechanism on an electronic base. The prediction from the proposed EWF model is consistent with relevant experimental observations.

Chapter 6 Correlations between EWF and properties of multi-phase alloys

Previous studies have demonstrated that EWF is intrinsically related to many mechanical properties of pure metals, such as Young's modulus, hardness, yield strength and thermal expansion coefficient [71,72,100], *etc.* These relationships can be extended to isomorphous solid solutions as discussed in Chapter 4. It has been demonstrated that EWF provides a new and effective approach for alloying element selection to achieve adjustable strength for isomorphous solid solutions [107,115]. However, realistic industrial materials generally have multi-phase microstructures. Thus, whether or not the established relationships between EWF and mechanical properties of pure metals are applicable to multi-phase alloys needs to be investigated. The research efforts in this chapter are oriented to determination of the relation between EWF and mechanical properties of multi-phase alloys and explore application of EWF for realistic material design. The work reported in this chapter has been published in Scientific Reports 6 (2016) 24366 [129] entitled "Electron work function–a promising guiding parameter for material design" by Hao Lu, Ziran Liu, Xianguo Yan, Dongyang Li, Leo Parent, and Harry Tian.

6.1 Experimental details

X70 steel (a common pipeline steel) contains only 0.066%C and very minor elements (0.5% Mn, 0.3% Cr, Si, P, S) within their solubility. This steel, in a form of nearly iron with little cementite (see a TEM image of X70 in Figure 6.1), is used as a base material for this study. X70 samples containing different amounts of Ni

addition were made using an arc melting furnace, annealed (homogenization treatment) in a tube furnace at $600°C$ in an Ar atmosphere for 3 hours followed by furnace cooling. The samples were polished using 400, 600, 800, 1200 grit SiC sand papers successively and finally polished in a solution containing diamond particles 1 μm in diameter. The polished surface was cleaned using an ultrasonic cleaner with reagent alcohol for 3 min. Right after drying, the EWF of the surface was measured using a scanning Kelvin probe (KP Technology Ltd. UK) in order to minimize the influence of contamination and oxidation on EWF measurement to obtain reproducible results. During the measurement, a surface under study was scanned by the SKP over an area of $16\mu m \times 16\mu m$ which covered 25 points for EWF measurement. At least three different regions on each sample and two samples for each alloy were analyzed for statistically reliable results. Young's modulus and hardness of the samples were measured using a micro-indenter (Fisherscope H100C Micro hardness Measurement System, Fisher Technology, Germany). A cone-shaped diamond indenter tip was used and the load was applied at a rate of 30mN/s up to 600 mN. Each sample was measured at least five times. Macro-hardness of the samples was measured using a Mitutoyo hardness tester under a load of 15 kg with a pyramidal indenter. Each hardness value is an average of 5 measurements made at randomly selected locations on each sample.
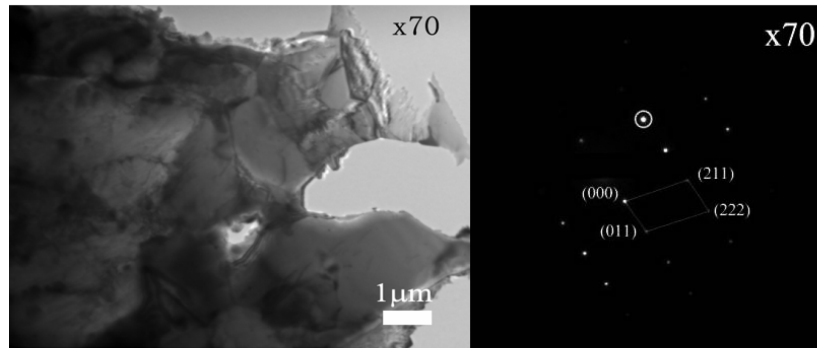
Figure 6.1 TEM image and diffraction pattern of the base alloy, X70 steel, which contains mainly ferrite with little cementite

Crystal structures of the samples were analyzed with X-Ray diffraction (Rigaku XRD Ultimate IV; Cu $k\alpha$ radiation). Surface morphological observation and local EWF analysis were carried out using a multi-mode AFM with the capability for *in situ* measuring or mapping EWF, elastic modulus and deformation simultaneously. The electron density of the samples was analyzed by ultraviolet photoelectron spectroscopy (UPS, Axis Ultra Spectrometer, Kratos Analytical). The UPS measurement was carried out in vacuum in order to prevent the influences of adsorption and contamination on the measurement. Before UPS tests were performed, sample surfaces were sputtered by argon ions in order to eliminate possible surface contamination. A multimode AFM (Bruker, US) was used to analyze local EWF, magnetic properties of phases and modulus of different phases/domains.

6.2 Simulation details

All energy calculations were carried out using the density functional theory

(DFT) implemented in the Vienna Ab initio simulation package (VASP) [130,131]with the projector-augmented wave (PAW) potential [132]. The generalized gradient approximation (GGA) with the exchange-correlation functional of Perdew, Burke and Ernzerhof(PBE) [133]was employed. K-points sampling using Monkhorst-Pack [134] with k-mesh of 21×21×21 was sufficient for structure optimization. A finer k-mesh (25×25×25) appeared to be optimal for calculating the elastic constants. The *K-mesh* of 25×25×1 was applied in supercell calculations. The elastic constants were calculated from the energy variation introduced by applying very small strains to the lattice in equilibrium. For a given strain, all internal atomic coordinates were fully relaxed while keeping the deformed lattice fixed. The elastic energy,ΔE, of a crystal can be expressed as:

$$\Delta E \approx \frac{\Delta V_0}{2} \sum_{i,j=1}^{6} C_{ij} e_i e_j \tag{6.1}$$

where ΔV_0 is the volume of a undistorted crystal unit cell, the vector $e = (e_1, e_2, e_3, e_4, e_5, e_6)$ represents the applied strain, and coefficients C_{ij} are elements in the elastic-constant matrix. ΔE and ΔV_0 were fitted with a quadratic polynomial to obtain the relevant elastic constants. Since the systems under study are cubic structures, there are only three independent elastic constants, C_{11}, C_{12} and C_{44} [135].

6.3 Results and discussion

6.3.1 Changes in EWF and mechanical properties with composition

Measured EWF, Young's modulus and hardness of samples with different concentrations of Ni are given in Figure 6.2. As shown, values of these properties increase initially with %Ni and reach maxima at 10%Ni; however, when more than 10% Ni is added, values of all the properties decrease. The changes in Young's modulus and hardness follow closely the changes in EWF. In order to ensure that the measurements reflected average mechanical properties of bulk materials, macro-hardness of the samples was also evaluated using a macro-hardness tester. Results of the measurements are given in Table 6.1. As shown, the trend of the macro-hardness with respect to %Ni is consistent with that of results obtained from micro-indentation testing.
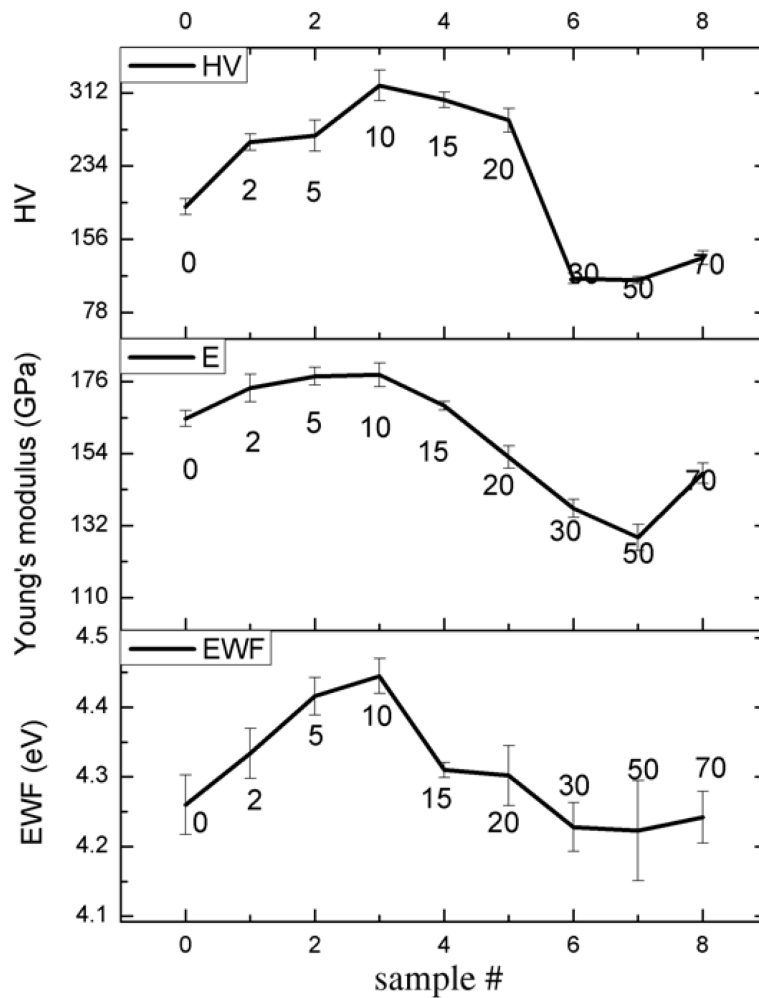
Figure 6.2 EWF, Young's modulus and hardness of X70 samples with different concentrations of Ni. The numbers around each curve represent %Ni (e.g., 15 stands for 15%Ni), x-axis gives I.D. number for the samples (e.g., sample 2 has its %Ni=5%). EWF was measured using a scanning Kelvin probe (SKP); Young's modulus and hardness were determined using a micro-indenter.

Table 6.1 Hardness of X70 samples with different concentrations of Ni. Hardness was measured using a macro-indenter and the load was 15 kg

Sample	Hardness (HV)
X70	60.8+/-1.1
X70-2Ni	65.8+/-0.8
X70-5Ni	74.3+/-0.3
X70-10Ni	74.5+/-1.1
X70-15Ni	72.9+/-3.3
X70-20Ni	72.6+/-1.2
X70-30Ni	40.0+/-0.2
X70-50Ni	44.2+/-0.8
X70-70Ni	38.4+/-3.0

The initial increase in Young's modulus with EWF as a small amount of Ni was added to X70 can be explained based on the fact that EWF reflects the stability of the electron state and the resistance to breaking of atomic bonds. A metal which has a higher EWF requires more energy to change its electron state. Adding an element with higher EWF, the modified base alloy would have an increased EWF. This consequently generates higher barriers to attempts to change its mechanical and electrochemical states, which are related to the electron state that governs the atomic bond strength. When Ni is added to X70 steel, the overall EWF increases, corresponding to a stronger bonding between adjacent Ni and Fe atoms or a larger barrier to separation of a Fe-Ni atomic pair; as a result, Young's modulus of the steel increases. As for hardness, the stronger atomic bonding also raises barriers to generation and movement of dislocations, leading to higher hardness. It should be indicated that the increase in hardness is less intrinsic, since it is also influenced by other factors. However, although hardness is a property influenced by multiple factors such as elastic modulus, slip systems, and the activation energy of

dislocations, *etc.*, the atomic bonding is a primary intrinsic factor. Or in other words, for metals having the same crystal structure, their hardness is mainly governed by the atomic bond strength and thus the elastic modulus, which is therefore correlated to EWF. The activation energies for dislocation generation and movement motion are also related to the elastic modulus and thus the electronic state or EWF. This explains why the variation in hardness with %Ni shows a trend similar to those of Young's modulus and EWF as illustrated in Figure 6.2. Clearly, the hardness is correlated to EWF.

However, when more than 10% nickel was added to X70 steel, both EWF and the mechanical strengths decreased. Such changes are different from the effect of a small amount of Ni addition on the steel and also what previous studies showed, *i.e.*, adding an element with a higher EWF can raise the overall EWF and the mechanical strength of isomorphous alloys as discussed in Chapter 4. In order to clarify the discrepancy, possible changes in structure or microstructure were examined through X-ray diffraction (XRD) analysis. Obtained XRD patterns of X70 samples with different amounts of added Ni are illustrated in Figure 6.3. As shown, below 10%Ni, samples are homogeneous without second phases present. When 15wt% Ni is added to X70, very small peaks of the $FeNi_3$ phase show up. The peaks of $FeNi_3$ become much stronger when 30 wt% Ni is added to X70. When 70 wt% Ni is added, the sample contains almost $FeNi_3$ fully, which is consistent with the Fe-Ni phase diagram (see Fig.6.3 (b)) and observations by others [136,137]. Thus, when the second phase forms in the samples, one cannot simply expect that the mechanical strength of the alloy is enhanced by alloying with an element that has a higher EWF.
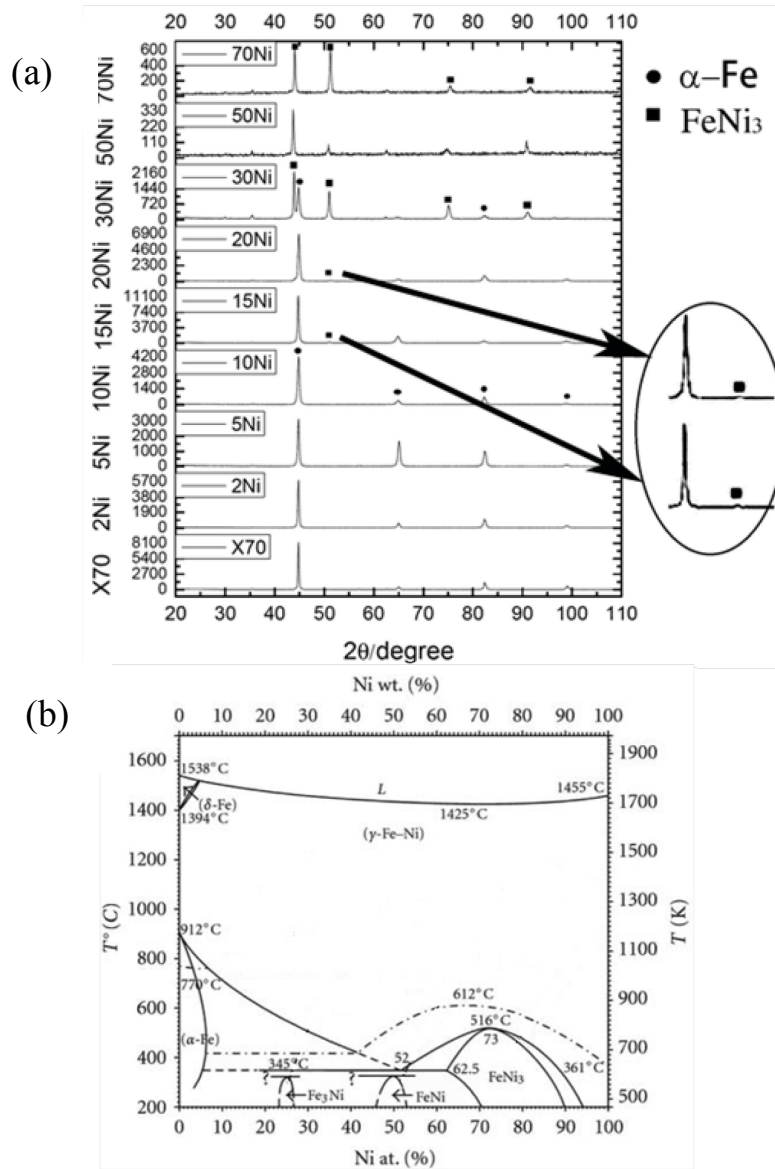
Figure 6.3 (a) XRD patterns of X70-Ni samples containing different amounts of Ni addition. When Ni concentration is lower than 10%, samples show only one phase. Once the amount of Ni is more than 10%, samples contain two different phases, ferrite and $FeNi_3$. However, X70-70Ni basically only shows peaks of $FeNi_3$. (b) A phase diagram of Fe-Ni

It should be pointed out that $FeNi$, Fe_3Ni and γ-Fe all have FCC structures and their XRD peaks are close to or overlap with those of $FeNi_3$. However, it is believed that the formed phase is $FeNi_3$ rather than either FeNi or Fe_3Ni based on the phase stability and mechanical properties. According to extensive studies [136,138], the diffusion rate of Ni in the Fe-Ni system is very low. Thus, some phases shown in the Fe-Ni phase diagram are hard to obtain or be observed experimentally. $FeNi_3$ is a stable intermetallic phase in the Fe-Ni system, while FeNi and Fe_3Ni are metastable phases according to both experimental and theoretical (enthalpy and free energy) studies [139-141]. Thus, $FeNi_3$ is a favorite phase, compared to the metastable FeNi and Fe_3Ni. The metastable phases may exist in very fine particles of Fe-Ni alloys when the cooling rate is high [142]. FeNi and Fe_3Ni are indeed observed in Fe-Ni nanopaticles but not in bulk materials fabricated in the laboratory. Besides, the bulk modulus of $FeNi_3$ is lower than that of Fe and the latter is lower than those of FeNi and Fe_3Ni [143]. We performed nano-indentation tests to evaluate hardness of the formed second phase domains in the X70-30Ni sample and confirmed that the formed phase was softer than X70 which is basically α-Fe. Based on the above analysis, we believe that the phase marked with black squares in XRD patterns is $FeNi_3$ rather than metastable FeNi or Fe_3Ni.

The phase marked with black squares in the XRD patterns should not be γ-Fe either, since the formed phase is softer than α-Fe, while γ-Fe is harder with higher EWF than α-Fe. Thus, the formed softer phase cannot be γ-Fe. In order to further confirm this conclusion, we conducted magnetic mapping for the X70-50Ni

sample with magnetic force microscopy (MFM) using a multimode atomic force microscope. Similar to α-Fe, FeNi$_3$ is a ferromagnetic phase, while γ-Fe is a paramagnetic phase [139,141]. In the magnetic map, a ferromagnetic phase shows a strip pattern while the paramagnetic γ-Fe phase does not have such pattern [68]. The samples under study were examined; no paramagnetic γ-Fe domains were observed and all obtained magnetic maps only show typical ferromagnetic features in the entire sample area under analysis. Figure 6.4(a) shows a representative magnetic map of a X70-50Ni sample with strip pattern over an area of $80 \times 80 \mu m$. No paramagnetic γ-Fe domains are presented. Figure 6.4 (b) and (c) present a closer view of the magnetic map and a corresponding EWF map, which shows the presence of sub-micron ferromagnetic domains that are softer with lower EWF than the matrix. These suggest that no detectable γ-Fe existed in the sample under examination.
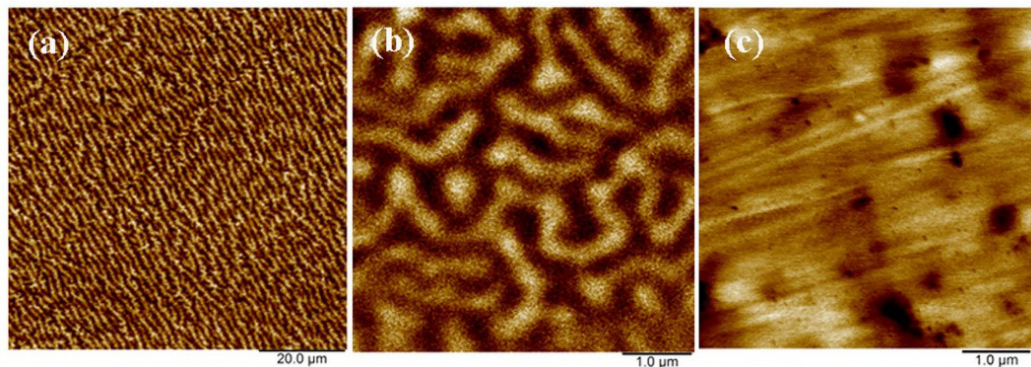
Figure 6.4 (a) a magnetic map of X70-50Ni sample with strip pattern over an area of $80 \times 80 \mu m$, (b) a close view of the magnetic map over a smaller area, and (c) a corresponding EWF map of the area shown in (b), in which the dark domains have lower EWF and are believed to be FeNi$_3$ precipitated in α-Fe matrix (the bright area of the EWF map).

Previous studies have demonstrated that EWF has sixth power relationships with Young's modulus and hardness of metals, e.g., $E = \beta \varphi^6$, where E is the Young's modulus or elastic modulus and β is a coefficient. Such relationships still
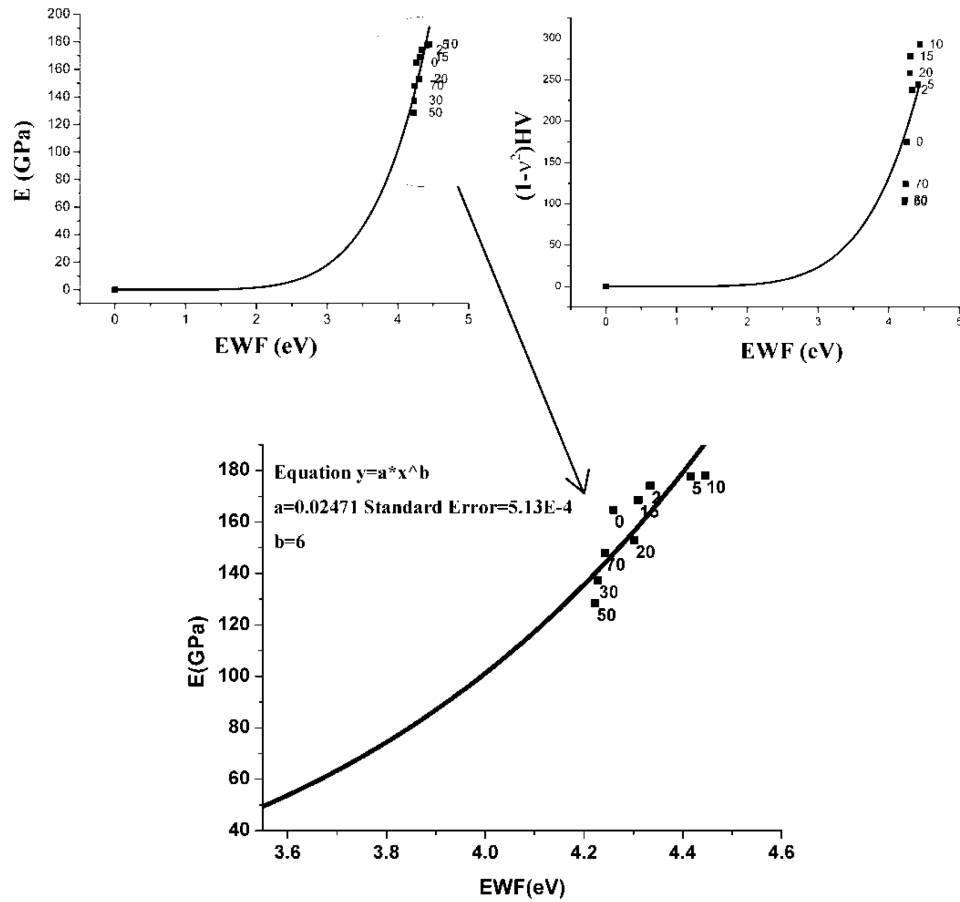
Figure 6.5 Variations in Young's modulus (E) and hardness (H) with EWF. Curves of E ~ EWF and (1-υ^2)H ~ EWF of Ni-added X70 samples were obtained by fitting experimental data points. υ is the Poisson's ratio. The curves are consistent with theoretical sixth power relationships with similar coefficients (β).

exist in the present case (See Figure 6.5), no matter whether the second phase, $FeNi_3$, exists or not. A fitted coefficient (β), *e.g.*, for $E \sim \varphi$ curve, equals 2.47×10^{-2}, which is consistent with previous theoretical analysis [71].

It appears that the overall mechanical properties are determined by the overall EWF to a certain degree. Figure 6.6 schematically illustrates two general cases to show how the individual phases with different scales may affect the overall EWF, resulting in possible influences on the overall mechanical properties of the material systems. Figure 6.6(a) shows a two-phase material in which phase 1 has a higher EWF than phase 2(softer). When EWF of the material is measured under the applied potential, electrons are pulled out basically from phase 2 with a lower EWF ($\varphi_{\textbf{Phase2}}$). Thus, the overall EWF is dominated by $\varphi_{\textbf{Phase2}}$. The overall mechanical strength is lowered by the softer phase 2, corresponding to a lower overall EWF. The situation is reversed if phase 2 becomes harder with a raised EWF. Thus, variations in the overall EWF due to changes in EWFs of individual phases may reflect corresponding variations in the overall mechanical properties of the material system.

Figure 6.6(b) illustrates another system in which finer domains of phases 1 and 2 are densely distributed. In this case, the overall EWF is dominated by the phase which has a higher EWF, depending on size and spacing between adjacent domains of the higher EWF phase. This has been demonstrated by a recent study on TiC-Ni composite coatings with two sizes of TiC particles on micron and nanometer scales[144]. Effects of the second phase's size and morphology on the interfacial coherency and thus properties of a two-phase material are also reflected by

EWF[144,145]. As observed in the study on TiC-Ni composite coatings, lower interfacial coherency (caused by large TiC particles embedded in the Ni matrix) resulted in lowered EWF or electron localization at the interface. Such lowered EWF at interfaces reflects a lower resistance of materials to mechanical and electrochemical attacks [112,146]. However, the situation is reversed when the particle size is on nano-scale with elevated interfacial coherency [144,145].
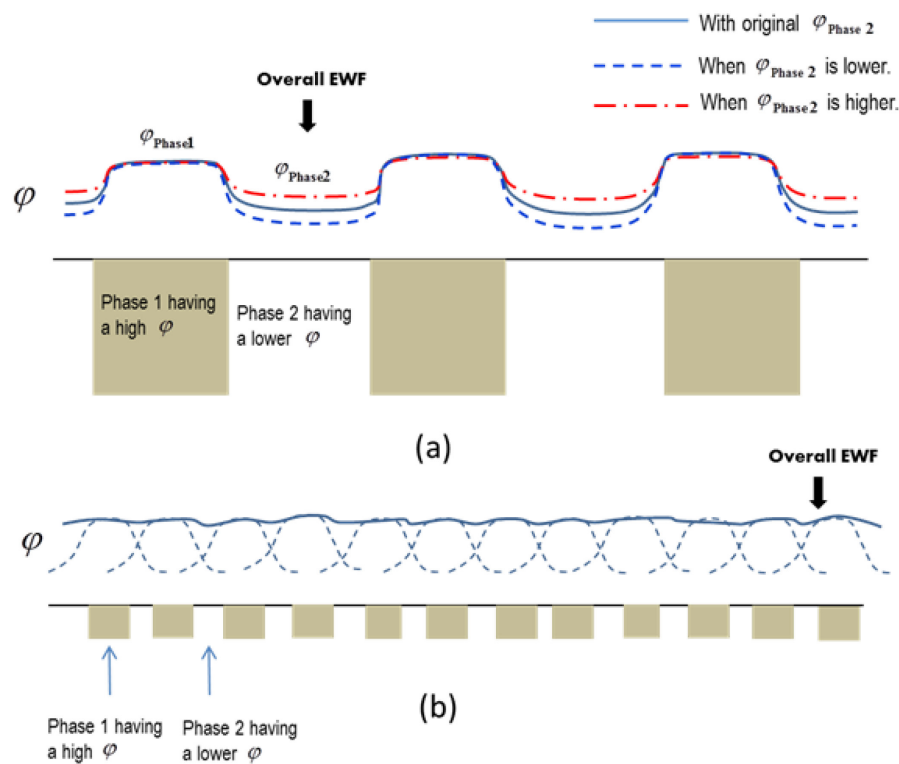
Figure 6.6 Schematic illustrations: effects of EWFs of individual phases and microstructure on overall EWF of a two-phase material. (a) The overall EWF is mainly the EWF of the phase having a lower EWF; (b) The overall EWF increases as the size of the phase with a higher EWF becomes smaller and more densely distributed.

Based on collected information from current and previous studies, it appears that the overall EWF integrates EWFs of individual microstructure constituents (phases, interfaces) and their mutual influence or synergy. Such an integrated EWF may reflect material properties to a certain degree.

6.3.2 Effect of the second phase on the properties of Ni-added X70

As shown in section 6.3.1, the formed $FeNi_3$ phase resulted in a deviation from the trend of changes in EWF with %Ni, observed for isomorphous solid solutions in which solute atoms are homogeneously dispersed in the host lattice. More detailed analysis was made to investigate influences of this second phase on the Ni-added X70 steel. A multimode atomic force microscope (AFM) with a nano-Kelvin probe was used to map variations in local EWF of samples with different concentrations of Ni. Figure 6.7 illustrates EWF distributions of X70, X70-10Ni, X70-30Niand X70-70Ni. As shown, the first two alloys show approximately homogenous EWF distributions, which is consistent with the XRD patterns in which the two alloys only have a single phase. However, in the X70-30Ni sample there are distinguishable domains with lower EWF. The EWF of darker domains is approximately 0.16 eV lower than that of brighter domains. Since the EWF of X70-70Ni is about 0.2 eV lower than that of X70-10Ni and the former is basically $FeNi_3$, it is believed that the darker domains in Figure 6.7(c) are $FeNi_3$.The brighter area is the α-Fe matrix with saturated dissolved Ni addition, whose composition should be close to X70-10Ni. TheX70-70Ni sample appeared to

be homogenous. However, a closer view (see Figure 6.8) shows that there are many nanometer-scaled $FeNi_3$ domains in the sample. Since the composition of this sample is close to that of $FeNi_3$, the nucleation rate of $FeNi_3$ could be sufficiently high, leading to the formation of many $FeNi_3$ nano-domains in the sample.
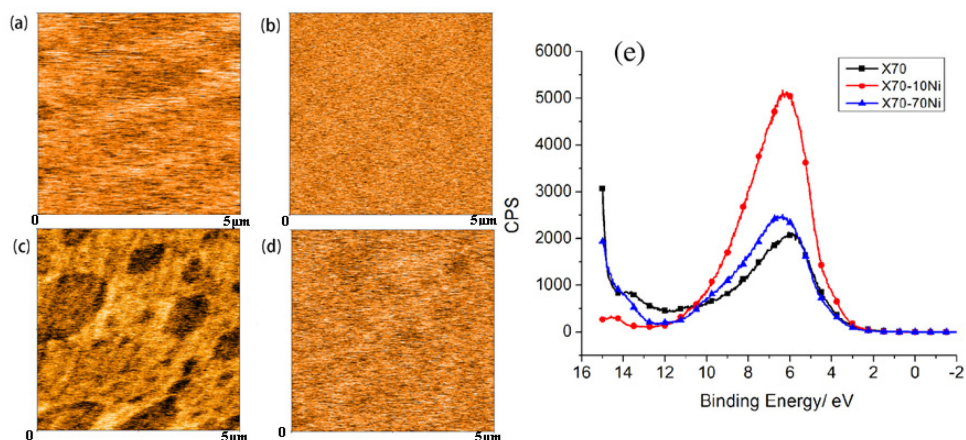
Figure 6.7 EWF maps of (a) X70, (b) X70-10Ni, (c) X70-30Ni, (d) X70-70Ni, respectively, obtained by nano-Kelvin probing. Darker regions have lower EWFs and brighter regions show higher EWFs. The EWF distribution of X70, X70-10Ni and X70-70Ni are approximately homogenous. X70-30Ni has two different groups of domains with different EWFs. (e) CPS ~ binding energy curves of X70, X70-10Ni and X70-70Ni. The area under a curve is proportional to the number of free electrons in the sample. The number of free electrons is the highest for X70-10Ni, and those of X70 and X70-70Ni are close.

The samples were also examined under a scanning electron microscope. However, due to limited resolution, the nano-scaled $FeNi_3$ domains are too small

to be clearly viewed under SEM. A SEM image of X70-70Ni is still included in Figure 6.8, from which nano-scaled domains are more or less visible.

To further analyze variations in EWF, the samples were examined using ultraviolet photoelectron spectroscopy (UPS), from which their electron band structure and valence electron density can be determined [147]. Ultraviolet light shines at the sample using a helium lamp emitting at 21.2 eV (He radiation). The photons of low energy cannot excite and emit core electrons out of the sample but have access to the valence band or can emit valence electrons. Thus, UPS can be used to analyze the valence band structure of materials and the low binding energy part of the spectrum mirrors the electron density of state in first-order approximation. The integral of the spectrum is the total number of electron states of the materials, and each state is occupied by two electrons. Since an electron is a kind of fermion, the integral of the spectrum multiplied by Fermi-Dirac distribution function equals to the number of electron states if temperature is higher than 0K [10]. Figure 6.7(e) illustrates the counts per second (CPS) ~ binding energy curves of X70, X70-10Ni and X70-70Ni. The area under a curve is proportional to the number of free electrons in the sample. As shown, the number of free electrons increases when 10%Ni is added to X70, but it decreases when more Ni is added. The number of free electrons of X70-70Ni is similar to that of X70. The decrease in EWF of X70-10Ni when more Ni is added is attributed to the formation of the intermetallic phase, $FeNi_3$. The change in electron density measured by UPS may explain the trend of variations in EWF, since EWF is proportional to the free electron density, where the number of free electrons per atom is equal to the nominal valence of the element or close to its number as expressed in Eq.(6.2) [51,148],

$$\varphi=43.46\alpha r_s^{-3/2}E_F^{-1/2} = \frac{e^3 m^{1/2} n^{1/6}}{16\pi^{5/3}3^{1/3}\hbar\varepsilon_0^{3/2}} = \frac{e^3 m^{1/2}}{16\cdot\sqrt[3]{3}\pi^{5/3}\hbar\varepsilon_\circ^{3/2}}\cdot\frac{z}{a^{1/2}}^{1/6} \tag{6.2}$$

where r_s is the electron density parameter, E_F is Fermi energy, α is an constant, n is the equilibrium valence electron density, z is the number of valence electrons, a is the lattice constant, m is the electron mass, ε_0 is the vacuum permittivity, $\hbar$ is Planck constant, and e is the elementary charge.

When Ni is added to Fe without forming a second phase, it brings more free electrons to the system and consequently raises the free electron density, leading to a higher overall EWF. As a result, the interaction between electrons and nuclei is enhanced, rendering the material stronger. When too much Ni is added with the formation of the intermetallic phase, $FeNi_3$, previous free electrons may not all serve as valence electrons. It is known that electrical conductivities of intermetallic compounds can be much lower than those of the corresponding individual elements and some of them may behave like semiconductors [149,150]. The decrease in the free electron density could be ascribed to possible change from the metallic bond to one(s) with less metallic characteristics or a mixture of metallic and covalent/ionic bonds. No matter what is the bond type or whether atoms are bonded by sharing electrons or by electrostatic interactions, if electrons are easier to be taken out from a solid, the stability of its mechanical state is lower, corresponding to weaker atomic bonds.

Local EWF, modulus and deformation of a X70-30Ni sample were mapped simultaneously using the multi-mode AFM in order to evaluate local properties of the sample consisting of $FeNi_3$ phase domains and the matrix. As illustrated in

Figure 6.8 (a)-(c), X70-30Ni shows two different regions with different EWFs. The dark domain having a lower EWF in Figure 6.8(a) is softer than the matrix, evidenced by its lower elastic moduli and larger deformation (Figure 6.8 (b) and (c)).
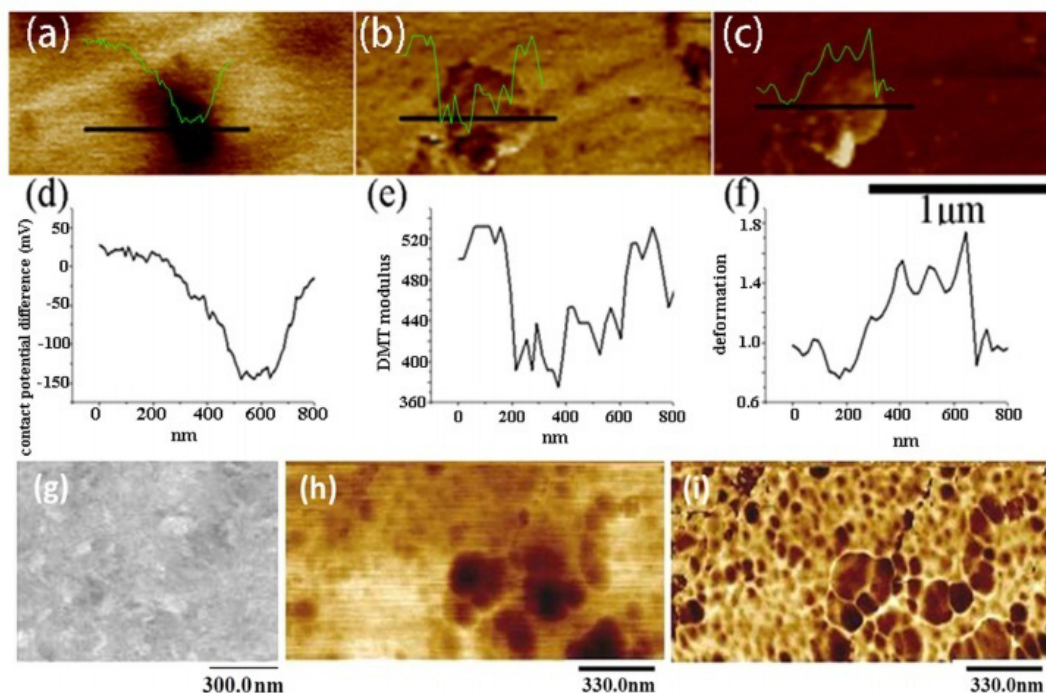
Figure 6.8 (a)-(c) show in situ EWF, elastic modulus and deformation maps of X70-30Ni with inserted line property profiles, obtained using a multi-mode AFM. In the EWF map (a), the darker domain (FeNi$_3$) has a lower EWF and brighter regions show higher EWFs. As demonstrated by the elastic modulus (b) and deformation (c) maps, the darker domain is softer than the brighter regions. (g) A SEM image of X70-70Ni, (h) a EWF map and (i) corresponding elastic modulus map of the X70-70Ni sample.

In order to support or further confirm the experimental observations, mechanical properties of α-Fe, Ni and $FeNi_3$ were calculated using the first-principles method. α-Fe has a BCC structure and the other two have FCC structures. $FeNi_3$ is an ordered phase with Fe atoms occupying the corner positions and Ni atoms located in face centers [141]. The calculated elastic constants are consistent with the experimentally measured values [141], both of which are given in Table 6.2. In Table 6.2, bulk modulus B of polycrystalline samples was also calculated from the elastic constants.

$$\mathrm{B} = (C_{11} + 2C_{12}) \Big/ 3 \qquad\qquad (6.3)$$

Unlike the bulk modulus, Young's modulus and shear modulus are more crystallographic orientation dependent. Thus, they are not calculated here for comparison purpose in order to prevent misleading information. Experimentally measured bulk modulus is given in Table 6.2 as well, which is in good agreement with the calculated one. As shown, Ni is more stiff than both α-Fe and $FeNi_3$. α-Fe has medium bulk modulus, higher than that of $FeNi_3$. This is consistent with the order of their EWFs. When Ni with a higher EWF is added to X70 steel, the overall EWF increases. However, the situation is reversed when $FeNi_3$ forms, which exhibits a lower EWF. The correlation between EWF and mechanical properties, including Young's modulus, hardness and calculated bulk modulus and elastic constants, has been well demonstrated by this Fe-Ni alloy system.

Table 6.2 Elastic constants and elastic moduli of Fe, Ni and FeNi3 from first-principles simulation and experiments; the experimental data are cited from [141]

	Fe(BCC)		Ni(FCC)		$FeNi_3$(FCC)	
	Exp.	Cal.	Exp.	Cal.	Exp.	Cal.
C_{11}	242.0	268.1	246.5	268.7	230.4	237.2
C_{12}	146.5	144.2	147.3	150.9	144.4	136.9
C_{44}	112.0	83.4	124.7	129.9	119.2	114.7
B (GPa)	178.3	185.5	180.4	190.2	173.0	174.0

In order to understand why $FeNi_3$ has a lower EWF corresponding to lowered free electron density, variations in electron localization function and electron density across a α-Fe/$FeNi_3$ interface were calculated using first-principles method. Such variations help view the difference in the degree of electron localization between α-Fe and $FeNi_3$ phase and further help understand the strengths of Fe-Fe bond and Fe-Ni bond in the $FeNi_3$ phase. However, due to different crystal structures and a large difference in lattice constant between BCC-Fe and FCC-$FeNi_3$ as well as lack of relevant information on Fe/$FeNi_3$ interfaces, it is difficult to construct an interface between these two phases, which can be used to perform convergent calculations. Thus, we study the interface between FCC-Fe and FCC-$FeNi_3$ (see Figure 6.9) with attention to variations in electron localization and density. Although the obtained information may not precisely reflect the interfacial situation, one may still see how the degree of electron localization changes when Fe and $FeNi_3$ are adjacent to each other. From the calculation, one may see that

electrons are more localized in Fe than FeNi$_3$ and the former has its electron density larger than that of FeNi$_3$. The calculations demonstrate that Fe has its electron localization function (ELF) and electron density higher than those of FeNi$_3$ phase. The calculation indicates that the Fe-Fe bond is stronger than that of Fe-Ni bonds in the intermetallic phase, FeNi$_3$.
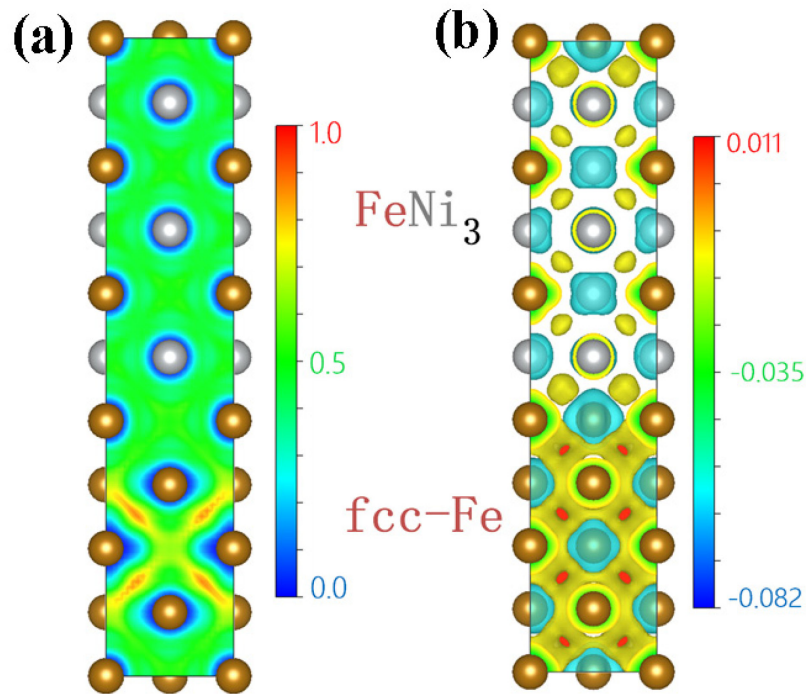
Figure 6.9 (a) Electron localization function (ELF) and (b) electron-density difference of Fe & FeNi$_3$ supercell

As shown in Figure 6.9(a), ELF in Fe region is higher than that in FeNi$_3$ region, indicating that the electrons in Fe are more localized or more tightly confined, corresponding to stronger Fe-Fe bonds in contrast with those in FeNi$_3$ phase. This explains why pure Fe has higher Young's modulus and EWF than FeNi$_3$ and why

the modulus and EWF decrease when the intermetallic phase $FeNi_3$ is formed as more than 10% Ni is added to X70.

We also calculated the electron-density difference, which is defined as the difference in the electron density between a $Fe/FeNi_3$ supercell and isolated Fe or $FeNi_3$ supercell. This parameter reflects the electron density of the system and related bond strength. As illustrated in Figure 6.9(b), the electron density of Fe supercell is higher than that of $FeNi_3$ supercell, which is consistent with the calculated electron localization function shown in Figure 6.9(a) and experimentally measured electron density from UPS analysis, EWF and elastic modulus illustrated in Figure 6.2 and Figure 6.7(e), respectively.

6.4 Summary

Correlations between EWF and mechanical properties were investigated using Ni-added X70 steel as a sample material in this study. It demonstrated that adding Ni having a higher EWF brought more "free" or valence electrons to the steel, increasing the overall EWF of the material. Young's modulus and hardness increased correspondingly, which was consistent to the results of the studies in Chapter 4. However, the free electron density and EWF decreased as %Ni was continuously increased with the formation of an intermetallic phase, $FeNi_3$. This softer phase resulted in lowered EWF and corresponding deterioration in the overall mechanical strength.

The changes in Young's modulus and hardness show trends similar to that of change in EWF with respect to %Ni no matter whether or not the second phase

(FeNi$_3$) is present. The similar trends suggest that the overall mechanical behavior is correlated with the overall EWF to a certain degree, although the former is microstructure dependent.

Chapter 7 Potential applications of EWF in materials characterization

Chapter 3 to Chapter 6 report the studies of relationships between EWF and mechanical properties of metallic materials, including pure metals, binary solid solutions or single phase alloys, and multi-phase alloys. It demonstrates that there is a clear correlation between EWF and mechanical properties of the alloys with respect to the composition. These studies demonstrate that EWF is a promising parameter which may provide supplementary clues for element selection and materials tailoring on a feasible electronic base. This promising parameter could provide alternative or complementary approaches or methodologies for materials design.

Materials characterization is an important research area in materials science, which can help to evaluate the properties of the designed materials. As discussed in Chapter 2, EWF is related to many properties of materials and EWF has been tried to be used in determining yield strength, onset of wear, corrosion resistance, *etc*. This chapter reports two studies of EWF applications in materials characterization, (1) evaluating fracture toughness of hard metallic materials and (2) analyzing interfacial bonding strength.

7.1 Potential application of EWF in analyzing fracture toughness of materials

Fracture toughness is one of the important mechanical properties of materials,

which is a measure of materials' resistance to fracture. This property is crucial to materials which are required to have high reliability such as those used for components in aircrafts and space vehicles. Materials with higher fracture toughness are more reliable than those with low toughness. The fracture toughness of a material is usually evaluated using the stress intensity factor, K. When the stress intensity factor exceeds a critical value, K_c, fracture occurs [151]. There are several standard methods for measuring the fracture toughness of bulk materials such as the impact and three-point bending methods [22]. However, the above-mentioned methods are not feasible for evaluating the fracture toughness of protective coatings, which is crucial to their performance [152,153]. Many protective coatings, *e.g.*, wear-resistant ones, are generally hard and less tough. The indentation method can be used to evaluate fracture toughness of ceramic coatings by examining the configuration of generated cracks around the indent [154]. However, this method does not work for hard metallic coatings, *e.g.*, those made of white irons or tool steels, since the coatings are hard but not as brittle as ceramic materials so that no cracking may occur around the indent. Thus, methods that can be used to evaluate the fracture toughness of protective coatings or films are highly desired.

It has been demonstrated that EWF is related to materials strength and intrinsic ductility as discussed in section 2.2.4.5 and section 2.2.4.7, and EWF is also sensitive to surface morphology and cracks [155]. Thus, it is expected that EWF could be used to reflect and characterize fracture toughness of materials.

When micro-cracks are generated in a hard and less tough material by impact, *e.g.*, repeated hammering, structural integrity of the material deteriorates. This may result in a decrease in the electron density and thus lowered EWF. Young's modulus

of the material is also lowered due to loss of corresponding mechanical integrity or an increase of broken atomic bonds, which is proportional to the crack density [156,157]. A model is proposed to estimate the stability of cracks and fracture toughness of materials based on variations in Young's modulus [158]. Young's modulus is influenced by cracks, since the local effective stiffness may considerably decrease in the vicinity of a crack. Thus, both the fracture toughness and Young's modulus of a material decrease as the crack density increases. However, precisely measuring changes in Young's modulus of a coating on a substrate is challenging [159], although many studies on measuring surface Young's modulus using indentation techniques are reported in the literature [160,161]. Allowing for the fact that EWF can easily be measured using a Kelvin probe on macro/micro-scales and using the multi-mode AFM on nano-scale, EWF could be an alternative indicator for evaluating toughness for coatings and bulks as well.

In this study, using high-Cr cast irons as a sample material, the promise of evaluating fracture toughness based on EWF is discussed. Conventional impact tests and Young's modulus analysis were also carried out in order to verify the EWF analysis. This study has been published in Journal of Materials Science and Technology (2017) entitled "Potential application of electron work function in analyzing fracture toughness of materials" by Hao Lu, Chenxin Ouyang, Xianguo Yan, Jian Wang, Guomin Hua, Reinaldo Chung, and Dongyang Li.

7.1.1 Experimental details

Six high-Cr cast irons containing 40 wt% Cr and carbon concentrations in the range from 1 to 6 wt% were selected, which are denoted as samples from 40-1 to

40-6. SEM images of the alloys are illustrated in Figure 7.1. It can be seen that samples 40-1 and 40-2 are in hypoeutectic states, 40-4, 40-5 and 40-6 are in hypereutectic states; and sample 40-3 is in a slightly hypereutectic state. The samples were repeated hammered for 2 min using a roto-hammer (Robert Bosch Tool Corporation, USA) at a frequency of 50 Hz. The head of the punching hammer, made of tool steel, had a semi-spherical shape of 5 mm in diameter. The impact energy of this punching machine was 2.207 N m. The process was well controlled in order to have the entire sample surface hammered homogeneously. Due to the low impact energy and short hammering process, little temperature rise at the sample surface was detected, so that oxidation at the sample surface was not a concern.
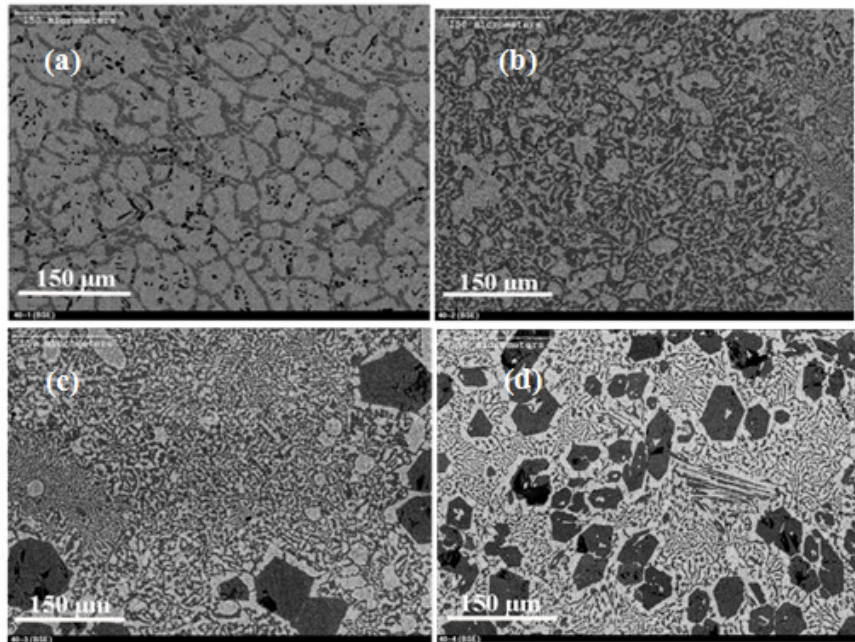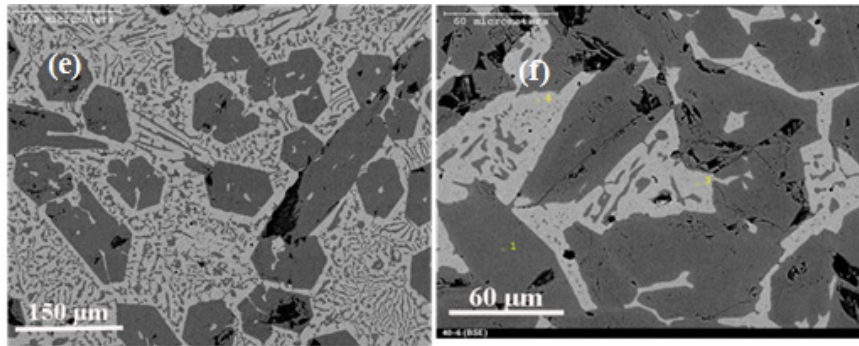
Figure 7.1 Microstructures of alloys (a)40-1, (b)40-2, (c)40-3, (d)40-4, (e)40-5 and (f)40-6

Young's modulus and EWF of the samples before and after the hammering were measured. Before EWF measurement, the samples were cleaned using an ultrasonic cleaner with reagent alcohol for 3 min to minimize the influence of contamination. EWFs of the samples were measured using a scanning Kelvin probe (KT Technology, UK) with a tip of 1 mm in tip radius. EWFs of the samples were further analyzed using a Bruker Multimode-8 AFM with the capability for local EWF mapping. Contact potential difference between the AFM probe (CoCr coated Si AFM probe with its nominal tip radius equal to 35 nm) and the sample was measured, which was then converted to EWF. Young's modulus of the samples was determined using a resonant frequency and damping analyser (RFDA) made by Integrated Material Control Engineering (IMCE, Belgium). During the measurement, an impulse was used to vibrate the sample and flexural vibration modes were analyzed, based on which Young's modulus was determined. Details about the Young's modulus measurement can be found in ASTM E 1876 "Standard Test Method for Dynamic Young's Modulus, Shear Modulus, and Poisson's Ratio by Impulse Excitation of Vibration". The specimen for Young's modulus

measurement had dimensions of 50 mm × 10 mm × 5 mm. Changes in sample dimensions by the repeated hammering process were very small and negligible.

Fracture toughness of the samples was directly evaluated using conventional method based on ASTM E 399 standard (three-point bending test).

7.1.2 Experimental Results

Fracture toughness and changes in both EWF and Young's modulus caused by hammering are illustrated in Figure 7.2 and measured experimental values are listed in Table 7.1. As observed, the hypereutectic alloys 40-5 and 40-6 showed lower toughness, while hypoeutectic and eutectic samples with lower %C were tougher. The repeated hammering decreased both Young's modulus and EWF for all samples. The samples with lower fracture toughness showed larger decreases in Young's modulus and EWF.
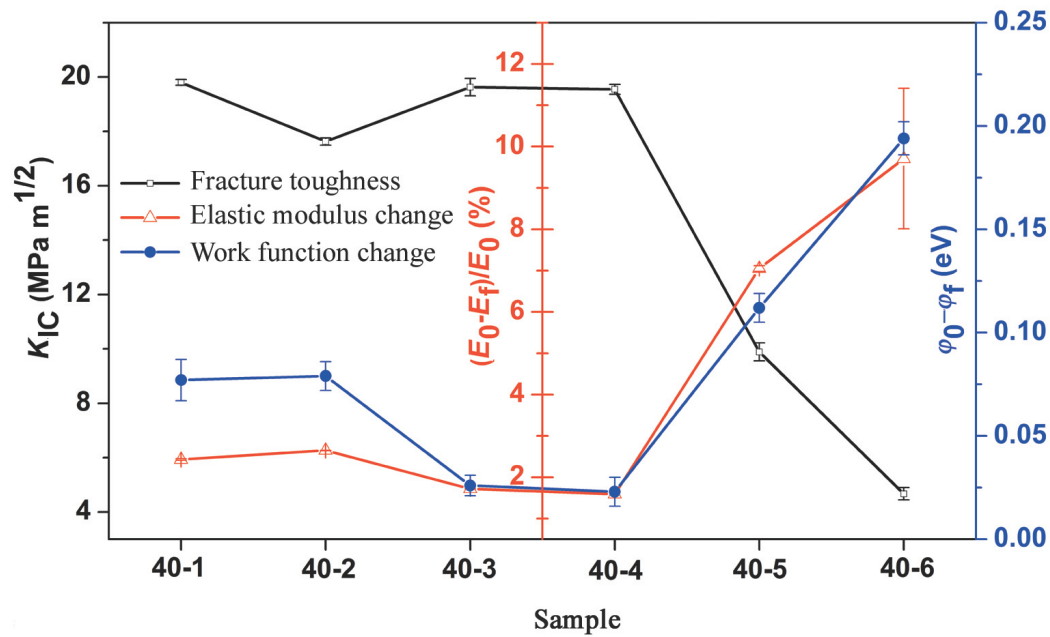
Figure 7.2 Samples with lower fracture toughness showed larger decreases in Young's modulus and EWF change caused by repeated hammering (φ_0: EWF before hammering; φ_f: EWF after hammering; E_0: Young's modulus before hammering ; E_f: Young's modulus after hammering ; K_{IC}: fracture toughness).

The changes in EWF ($\Delta\varphi$) caused by repeated hammering were measured. As shown in Table 7.1, the average changes in EWF measured respectively using AFM and Kelvin probe show similar trends. Roughness values of the samples before and after the repeated hammering were determined using a confocal microscope. As illustrated in Table 7.2, the repeated hammering did not change the roughness of the samples much, suggesting that the minor changes in roughness should not be responsible for the variations in EWF caused by hammering. Sample 40-6 provides a good example. As shown, hammering resulted in little change in roughness of sample 40-6 (Table 7.2), but this sample showed the largest variation in EWF as

illustrated in Figure 7.2.

Table 7.1 Fracture toughness of the samples, which was tested based on ASTM E 399 standard; Changes in Young's modulus and EWF of the samples caused by repeated hammering. Young's modulus was measured using an impulse excitation technique, and EWF was measured using a multimode AFM and also a macro-Kelvin probe.

sample	Fracture toughness (MPa $m^{1/2}$)	Changes in relative Young's modulus, $\frac{E_0 - E_f}{E_0}$ (%)	Changes in work function, $\varphi_0 - \varphi_f$, (eV)	
			measured by AFM	measured by Kelvin probe
40-1	19.80	2.43	0.077	0.053
40-2	17.63	2.65	0.079	0.080
40-3	19.63	1.72	0.026	0.034
40-4	19.55	1.59	0.023	0.037
40-5	9.89	7.05	0.112	0.163
40-6	4.67	9.71	0.194	0.250

As shown in Figure 7.2, there is a good correlation between $\Delta\varphi$ and fracture toughness. Samples with lower fracture toughness reveal larger decreases in EWF caused by the repeated hammering. Figure 7.3 presents a fitting curve of fracture toughness versus $\Delta\varphi$, showing a linear relationship between the fracture toughness and $\Delta\varphi$ for the high-Cr cast irons under the present experimental conditions.

Table 7.2 Roughness values of samples before and after repeated hammering

Sample	Before repeated hammering (nm)	After repeated hammering (nm)
40-1	17.8	19.6
40-2	11.8	21.2
40-3	10.2	12.2
40-4	20.2	24.9
40-5	17.8	25.2
40-6	13.3	13.8
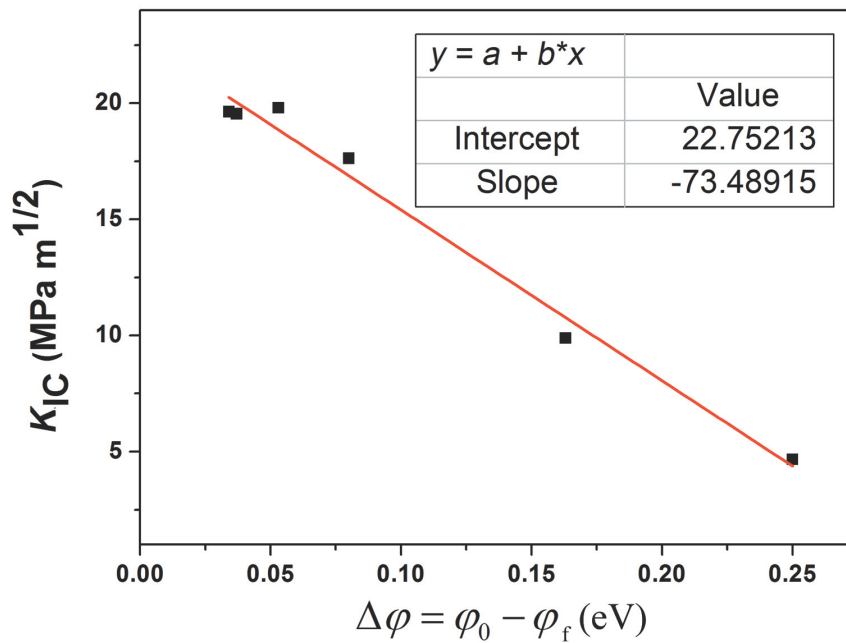
Figure 7.3 Data fitting curve demonstrating the relationship between fracture toughness of high-Cr cast irons and changes in their EWF caused by hammering.

7.1.3 Discussion

The decrease in Young's modulus is attributed to the fact that Young's modulus of a sample is related to the crack density in the sample [156-158]. More cracks with an

increase in the number of broken atomic bonds lead to larger losses of the structural integrity, resulting in a larger decrease in Young's modulus as expressed as [156]:

$$\frac{E_0 - E}{E_0} = fN_v \qquad (7.1)$$

where E and E_0 represent moduli of samples with and without cracks, respectively; N_v is the crack density and f is the micro-crack geometry factor. For samples with smaller fracture toughness, cracks were generated easily by hammering. This can be seen from microstructure examination. As illustrated in Figure 7.4(a), in samples 40-3 and 40-4 having the highest fracture toughness and smallest decrease in elastic modulus caused by hammering, no surface cracks were observed either on the surface or inside the samples. However, for low-toughness samples 40-5 and 40-6, many cracks were observed, corresponding to larger decreases in apparent elastic modulus.

The metallic bond strength is dependent on the valence electron density, which is directly related to EWF and thus connected to the elastic modulus. Fracture produces broken atomic bonds and the resultant looser structure lowers the electron density. As a result, the decrease in modulus can be reflected by the corresponding change in EWF as Figure 7.2 illustrates. Such a change in EWF provides an opportunity to evaluate the resistance to local cracking and thus the local toughness as well as global one. In other words, this allows the evaluation of toughness of coatings/thin films and local resistance to fracture, which is difficult to achieve using conventional techniques for fracture toughness measurement.
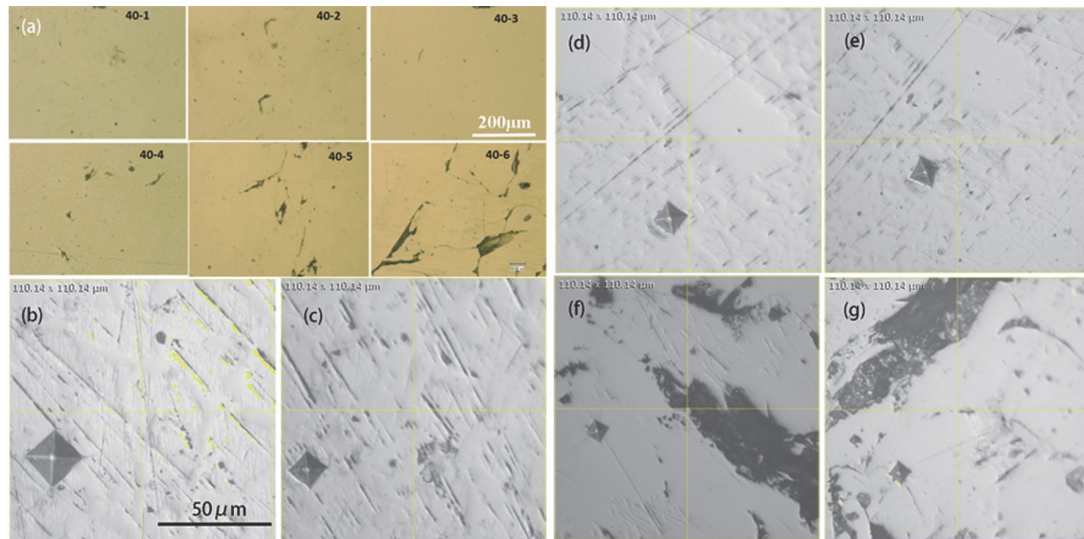
Figure 7.4 (a) Optical microscope images of samples with different carbon concentrations after hammering; both crack density and crack length increase as the carbon concentration increases; (b), (d) and (f) present optical microscope images of 40-1, 40-3 and 40-6 before hammering; (c), (e) and (g) present OM images of 40-1, 40-3 and 40-6 in same regions as those shown in (b), (d) and (f) after hammering.

As mentioned earlier, the decrease in EWF associated with micro-cracking may be viewed as a result of the decrease in the electron density. A higher electron density corresponds to a higher EWF [51]. Thus, when micro-cracking occurs in a metallic material, its overall EWF decreases.

Figure 7.5 illustrates a simple lattice model of a material with cracks. Micro-cracks are considered as clusters of vacancies, which reduce the valance electron density and thus EWF, since the latter is proportional to the sixth power of electron density expressed as [51,148]:

141

$$\varphi = \frac{e^3 m^{1/2} n^{1/6}}{16 \cdot \sqrt[3]{3} \pi^{5/3} \hbar \varepsilon_\circ^{3/2}} \tag{7.2}$$

$$\varphi_{\text{cracked}} = \frac{e^3 m^{1/2} n_{cracked}^{1/6}}{16 \cdot \sqrt[3]{3} \pi^{5/3} \hbar \varepsilon_\circ^{3/2}} = \frac{e^3 m^{1/2}}{16 \cdot \sqrt[3]{3} \pi^{5/3} \hbar \varepsilon_\circ^{3/2}} \cdot \frac{(z \cdot p)^{1/6}}{a^{1/2}} = p^{1/6} \cdot \varphi \tag{7.3}$$

where φ and φ_{crack} are EWFs of material without and with cracks, respectively; n is the equilibrium valence electron density, z is the number of valence electrons per atom, a is the lattice constant, m is the electron mass, ε_0 is the vacuum permittivity, $\hbar$ is Planck constant, e is the elementary charge, and p is the lattice site occupation probability which is between 0 and 1. As expressed by Eq. (7.3), the decrease in EWF of a material when micro-cracks are present is related to the lattice site occupancy probability. When cracks are generated by hammering, the increase in broken atomic bonds with more unoccupied lattice sites lowers the EWF.
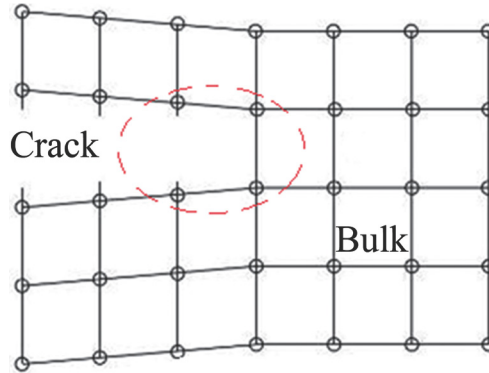
Figure 7.5 A micro-crack can be treated as a cluster of vacancies with broken bonds, where the electron density decreases.

For brittle materials, crack density or the volume fraction of cracks can be

determined by small-angle neutron scattering or analyzed based on their effects on bulk properties, such as elastic modulus and thermal diffusivity [162]. The density of cracks (Nd^3, N is the number of cracks per unit volume, d is a characteristic linear crack dimension) in brittle materials is usually between 25%-50%, dependent on the material type and how cracks are generated, *e.g.,* by thermal shocking and indentation [157,163]. This range of crack density corresponds to p=0.5-0.75, based on which one may estimate the $\varphi_{cracked}/\varphi$ ratio. According to Eqs. (7.2) and (7.3), $\varphi_{cracked}/\varphi = (0.5 \sim 0.75)^{1/6} = 0.89 \sim 0.95$, corresponding to changes in EWF in the range of 0.23-0.51 eV for materials such as ferrous alloys with their φ in the range of 4.5 eV. Since the density of cracks in cast irons, whose toughness is between those of ductile alloys and brittle ceramics, induced by hammering may not be very high as optical images (Figure 7.4) illustrates, one may assume that the change in EWF caused by hammering may not be larger than 0.23 eV. For the alloys under present study, only the most brittle one, 40-6, had its change in EWF caused by hammering reached this level.

For ductile materials, repeated hammering may only generate plastic deformation without formation of microcracks. Thus, it is not unreasonable to assume that the site occupancy probability of plastically deformed ductile samples is between those of crystalline and amorphous solids. Amorphous materials have random atomic arrangement with their packing density in the range of 0.64-0.7 [164], in comparison with 0.74 of the densest packing crystalline structures. Thus, the site occupancy probability of hammered samples with plastic deformation should be between 0.64/0.74=0.86 and 0.7/0.74=0.95. According to Eq. (7.3), we have

$$\varphi_{deformed} \Big/ \varphi = p^{1/6} = (0.86 - 0.95)^{1/6} = 0.975\text{-}0.991.$$ Since $\varphi_{Fe} \approx \varphi_{Cr} = 4.5\,\text{eV}$ [61], EWF of cast irons before hammering is around 4.5 eV and repeated hammering may change it by $4.5\,\text{eV} \times [1 - (0.975 - 0.991)] = 41 - 113\,\text{meV}$. The average change in EWF is around 70-80 meV, which is smaller than changes in EWF of brittle samples 40-5 and 40-6 but similar to those of ductile samples 40-1 and 40-2 as shown in Figure 7.2.

For better understanding, hammering-induced changes in local EWF of the samples with different carbon concentrations were also analyzed using a multimode AFM with the capability for EWF mapping. Using sample 40-3 as an example (Figure 7.6), it was observed that hammering resulted in a decrease in EWF about 25 meV in the deformed matrix while cracking in carbide led to a larger decrease in EWF in the range of 90 meV. Studies have demonstrated that cracks and defects can decrease the EWF of materials[155,165]. The larger decrease in EWF at cracks explains why the brittle samples 40-5 and 40-6 show markedly larger decreases in EWF caused by hammering.
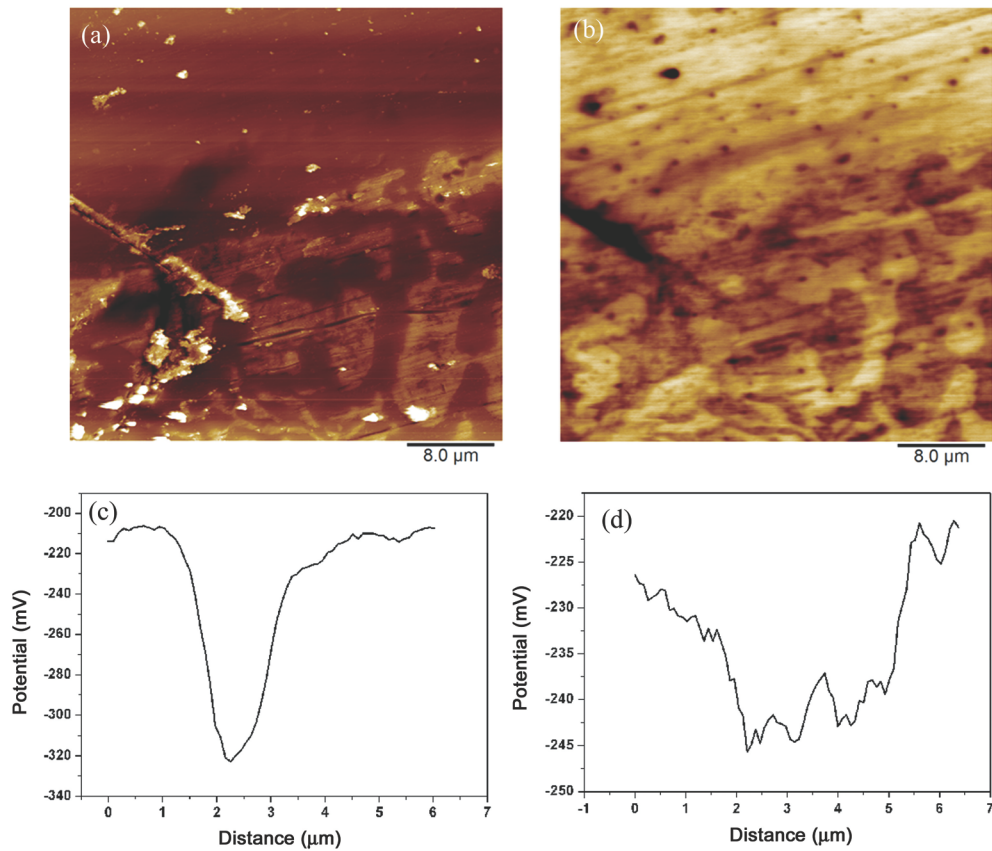
Figure 7.6 (a) a selected view of sample 40-3 (morphology) with a crack initiated at a carbide caused by repeated hammering, (b) a corresponding EWF map, in which dark regions have lower EWFs and bright regions have higher EWFs, (c) a line profile of EWF in a cracked region of a carbide in 40-3, (d) a line profile of EWF in a cracked region of the matrix in 40-3.

7.1.4 Remarking comments

Techniques are available to evaluate fracture toughness of bulk materials, but it is challenging to evaluate fracture toughness of protective coatings. In this work, an approach of using EWF as an indicator in evaluating fracture toughness of hard

metallic materials is demonstrated. It is demonstrated that the fracture toughness of the sample materials can be reflected by corresponding changes in EWF caused by repeated hammering. This study shows that EWF is an indicative parameter for analyzing fracture toughness of hard and less tough materials, especially promising for analyzing fracture toughness of hard protective coatings or thin films, which cannot be evaluated using conventional techniques.

The sample materials used in this study are, however, bulk cast irons rather than coatings. The main reason is that if directly using coatings for the present study, their fracture toughness cannot be measured using conventional methods. Thus, we would not have any reference for comparison purpose in order to verify results obtained from the EWF measurement.

It may also need to be mentioned that the thickness of protective coatings usually ranges from several dozen micrometers to the millimeter scale or even larger, which is greater than the analysis scale of EWF measurements. Thus, it is expected that the variations in EWF of layers induced by repeated hammering mainly reflect the properties of the coatings without much influence from the substrate. If the proposed method works for bulk materials, it should be applicable to coatings as well.

It should be noted that surface roughness affects the EWF. However, this influence could be minimized by adjusting hammer head's geometry and spacing between adjacent hammering points (or locations) as well as controlling hammering force and velocity, which can make it possible to reduce the change in surface roughness or to have roughness values of hammered surfaces similar. These are,

however, related to the hammering condition, which can be further studied for optimal testing conditions. In the present study, the repeated hammering did not result in significant changes in roughness of the high-Cr cast irons.

7.2 Potential application of EWF in analyzing interfacial bonding strength

Interfacial bonding plays a crucial role in determining properties and service life of coatings and welded joints. The quality of welding can be evaluated by tensile tests. However, such tests are not suitable in some cases, such as irregular shaped joints or joints with very large or small sizes. The bond strength in the small joints, such as thin films, is the average stress at the interface when fracture occurs, and is influenced by the specimen geometry and preparation. It is difficult to evaluate the bond strength between the substrate and the thin film. Thus, it is desired to develop a feasible method which can be used to evaluate the bond strength of the interfaces in various types of specimen. In this study, a novel method to characterize interfacial bonding based on interfacial EWF gradient is proposed. The interfacial EWF gradient can be analyzed by Kelvin probe force microscopy equipped on an atomic force microscope.

7.2.1 Experimental details

Pure copper and low carbon steel (0.06 wt% C 3 wt% Cr) were chosen as sample materials. Surfaces of copper and steel were polished using 400, 600, 800 and 1200 grit sand papers successively to get a mirror finish. Two polished surfaces

were clamped together by a clip to form an interface between the surfaces. In order to form an interfacial bond and avoid the influence of oxidation on the bond, the specimens were annealed in a tube furnace protected by argon gas. The annealing temperature was $700°C$ and the annealing times were 2 h, 4 h, 16 h, respectively, to get interfacial bonds with different strengths. The annealed sample surfaces were polished in cross-section using 400, 600, 800 and 1200 grit sand papers successively to get a mirror finish. The polished samples were cleaned using an ultrasonic cleaner with reagent alcohol for 3min.

Microstructure and composition of the interfaces were analyzed by scanning electron microscope (Tescan Vega 3 SEM, Czech Republic, with EDX detector provided by Oxford Instrument) to confirm that the interfacial bonds were formed in the interface region and no gaps or contamination and oxidation exist.

Micro-indentation was performed in the interfacial regions using a micro-indenter (Fisherscope H100C micro hardness measurement system, Fisher Technology, Germany) to determine the interfacial strength. A cone-shaped diamond indenter tip was used and the load was 1000 mN and applied for 60 s. The indentation position was carefully chosen to make one of the diagonals of the indenter along the interface using an optical microscope. Since the materials used to form the interfaces are the same, hardness of the materials have no effect on the indentation depths and the depths are only influenced by the interface strength. Plastic deformation depths were recorded to determine the interfacial strength.

EWFs in the interfacial regions were mapped by Kelvin probe force microscopy (KPFM, equipped on atomic force microscope (AFM), Multimode 8, Bruker, US). Measurements were performed right after the samples were polished to

avoid influence of contamination and oxidation. Bruker magnetic probes (MESP) with hard cobalt-chromium coating were used for EWF mappings in the interfacial regions.

7.2.2 Results and discussion

7.2.2.1 Microstructure

Morphologies of interfaces with different annealing durations were observed under SEM. As illustrated in Figure 7.7, no gaps are observed in the interface regions between copper and steel, which indicates that relatively good interfacial bonds are formed. Contamination and oxidation are not observed in the interface region. Figure 7.8 illustrates iron element distributions in interfacial regions with different annealing times. Little amount of iron is diffused into copper in all samples, which is due to the low solubility of iron in copper. Relatively more iron diffuses into copper with longer annealing time.
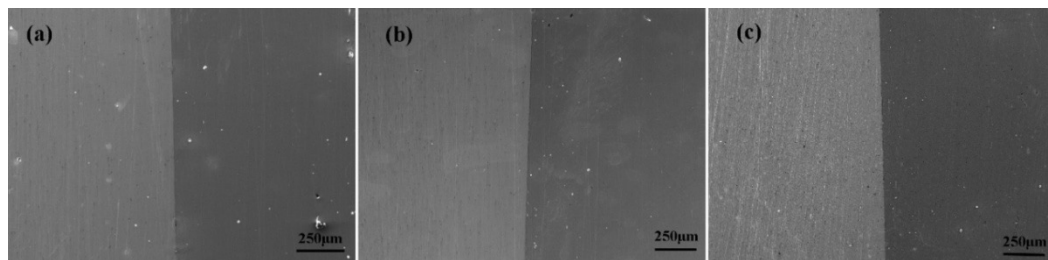
Figure 7.7 SEM images of interfaces with different annealing time, (a) 2 h (b) 4 h (c) 16 h
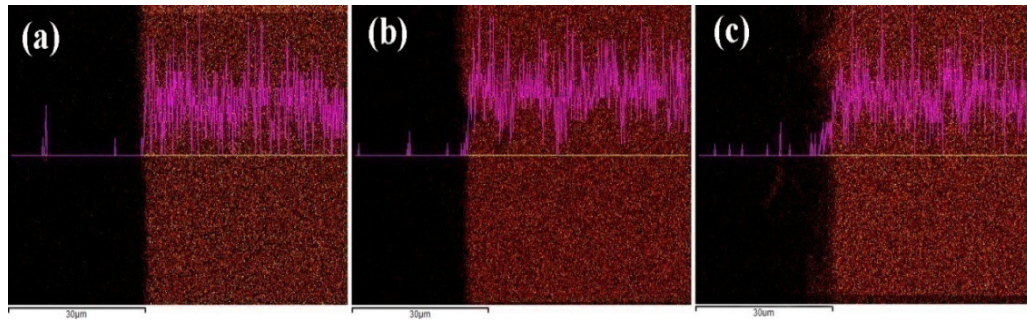
Figure 7.8 Energy Dispersive Spectroscopy (EDS) mappings and line profiles of Fe in the interfacial regions in samples annealed for (a) 2 h, (b) 4 h,and (c) 16 h.

7.2.2.2 Interfacial bond strength

Interfacial bonding strength was determined by measuring plastic deformation depth of the interfacial region. The indentation position was carefully chosen to make sure one of the diagonals of the indenter was along the interface using an optical microscope. Since the materials used to form the interfaces were the same, hardness of the materials had no effects on the indentation depths and the depths were only influenced by the interface strength. As shown in Figure 7.9, the sample with longer annealing time has smaller plastic deformation and thus exhibits stronger interfacial bonding strength, which is understandable since the sample with longer annealing time has larger diffusion distance in the interfacial region as illustrated in Figure 7.8.
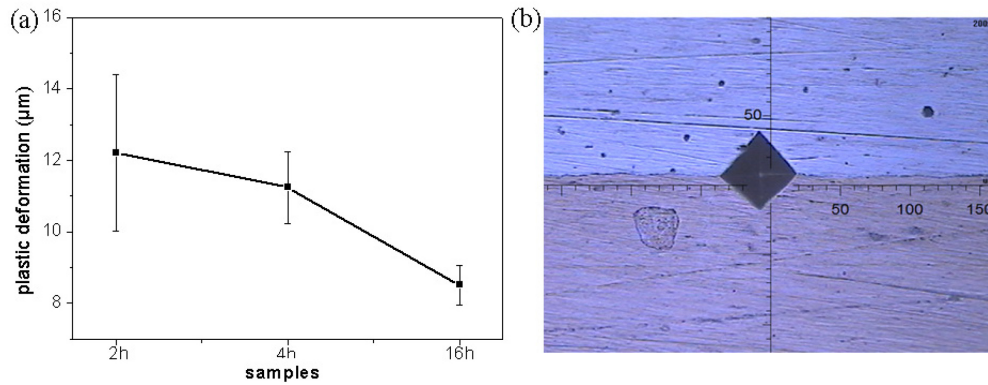
Figure 7.9 (a) plastic deformation depths in the interfacial region for samples with different annealing times (b) the indentation position in the interfacial region

7.2.2.3 EWF in the interfacial region

EWFs in the interfacial regions were mapped by KPFM and the scan region sizes were $20\mu\text{m} \times 20\mu m$. As illustrated in Figure 7.10, one may see the EWF difference for steel and copper in the interface sample and EWF in the interfacial region changes from copper's EWF to steel's EWF gradually. The EWF change slopes in the interfacial regions of samples with different annealing time are shown in Figure 7.10(c). Samples with longer annealing time have smaller EWF change slopes. As illustrated in Figure 7.9, the samples with longer annealing time possess stronger interfacial bond strength. Clear correlation between the interfacial property and interfacial EWF change slope can be observed in the copper-steel interfaces.
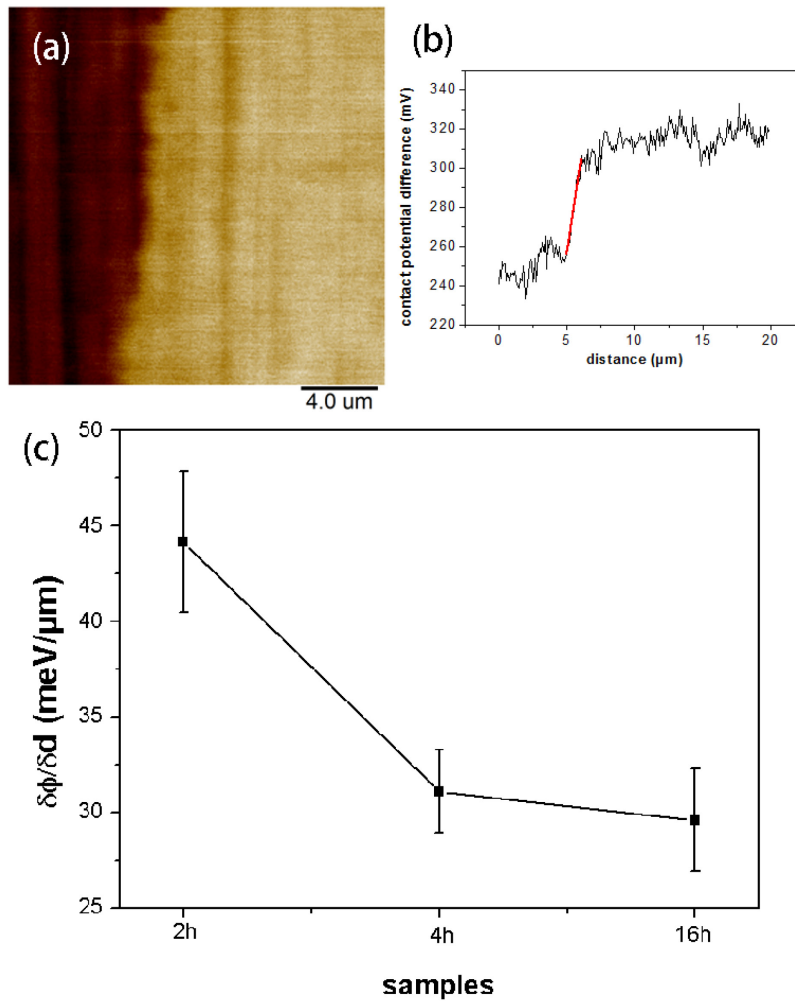
Figure 7.10 (a) EWF map in the interfacial region, bright region represents larger contact potential difference with AFM tip and thus low EWF and dark region represent high EWF (b) a representative contact potential line profile in the interfacial region, corresponding to change in EWF in the interfacial region (c) EWF slopes in the interfacial region for samples annealed for different durations

7.2.2.4 Correlation between interfacial EWF gradient or slope and interfacial bonding

The bond strength and adhesive energy between two surfaces are fundamentally described by the relation between the total energy and an appropriate atomic separation. Strong interactions may occur between metals when their surfaces are in initial contact, and there could be significant changes in electronic structures as a function as separation distance. The energy-distance relationship can be determined experimentally or through first-principles simulations. However, such studies are difficult and complicated [166,167]. A relatively simple universal relationship between adhesive energy and separation distance was proposed in the literature [166-168], which provides a simple prediction for adhesive energy and the inputs are only equilibrium binding energy and equilibrium electron density of the two metals in contact.

The interfacial bond strength is defined by the interface adhesive interaction energy which has a negative value, representing the amount of work to result in interface separation [166]

$$E_{ad} = [E(a) - E(\infty)] \big/ 2A \tag{7.4}$$

where E is the total energy, (a=0 when surface atoms of the two surfaces are separated with a spacing which equals the average of the bulk lattice parameters of the two metals).

Universal relationship between adhesive energy and electron density versus the separation distance between the two metal interfaces was found by solving the adhesive energy equations and more details can be found in the literature. [166,168].

As seen in Figure 7.11(a), electron density in the interfacial region changes gradually from the electron density of metal 1 to metal 2 when the two metals are in contact perfectly without gap. However, the charge distribution gradient in the interfacial region increases rapidly as the separation distance between the two metal surfaces increases. EWF is proportional to the valence electron density [51,148], as expressed in Eq. (7.5),

$$\varphi = \frac{e^3 m^{1/2} n^{1/6}}{16\pi^{5/3} 3^{1/3} \hbar \varepsilon_0^{3/2}} \tag{7.5}$$

where n is the equilibrium valence electron density, e is the elementary charge, m is the electron mass, ε_0 is the vacuum permittivity, and $\hbar$ is Planck constant. It is expected that the relationship between EWF and separation distance between two surfaces is similar to the relationship between electron density and the separation distance, *i.e.,* EWF change gradient increases as the separation distance between two surfaces increases. It is consistent with the EWF change slopes shown in Figure 7.10; the samples with longer annealing time possess a better interfacial bonding and a smaller EWF slope or gradient.

Figure 7.11(b) illustrates the adhesive energy between the two surfaces as a function of the separation distance between the surfaces. The scaled separation distance and scaled adhesive energy are defined as

$$a^* = (a - a_m)/l \tag{7.6}$$

$$E_{ad}^*(a^*) = E_{ad}(a)/\Delta E \tag{7.7}$$

where l is average of Thomas-Fermi screening lengths of two metals, a is separation distance and a_m is equilibrium separation distance, ΔE is the adhesive energy at the equilibrium distance.
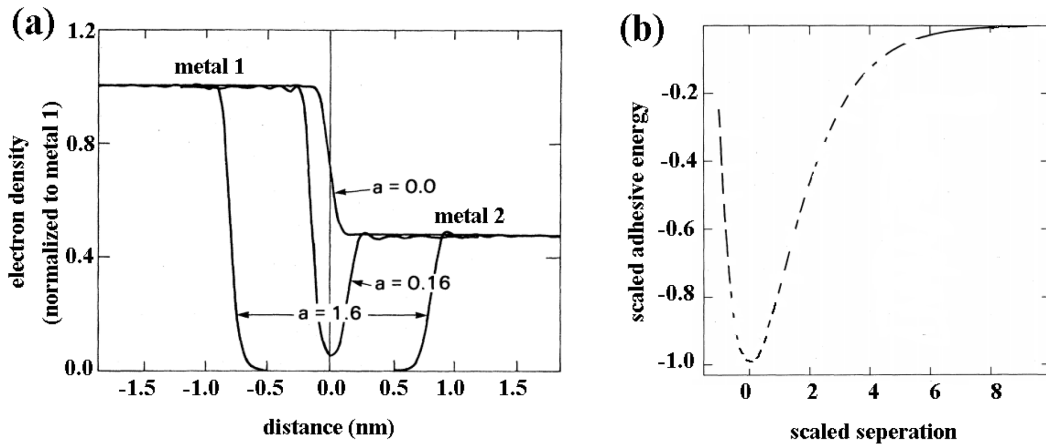
Figure 7.11 (a) electron density as a function of position in the interface region for two metals contact, a represents the separation distance between two metals (b) adhesive energy versus separation distance between two metal surfaces

One may see that the adhesive energy reaches a maximum when the two surfaces are in contact at the equilibrium distance (scaled separation equals to zero), and the adhesive energy decreases when the distance between two surfaces is larger or smaller than the equilibrium distance. Comparing Figure 7.11(a) and Figure 7.11(b), it is of interest to note that when the separation distance between two

surfaces equals zero, the charge density distribution gradient at the interface region is smallest and the adhesive energy reaches a maximum, while the adhesive energy decreases as the separation distance increases and the interfacial charge distribution gradient increases. It is consistent with the experimental results shown in Figure 7.9 and Figure 7.10 that the interfaces with longer annealing time possess stronger interfacial bonding strength and smaller EWF change slope.

The above discussions only take account of the initial contact of two surfaces and the electronic interactions; however, diffusion is another important issue that needs to be considered in the metal-metal interface. Elastic modulus of the interface can be expressed approximately as [169], if there are no interfacial defects, *e.g.*, microvoids, due to interfacial diffusion,

$$E_{\mathrm{interface}} = \frac{E_1 E_2}{E_1 + E_2} \tag{7.8}$$

Since mechanical properties of metals, such as elastic modulus, yield strength, are proportional to EWF to the sixth power, *i.e.,* $E \propto \varphi^6$ $\sigma_\mathrm{y} \propto \varphi^6$ [71,72,115], so we have

$$E_{\mathrm{interface}} = \frac{E_1 E_2}{E_1 + E_2} \propto \frac{\varphi_1^6 \varphi_2^6}{\varphi_1^6 + \varphi_2^6} = \frac{\varphi_2^6}{1 + \left(\dfrac{\varphi_2}{\varphi_1}\right)^6} \tag{7.9}$$

EWF of the two metals can be expressed approximately as [170]

$$\varphi_1 = x_A \varphi_A + (1\text{-}x_\mathrm{A})\varphi_B, \varphi_2 = (1\text{-}x_\mathrm{B})\varphi_A + x_B \varphi_B \tag{7.10}$$

where φ_1 φ_2 are EWFs of the two surfaces with diffusion and φ_A φ_B are EWFs of the two surfaces without diffusion, x_A x_B are diffused atomic percentages of the two surfaces. To make it simple, let $x_A = x_B$, substitute Eq. (7.10) into Eq. (7.9), we can get the interfacial bonding strength as a function of diffusion. As illustrated in Figure 7.12, the interfacial bonding becomes stronger as more atoms diffuse to the other side of the interface, which is consistent to the experimental results illustrated in Figure 7.9.
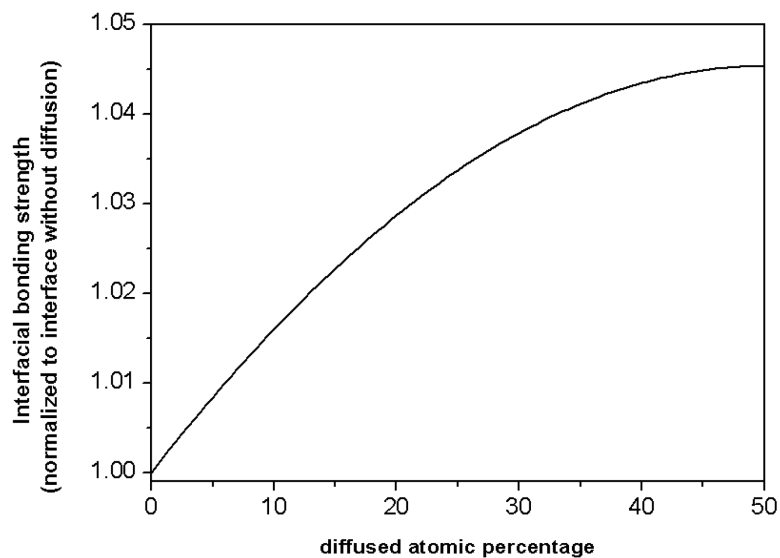
Figure 7.12 Interfacial bonding strength as a function of diffusion

7.2.3 Remarking comments

The correlation between interfacial EWF change gradient of metal-metal interfaces and interfacial bonding strength was investigated. It was demonstrated

that interfaces with smaller EWF change gradient possess stronger interfacial bonding, which is due to both electronic interactions when the two surfaces contact initially and atom diffusion when the interfaces form. This study demonstrates that EWF could be used to characterize interfacial bonding, especially for coatings or film samples with small sizes or irregular shapes which are difficult to be tested using conventional measurement methods.

7.3 Summary

It has been demonstrated that EWF is related to many properties of materials, such as mechanical strength, intrinsic ductility, surface energy, *etc.* In this chapter, based on the previously established correlations between EWF and properties of materials, two EWF applications in materials characterizations are explored. It demonstrates that (1) the fracture toughness of materials can be reflected by corresponding changes in EWF caused by repeated hammering, and (2) interfaces with smaller EWF gradients possess stronger interfacial bonding. The studies show that EWF is an indicative parameter for analyzing fracture toughness and interfacial bonding strength of materials, especially promising in analyzing coatings/films and small samples with irregular shapes, which are difficult to evaluate using conventional methods.

Chapter 8 Explore EWF as an indicative parameter for supplementary clues towards effective tailoring of wear-resistant materials

We have conducted considerable studies to investigate the correlation between EWF and properties of metallic materials, such as mechanical properties, surface energy, and corrosion resistance, *etc*. The studies reported in Chapters 3 to 7 have demonstrated that EWF is a promising parameter, which provides an alternative approach for materials characterization and supplementary clues for materials tailoring on a feasible electronic base.

This chapter reports a case study of using the established correlations between EWF and mechanical properties of materials in materials characterization and design. The materials under study are high chromium cast irons (HCCIs). The work reported in this chapter has been published in Materials Science and Engineering, A 669 (2016) 396-402 [171] entitled "Explore the electron work function as a promising indicative parameter for supplementary clues towards tailoring of wear-resistant materials," by Jian Wang, Hao Lu, Bin Yu, Rongfeng Wang, Guomin Hua, Xianguo Yan, Leo Parent, Harry Tian, Reinaldo Chung and Dongyang Li.

8.1 Introduction

Many materials used under dynamic loading conditions are required to possess both high hardness and high toughness. High-Cr cast irons (HCCIs) are such a type

of material, which are widely used as a wear-resistant material to resist abrasion and erosion in various industrial sectors, including mining, mineral processing, cement production, oil sands operations, and paper manufacturing, *etc.*[172,173]. The performance of HCCIs strongly depends on their microstructure, including the volume fraction, distribution and morphology of carbides [174,175] and properties of both the carbides and the ferrous matrix. HCCIs are generally hard with relatively low toughness. For wear under various wearing and loading conditions, both high hardness and toughness are desired [176] and they need to be appropriately balanced. Determination of such a balance is challenging, since the toughness depends on both the mechanical strength and ductility. These two properties change in opposite directions when modified by, *e.g.,* alloying elements and heat treatment. This complicates the judgment or determination of approaches for modifying HCCIs.

Since HCCIs are generally hard, hardness is a less sensitive parameter used to guide HCCI design or modification [177]. For applications involving dynamic loading or impact such as solid-particle erosion at high velocities, more attention may need to be put on the fracture toughness. However, since toughness is a product of the strength and ductility, and HCCIs' ductility is generally low, it is difficult to determine the optimal balance between hardness and toughness for maximized performance of HCCIs under various wearing conditions. Besides, local defects, undesired phases and interfaces could trigger local cracking and subsequent global failure, which makes it more difficult to control the hardness-toughness balance. Thus, one has to perform a large number of trial-and-error tests, which is costly and time-consuming with limited effectiveness.

Hardness, toughness, EWF, and resistances to sliding wear and solid-particle

erosion for a number of HCCIs are investigated in this study. Particular attention is paid to possible correlations between EWF and the properties of the HCCIs.

8.2 Experimental details

A set of HCCIs samples were fabricated using an induction furnace and the compositions of the HCCIs are given in Table8.1. The alloys contained 45%Cr and 4%C or 27%Cr and 2.5%C with other minor elements balanced by iron.

Hardness of the samples was measured using a Mitutoyo hardness tester under a load of 5 N for 20 s. Each hardness value is an average of 10 measurements made at randomly selected locations on each sample. Toughness of the HCCIs was evaluated by Charpy impact tests. Each reported toughness value is an average of three measurements. Dimensions of samples for the impact test were $55 \times 10 \times 2$ mm.

Sliding wear tests were performed on a pin-on-disc tribometer (CSEM Instruments, Neuchatel, Switzerland). The disc was the sample under study (15 mm $\times$ 8 mm $\times$ 5 mm) and the pin was a silicon nitride ball with its diameter equal to 6 mm. All tests were performed at a sliding speed of 2 cm/s along a circle path of 2.0 mm in diameter under a normal load of 10 N for 9,000 rotations. Each wear test was repeated at least 3 times. Wear tracks and corresponding volume losses of the samples were determined using a confocal microscope. (ZeGage 3D optical profilometer, Zygo Corp.)

Table 8.1 Nominal composition of HCCIs under study and their impact energy values

Sample	%Cr	%C	%Mn	%B	%Y	%Si	%V	%Ni	%Mo	Impact energy (J/cm^2)	Hardness(HRC)
B0	45	4	0	0	0.5	0	0	0	0	2.1 ± 0.4	48.9 ± 1.5
B2	45	4	2	0	0.5	0	0	0	0	2.4 ± 0.5	52.0 ± 1.3
B5	45	4	1	0.5	0.5	0	0	0	0	2.0 ± 0.6	63.0 ± 0.6
B12	45	4	4	1	0.5	0	0	0	0	1.7 ± 0.3	64.1 ± 0.5
B16	45	4	4	1.5	0.5	0	0	0	0	1.5 ± 0.4	71.0 ± 0.7
B20	45	4	4	2	0.5	0	0	0	0	1.7 ± 0.2	63.0 ± 0.9
C1	27	2.5	0	0	0	0.8	0	0	0	2.5 ± 0.4	63.3 ± 0.5
C2	27	2.5	0	0	0	0	0	0.5	2	3.1 ± 0.5	63.0 ± 0.6
C3	27	2.5	1	2	0	0.5	6	1	2	2.3 ± 0.4	70.0 ± 0.1

Solid-particle erosion tests were carried out using a home-made air-jet erosion tester. The erosion tests were performed at an impingement angle of 90° and a dry air flow was used to eject sand particles, generating a sand particle flow at a velocity of 55 m/s. The sand particle flow was delivered through a superalloy nozzle with its inner diameter equal to 4 mm. Each test consumed 2125 g fine sand (AFS 50–70) and the mass flow rate for the test was set at 177 g/min. The distance between the nozzle and sample surface was 10 mm. The purpose of using the high particle velocity and impingement angle of 90° was to perform the erosion tests under a condition in which the material toughness played a more important role in resisting erosion damage under larger impact forces. Weight losses of the samples caused by erosion were determined by weighing each sample before and after testing using a balance with an accuracy of 0.1 mg. Three erosion tests were performed for each HCCI and results obtained were averaged.

Microstructures of the samples were examined using a scanning electron microscope (Tescan Vega 3 SEM, Czech Republic).

EWFs of HCCIs were measured in air at room temperature using a scanning Kelvin probe (SKP 5050, KP Technology Ltd. UK). Before the testing, samples were polished using 400, 600, 800, 1200 grit sand papers successively to minimize the influence of roughness on EWF measurements. The polished surface was cleaned using an ultrasonic cleaner with reagent alcohol for 3 min and dried using an air flow. The EWF measurements were carried out right after the polishing and cleaning process in order to avoid surface contamination. A reference gold tip with 2 mm diameter was used to measure the contact potential difference between the tip and the sample. During the measurement, a sample surface was scanned by the SKP, which covered 25 spots, and at least three different regions on each sample were scanned for statistically reliable results. Since the tip size of the Kelvin probe is on mm scale, it collects signals from a relatively large area. Thus, what the Kelvin probe measures is the overall work function of an area under study.

8.3 Results and discussion

8.3.1 Microstructure

Microstructures of the alloys were observed using SEM. Figure 8.1 illustrates representative images of the alloys. As shown, except C1 and C2 in the hypoeutectic state, the others are in the hypereutectic state.
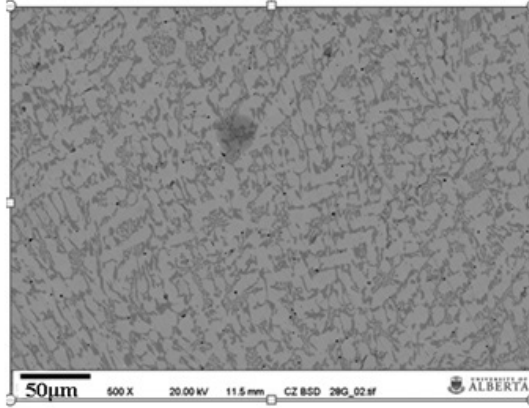
C1
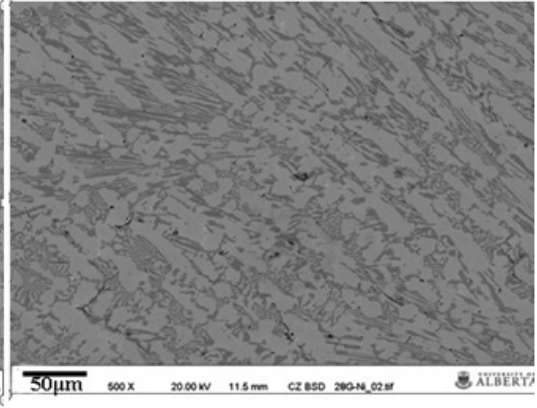
C2
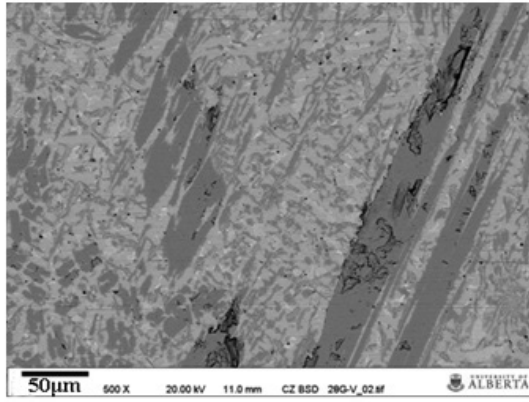
C3
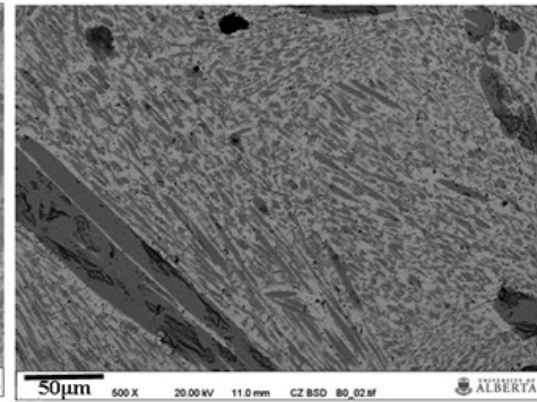
B0
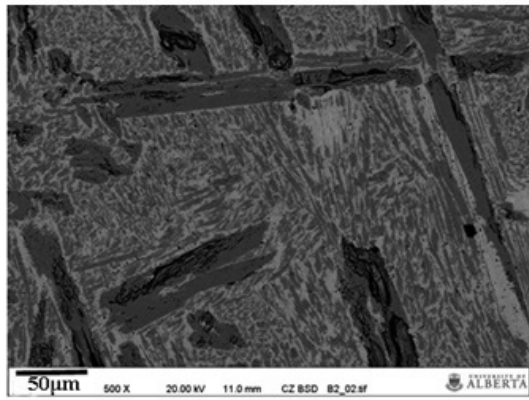
B2
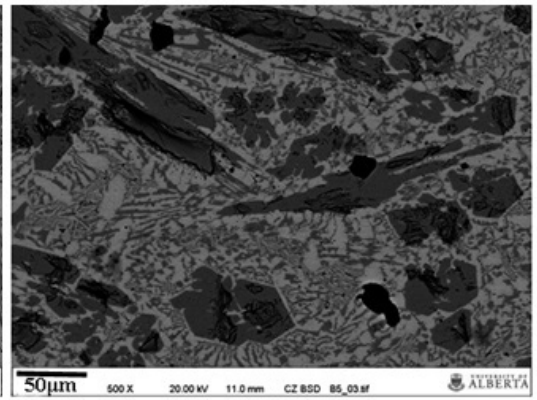
B5
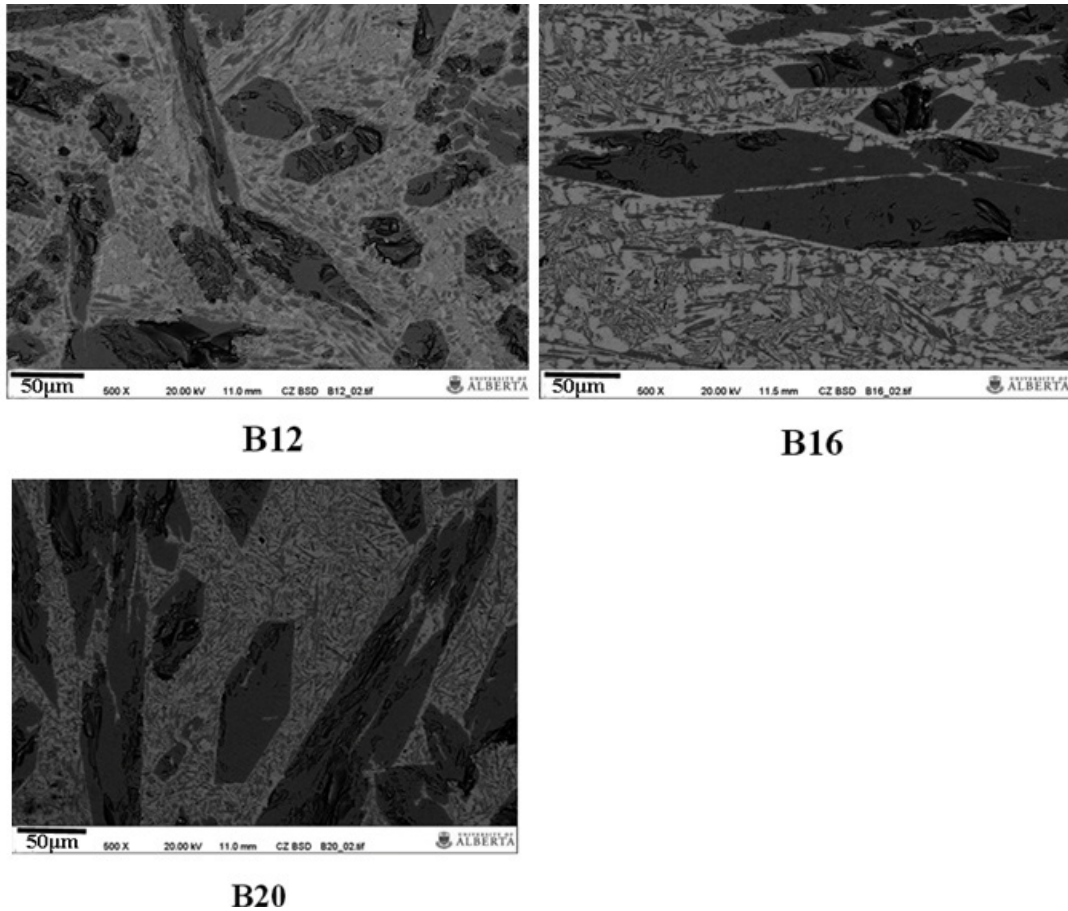
Figure 8.1 Microstructures of the sample alloys under study

8.3.2 Wear behavior and its dependence on hardness, toughness and EWF

The performances of the alloys during wear testing in two wear modes, abrasion and solid-particle erosion, were evaluated using pin-on-disc (abrasion) and air-jet solid-particle erosion testers. Results of the tests are illustrated in Figure 8.2. In Figure 8.2(a), values of hardness and fracture toughness of the alloys are also presented in order to see how the wear behavior is affected by the properties.

As shown, alloys having more hypereutectic features, *e.g.*, B12, B16 and B20, are harder but less resistant to wear. In general, increasing hardness of ductile materials enhances their wear resistance [178,179]. However, the high-Cr cast irons, which are hard, do not follow this trend well. Further increasing their hardness by introducing more carbides reduces their toughness and, consequently, renders them less resistant to fracture, leading to lowered resistance to wear. This can be seen more clearly under the high-velocity solid-particle erosion condition. In this case, the high-velocity particle impingement causes more damage to harder and less tough materials. Impact energies for fracture of the alloys are given in the figure, which support the above statement. As shown, alloys having higher wear resistances were generally tougher. However, toughness, as a measure of energy consumed to cause failure, is a product of strength and ductility. A fixed toughness value may correspond to low strength but large ductility or high strength but low ductility. Thus, with known hardness and toughness, how to further optimize the material (*i.e.*, increase hardness or ductility) with precise guidelines still remains unclear.

EWF of the alloys were measured and are presented in Figures 8.2(b)-(d). As illustrated, HCCIs with lower EWFs show higher resistance to wear especially to solid-particle erosion. Compared to hardness and toughness, this parameter appears to be a clear indicative parameter that categorizes the high-Cr cast irons in terms of their wear resistance.
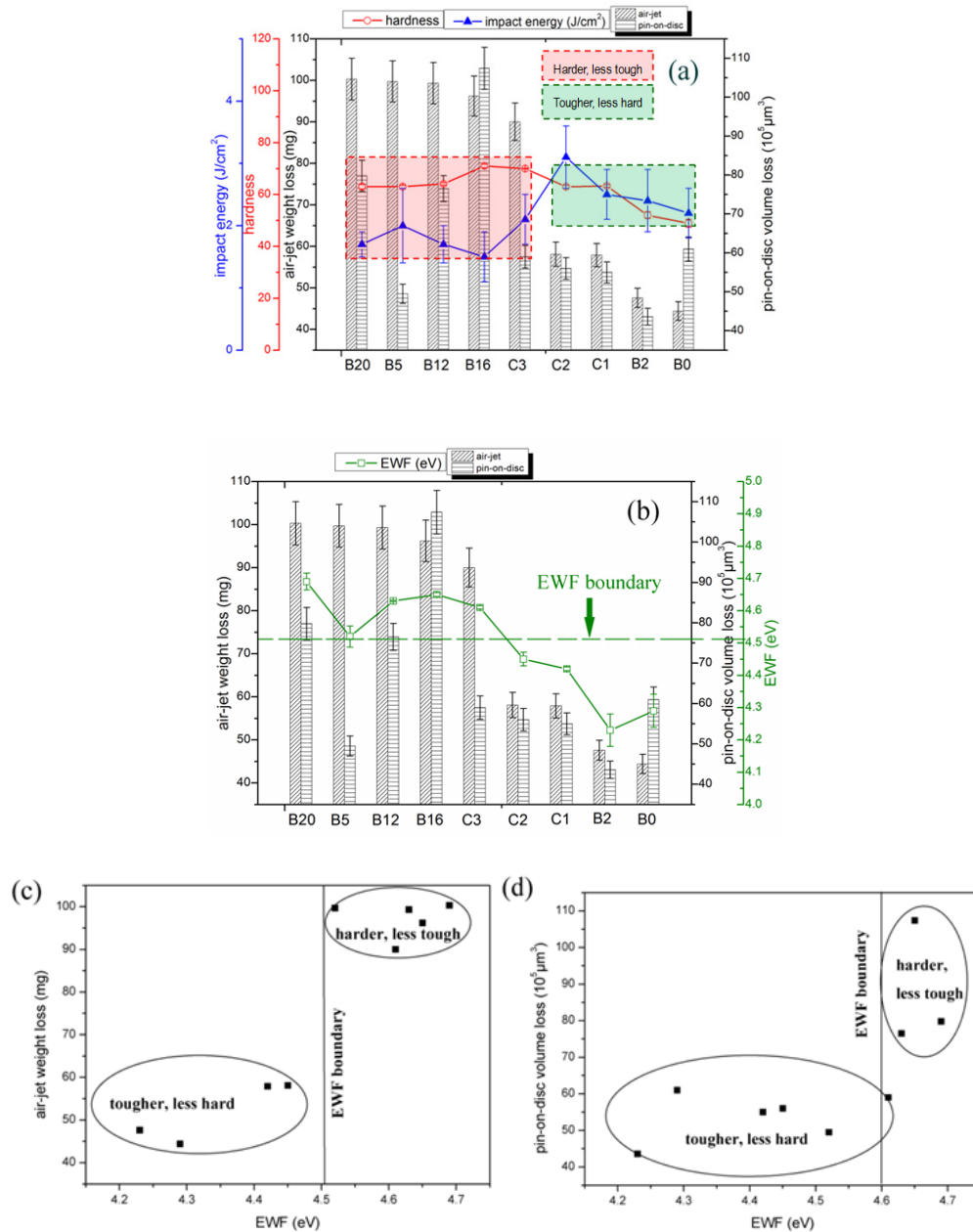
Figure 8.2 (a) material losses of the HCCIs caused by wear and their hardness and impact energy (fracture toughness); (b) material loss with respect to EWFs; (c) weight loss caused by erosion versus EWF; (d) volume loss caused by abrasion versus the EWF.

8.3.3 Analysis on the relation between wear and EWF

The effectiveness of EWF in categorizing HCCIs is attributed to the fact that EWF reflects both hardness and toughness, which are crucial factors governing the wear resistance. As discussed in section 2.2.4.6 and section 2.2.4.8, it has been demonstrated that hardness is proportional to φ^6 [72]. EWF is also related to material ductility and toughness [73]. From the view-point of charge redistribution in an external field, the material intrinsic ductility is correlated to the polarizability, on which material fracture is dependent [73,180,181]. In an electric field E, the charge distribution creates a dipole moment in the direction of the applied electric field. The relative tendency of a charge distribution, known as the polarizability [182], deceases with respect to the EWF as shown in Figure 8.3(a). A material having a higher polarizability is more flexible, corresponding to larger ductility or ductile fracture features when it is stretched. Small polarizability generally leads to brittle fracture. Electrons are less mobile in a metal with a higher EWF. Or in other words, the electrons are more confined by nuclei or more localized, thus leading to stronger atomic bonding or higher strength but less ductile behaviour as Figure 8.3(b) schematically illustrates. Such a trend has been observed for different types of material. For instance, an increase in polarizability of alkali halides results in a clear decline of their cleavability; similar trends are observed for metals and polymers as well [183].
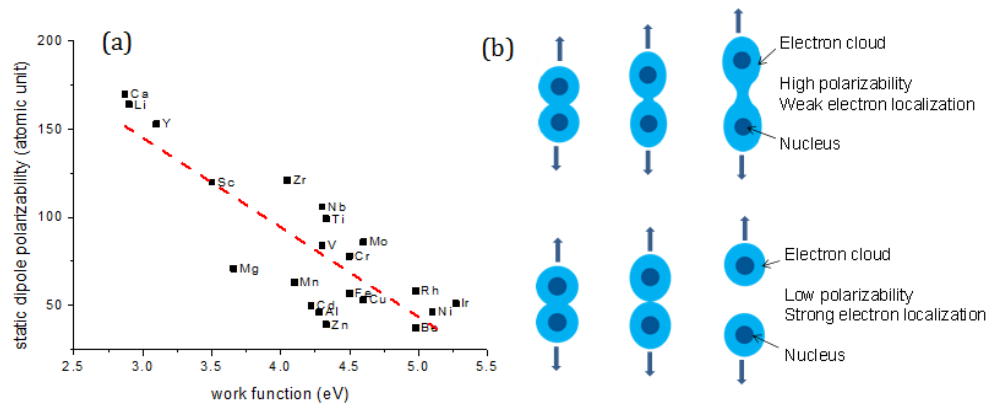
Figure 8.3(a) Relationship between EWF and the polarizability; (b) schematic illustration of the relationships among the polarizability, electron localization and atomic separation or displacement under the external force

Based on the relationship between EWF and mechanical strength and polarizability, which is related to ductility, as well as the fact that the material toughness is a product of strength and ductility, one may expect that the material toughness should increase upon increasing the EWF and then decrease after reaching a certain value. As discussed in section 2.2.4.8, there is an approximate trend between EWF and fracture toughness of metals. A peak of K_{IC} exists around $\varphi = 4.5 \sim 4.6eV$, which could be regarded as a boundary. Below this boundary, the material behaves in a ductile manner with lower strength. Above the boundary, the material becomes harder but brittle. For HCCIs which are generally hard, ductility should play a more crucial role in determining their resistance to wear. The lower EWFs of B2, B0, C1 and C2 imply that these HCCIs are relatively ductile and thus possess higher toughness as Figure 8.2(a) illustrates. This may explain why the HCCIs with lower EWF performed better than those having higher EWFs as

illustrated in Figures 8.2 (b)-(d).

In terms of material design, below the boundary, increasing the mechanical strength makes a material tougher; while above the boundary, increasing the strength may deteriorate the material with lowered toughness.

8.4 Summary

In this chapter, hardness, fracture toughness, EWF, and resistances to sliding wear and solid-particle erosion for a number of high-Cr cast irons (HCCIs) are investigated. It was shown that the wear resistance of the HCCIs was not sensitive to their hardness while their fracture toughness was more influential. Since the toughness is determined by both the mechanical strength and ductility, which vary in opposite directions when modified by, *e.g.*, alloying elements and heat treatment, it is challenging to identify an appropriate balance between strength and ductility. In this work, it was observed that HCCIs having low EWFs performed better than those having higher EWFs. The EWF categorizes the materials well. There appears to be a boundary of EWF around 4.5~4.6 eV, below which HCCIs show higher wear resistance than those with their EWFs above the boundary. Efforts are made to elucidate underlying mechanisms. This study demonstrates that EWF is a promising indicative parameter for categorizing materials and a supplementary clue for judging the balance between hardness and toughness towards effective modification of materials.

Chapter 9 Remarking Comments, general conclusions and possible future studies

9.1 Remarking comments

In this thesis study, it is demonstrated that EWF is a promising guiding parameter for material characterization and design. It should be, however, pointed out that the EWF measurement is sensitive to the sample surface condition, thus it is essential to ensure that the surface conditions of different samples under study are the same or similar in order to obtain comparable results. As discussed in sections 2.2.4.10 and 2.2.5.4, surface roughness, adsorption, and oxidation film influence the EWF measurement. As demonstrated, EWF decreases with an increase in the surface roughness [76]. In order to minimize the influence of roughness on EWF measurement, surfaces of the samples under study should be prepared under the same conditions, *e.g.*, being polished using same grit sand papers and finally polished in a slurry containing fine diamond particles to achieve similar roughness. Since polishing introduces a plastically deformed thin layer, one may etch the polished surfaces to remove (through dissolution) the deformed thin layer.

Possible adsorption and oxidation may also influence EWF of the sample surface. Adsorption may result in the redistribution of the electron density on the surface and reconstruct the surface structure, leading to changes in the EWF value [15, 37, 40]. If the adsorbate is more electronegative than the substrate, electrons will transfer to the adsorbate layer, leading to an increase in electron density and EWF of the sample surface. On the contrary, a decrease in EWF of the surface is expected for electropositive adsorbates [15]. The oxidation film on the sample surface may also

increase EWF of the sample [75]. Thus, for sample preparations as described in this thesis, the polished surface was cleaned using an ultrasonic cleaner with reagent alcohol, and its EWF was measured immediately after it was dried in order to minimize the influence of adsorption/contamination. If oxidation exists, after a possible oxide film is removed by polishing, or polishing followed by light etching (for removal of the deformed thin layer), and the surface is cleaned, EWF of the surface is immediately measured. Since etching could also introduce a thin layer, etching could influence EWF measurement as well. However, our experience shows that although polishing alone and polishing with subsequent etching more or less influence the measured EWF value, they generally do not affect the trend or ranking of work functions of different samples. Besides, they help minimizing the influences of surface roughness, contamination and oxidation, making the measured EWF closer to the intrinsic EWF of materials.

9.2 General conclusions

In this thesis study, relationships between EWF and properties, especially mechanical properties, of metallic materials are investigated. Clear correlations between EWF and mechanical properties of materials are shown both experimentally and theoretically. It demonstrates that EWF could be used as a guiding parameter for material characterization and design. This parameter is promising to build a bridge towards the development of alternative or complementary approaches or methodologies for materials design on a feasible electronic base.

● Based on the dependence of Young's modulus on EWF, several bond

energy-related properties including bulk modulus, thermal expansion and Debye temperature are correlated to EWF using the Lennard-Jones potential as a bridge.

- A method to extract the EWFs of binary solid solutions from their phase diagrams is proposed. EWF of a binary solid solution could be calculated from the solvus line in the binary phase diagram with the quasi-chemical treatment.

- Correlation between EWF and Young's modulus as well as hardness of solid solutions with respect to the composition is investigated. Young's modulus and hardness of the alloy increase as the EWF increases in a sixth power relationship approximately.

- A single-parameter model using EWF as an indicator to evaluate the capability of solute atoms in solid solution hardening is proposed. It predicts that the larger the EWF difference between solute atom and host atom, the more effective is the solute for hardening, and the solute with larger EWF is more effective in solid-solution hardening.

- The changes in Young's modulus and hardness with respect to composition show trends similar to that of change in EWF no matter whether or not a second phase is present. The similar trends suggest that the overall mechanical behavior is related to the overall EWF to a certain degree, although the former is microstructure dependent.

- An approach of using EWF as an indicator in evaluating fracture toughness of hard metallic materials is demonstrated. Samples with lower fracture toughness

reveal larger decreases in EWF caused by the repeated hammering.

● The correlation between interfacial EWF change gradient of metal-metal interfaces and interfacial bonding strength is investigated. It demonstrates that interfaces with smaller EWF change gradients possess stronger interfacial bonding.

● It is observed that HCCIs having low EWFs performed better than those having higher EWFs during wear tests. The EWF well categorizes the materials. There appears to be a boundary of EWF around 4.5~4.6 eV, below which HCCIs show higher wear resistance than those with their EWFs above the boundary.

9.3 Future studies

● Based on the studies reported in Chapter 6, it appears that the overall EWF integrates EWFs of individual microstructure constituents (phases, interfaces) and their mutual influence or synergy. Such an integrated EWF may reflect material properties to a certain degree. However, more studies are needed for comprehensive understanding of the microstructure-EWF-property relationships and underlying mechanisms.

● In Chapter 5, a single-parameter model is proposed using EWF as an indicator to evaluate the capability of solute atoms in solid solution hardening. However, it cannot explain well possible solid solution softening phenomenon reported in the literature. Further theoretical studies on solute softening phenomenon and an improved model are needed.

- Based on the studies reported in Chapters 3-6, clear relationships between EWF and mechanical properties of materials are demonstrated. However, relatively large data scatter still exists in the theoretical fitted curves, due to the simplicity of the model and error in experiments (*e.g.*, surface condition). More studies to improve the theoretical models and more accurate experimental arrangements are required. More samples and different kinds of materials are needed to be tested to verify the proposed relationships between EWF and mechanical properties of materials, in order to generalize the proposed models in materials design.

- Studies shown in Chapter 7 demonstrate that EWF is an indicative parameter for analyzing fracture toughness of hard and less tough materials, especially promising for analyzing fracture toughness of hard protective coatings or thin films, which cannot be evaluated using conventional techniques. However, the sample materials used in the study are bulk cast irons rather than coatings. Further studies directly using coating samples to verify the proposed testing method are needed. Further studies for optimal testing conditions are also required.

- Correlation between the interfacial EWF gradient and interfacial bonding strength was investigated and reported in Chapter 7. Whether the proposed correlation is still applicable for metal-ceramic interfaces or ceramic-ceramic interfaces needs more studies. Theoretical models are also required for better understanding the correlation and using it in interfacial analysis.

- Studies presented in this thesis are focused on mechanical properties of metallic

materials. More studies for the correlations between EWF and other properties and studies for ceramics materials or polymers are desired in order to expand the applications of EWF.

- Sample surface preparations and EWF measurement are conducted in air in the studies. If the experiments can be conducted in vacuum or in protective conditions, it is possible to minimize the influence of surface conditions on EWF measurements to obtain more accurate results. It is also possible to study the influence of adsorption and gas atom diffusion in materials [184].

- KPFM is a tool that enables nanometer scale imaging EWF for a wide range of materials [58]. Studies in this thesis use SKP and KPFM for micrometer scale imaging to investigate the dependence of mechanical properties of alloys on EWF. Upon applying nanometer scale imaging capability of KPFM, it is possible to understand microstructure-EWF-property relationships more deeply. It is also expected that EWF can be applied in nanostructure materials research.

References

1   Allen, N., Schofield, T. & Tate, A. Mechanical Properties of α-Solid Solutions of Copper, with Zinc, Gallium, Germanium and Arsenic. *Nature* **168**, 378-379 (1951).

2   Tiwari, G. & Ramanujan, R. Review The relation between the electron to atom ratio and some properties of metallic systems. *J Mater Sci* **36**, 271-283 (2001).

3   Levitin, V., Liskutov, S. & Pogosov, V. Influence of deformation and residual stresses in metals on the electronic work function. *Physics of metals and metallography* **70**, 70-76 (1990).

4   Loskutov, S. V., Levitin, V. V., Pogosov, V. V. & Pravda, M. I. Change of Electron Work Function under Influence of Metal Deformation. *Fizika Metallov I Metallovedenie* **79**, 3-7 (1995).

5   Levitin, V., Loskutov, S., Pravda, M. & Serpetzky, B. Influence of cyclic stresses upon the electronic work function for the metal surface. *Solid state communications* **92**, 973-976 (1994).

6   Levitin, V., Garin, O., Yatsenko, V. & Loskutov, S. On structural sensibility of work function. *Vacuum* **63**, 367-370 (2001).

7   Rueda, H. *et al.* in *MRS Proceedings.*   245 (Cambridge Univ Press).

8   Kiejna, A. & Pogosov, V. V. Simple theory of elastically deformed metals: Surface energy, stress, and work function. *Physical Review B* **62**, 10445 (2000).

9   Subramanyam, A. *Kelvin Probe For Surface Engineering : Fund And Design*. Chapter 3 (Ane Books Pvt Ltd, 2010).

10   Kittel, C. *Introduction to the Solid State Physics*. 8 edn, Chapters 3, 5& 17 (John Wiley & Sons, 2004).

11   Li, W. & Li, D. Y. Effects of elastic and plastic deformations on the electron work function of metals during bending tests. *Philos. Mag.* **84**, 3717-3727 (2004).

12   Li, W., Wang, Y. & Li, D. Y. Response of the electron work function to deformation and yielding behavior of copper under different stress states. *Physica Status Solidi a-Applied Research* **201**, 2005-2012 (2004).

13   Li, W. & Li, D. Y. In situ measurements of simultaneous electronic behavior of Cu and Al induced by mechanical deformation. *Journal of Applied Physics* **99**, 073502 (2006).

14   Li, D. Y. Kelvin probing technique: A promising method for the determination of the yield strain of a solid under different types of stress. *Physica Status Solidi a-Applied Research* **191**, 427-434 (2002).

15   Li, D. Y. & Li, W. Electron work function: A parameter sensitive to the adhesion behavior of crystallographic surfaces. *Applied Physics Letters* **79**, 4337-4338 (2001).

16   Li, W. & Li, D. Y. Exploring the application of the Kelvin method in studying the history prior to wear and the onset of wear. *Wear* **253**, 746-751 (2002).

17   Li, W. & Li, D. Y. A study on the kinetic response of the electron work function to wear. *Wear* **255**, 333-340 (2003).

18   Li, Y. & Li, D. Y. Experimental studies on relationships between the electron work function, adhesion, and friction for 3d transition metals. *Journal of Applied Physics* **95**, 7961 (2004).

19   Li, Y. & Li, D. Y. Electron work function, adhesion, and friction between 3d transition metals under light loads. *Wear* **259**, 1432-1436 (2005).

20   Li, Y. & Li, D. Y. Prediction of elastic-contact friction of transition metals under light loads based on their electron work functions. *Journal of Physics D: Applied Pysics* **40**, 5980-5983 (2007).

21   Li, Y. P. & Li, D. Y. An energy consumption model based on the electron work function and Fermi energy for predicting adhesion and low-load friction between 3d transition metals. *Wear* **263**, 1610-1615 (2007).

22   Callister, W. *Materials Science and Engineering an Introduction*. 5 edn, Chapter 1, 2& 7, (John Wiley & Sons, 2000).

23   Chen, M. A brief overview of bulk metallic glasses. *NPG Asia Materials* **3**, 82-90 (2011).

24   Lim, X. Metal Mixology. *Nature* **533**, 306-307 (2016).

25   Lee, J. G. *Computational materials science: an introduction*.   (Crc Press, 2016).

26   Fleisgher, R. L. Solution hardening. *Acta Metallurgica* **9**, 996-1000 (1961).

27   Hume-Rothery, W., Mabbott, G. W. & Evans, K. C. The freezing points, melting points, and solid solubility limits of the alloys of silver, and copper with the elements of the B sub-groups. *Philosophical Transactions of the Royal Society of London. Series A, Containing Papers of a Mathematical or Physical Character*, 1-97 (1934).

28   Hafner, J., Wolverton, C. & Ceder, G. Toward computational materials design: the impact of density functional theory on materials research. *MRS Bulletin* **31**, 659-668 (2006).

29   Leyson, G. P. M., Curtin, W. A., Hector Jr, L. G. & Woodward, C. F.

Quantitative prediction of solute strengthening in aluminium alloys. *NATURE MATERIALS* **9**, 750-755 (2010).

30   Chakraborti, N. Genetic algorithms in materials design and processing. *International Materials Reviews* **49**, 246-260 (2004).

31   Ikeda, Y. A new method of alloy design using a genetic algorithm and molecular dynamics simulation and its application to nickel-based superalloys. *Materials Transactions, JIM* **38**, 771-779 (1997).

32   Johannesson, G. H. *et al.* Combined electronic structure and evolutionary search approach to materials design. *Physical Review Letters* **88**, 255506 (2002).

33   Curtarolo, S. *et al.* The high-throughput highway to computational materials design. *NATURE MATERIALS* **12**, 191-201 (2013).

34   Kahn, A. Fermi level, work function and vacuum level. *Materials Horizons* **3**, 7-10 (2016).

35   Leung, T. C., Kao, C. L., Su, W. S., Feng, Y. J. & Chan, C. T. Relationship between surface dipole, work function and charge transfer:Some exceptions to an established rule. *Physical Review B* **68**, 195408 (2003).

36   Janata, J. Chemical Modulation of the Electron Work Function. *Analytical Chemistry* **63**, 2546-2550 (1991).

37   Demuth, J. E. & Rhodin, T. N. Chemisorption on (001), (110) and (111) nickel surfaces: A correlated study using LEED spectra, Auger spectra and work function change measurements. *Surface Science* **45**, 249-307 (1974).

38   Franken, P. E. C. & Ponec, V. Photoelectric work function measurements on nickel-copper and nickel-gold alloy films: Clean surfaces and adsorption of ethylene and carbon monoxide. *Journal of Catalysis* **42**, 398-407 (1976).

39   Bagus, P. S., Käfer, D., Witte, G. & Wöll, C. Work Function Changes Induced by Charged Adsorbates: Origin of the Polarity Asymmetry. *Physical Review Letters* **100**, 126101 (2008).

40   Benndorf, C., Klatte, G. & Thieme, F. Interaction of oxygen with CuNi(110) alloy surfaces: AES, XPS and work function measurements. *Surface Science* **135**, 1-17 (1983).

41   Yu, K. Y., Helms, C. R., Spicer, W. E. & Chye, P. W. Photoemission studies of the surface and bulk electronic structure of the Cu-Ni alloys. *Physical Review B* **15**, 1629-1639 (1977).

42   Li, W. & Li, D. Y. Influence of surface morphology on corrosion and electronic behavior. *Acta Materialia* **54**, 445-452 (2006).

43   Li, D. Y. Electron work function at grain boundary and the corrosion behavior of nanocrystalline metallic materials. Materials Research Society Symposium Proceedings **887**, 227-235 (2006).

44   Kiejna, A. & Wojciechowski, K. F. Work Function of Metals - Relation Between Theory and Experiment. *Progress in Surface Science* **11**, 293-338 (1981).

45   Samsonov, G. V., Fomenko, V. S., Podchernyaeva, I. A. & Okhremchuk, L. N. Thermionic emission properties of refractory compounds and materials based on them (a review). *Powder Metall Met Ceram* **13**, 836-842 (1974).

46   Michaelson, H. B. Work functions of the elements. *Journal of Applied Physics* **21**, 536-540 (1950).

47   Halas, S. 100 years of work function. *Materials Science-Poland* **24** (2006).

48   Lang, N. D. & Kohn, W. Theory of Metal Surfaces: Work Function. *Physical Review B* **3**, 1215-1223 (1971).

49   Skriver, H. L. & Rosengaard, N. Surface energy and work function of elemental metals. *Physical Review B* **46**, 7157 (1992).

50   Brodie, I. Uncertainty, topography, and work function. *Physical Review B* **51**, 13660-13668 (1995).

51   Halas, S. & Durakiewicz, T. Work functions of elements expressed in terms of the Fermi energy and the density of free electrons. *Journal of Physics: Condensed Matter* **10**, 10815 (1999).

52   Durakiewicz, T., Halas, S., Arko, A., Joyce, J. J. & Moore, D. P. Electronic work-function calculations of polycrystalline metal surfaces revisited. *Physical Review B* **64**, 045101 (2001).

53   Halas, S. & Durakiewicz, T. Physical foundations of the oxide cathodes. *Applied Surface Science* **252**, 6119-6121 (2006).

54   Park, Y., Choong, V., Gao, Y., Hsieh, B. R. & Tang, C. W. Work function of indium tin oxide transparent conductor measured by photoelectron spectroscopy. *Applied Physics Letters* **68**, 2699-2701 (1996).

55   Nonnenmacher, M., Oboyle, M. P. & Wickramasinghe, H. K. KELVIN PROBE FORCE MICROSCOPY. *Applied Physics Letters* **58**, 2921-2923 (1991).

56   Baikie, I. D. & Estrup, P. J. Low cost PC based scanning Kelvin probe. *Review of Scientific Instruments* **69**, 3902-3907 (1998).

57   Helander, M. G., Greiner, M. T., Wang, Z. B. & Lu, Z. H. Pitfalls in measuring work function using photoelectron spectroscopy. *Applied Surface Science* **256**, 2602-2605 (2010).

58   Melitz, W., Shen, J., Kummel, A. C. & Lee, S. Kelvin probe force microscopy and its application. *Surf. Sci. Rep.* **66**, 1-27 (2011).

59   Miedema, A. R. The electronegativity parameter for transition metals: Heat of formation and charge transfer in alloys. *Journal of the Less Common Metals* **32**, 117-136 (1973).

60   Michaelson, H. B. Relation Between an Atomic Electronegativity Scale and the Work Function. *Ibm Journal of Research and Development* **22**, 72-80 (1978).

61   Michaelson, H. B. The work function of the elements and its periodicity. *Journal of Applied Physics* **48**, 4729-4733 (1977).

62   Brajczewska, M., Henriques, C. & Fiolhais, C. Dependence of metal surface properties on the valence-electron density in the stabilized jellium model. *Vacuum* **63**, 135-138 (2001).

63   Halas, S., Durakiewicz, T. & Joyce, J. J. Surface energy calculation – metals with 1 and 2 delocalized electrons per atom. *Chemical Physics* **278**, 111-117 (2002).

64   Kalazhokov, K., Gonov, A. & Kalazhokov, Z. On the calculation of the surface energy of a face of a single crystal through the electron work function of this face. *Russian metallurgy. Metally*, 39-41 (1996).

65   Ji, D.-P., Zhu, Q. & Wang, S.-Q. Detailed first-principles studies on surface energy and work function of hexagonal metals. *Surface Science* **651**, 137-146 (2016).

66   Noy, A., Frisbie, C. D., Rozsnyai, L. F., Wrighton, M. S. & Lieber, C. M. Chemical Force Microscopy: Exploiting Chemically-Modified Tips To Quantify Adhesion, Friction, and Functional Group Distributions in Molecular Assemblies. *Journal of the American Chemical Society* **117**, 7943-7951 (1995).

67   Bagge, D., Hjelm, M., Johansen, C., Huber, I. & Gram, L. Shewanella putrefaciens adhesion and biofilm formation on food processing surfaces. *Applied and environmental microbiology* **67**, 2319-2325 (2001).

68   Guo, L. *et al.* Electron work functions of ferrite and austenite phases in a duplex stainless steel and their adhesive forces with AFM silicon probe. *Scientific Reports* **6**, 20660 (2016).

69   Li, W. & Li, D. Y. A simple method for determination of the electron work function of different crystallographic faces of copper. *Physica Status Solidi a-Applied Research* **196**, 390-395 (2003).

70   Howe, J. M. *Interfaces in Materials- Atomic Structure, Thermodynamics, and Kinetics of Solid-Vapor and Solid-Liquid Interfaces*. Chapters 2 & 3 (John Wiley & Sons Inc., 1997).

71   Hua, G. & Li, D. Generic relation between the electron work function and Young's modulus of metals. *Applied Physics Letters* **99**, 041907 (2011).

72   Hua, G. M. & Li, D. Y. The correlation between the electron work function and yield strength of metals. *Physica Status Solidi B-Basic Solid State Physics* **249**, 1517-1520 (2012).

73   Hua, G. & Li, D. Electron Work Function: A Novel Probe for Toughness. *Physical Chemistry Chemical Physics* (2016).

74   Liu, Z. & Li, D. The electronic origin of strengthening and ductilizing magnesium by solid solutes. *Acta Materialia* **89**, 225-233 (2015).

75   Xue, M. *et al.* Understanding of the correlation between work function and surface morphology of metals and alloys. *Journal of Alloys and Compounds* **577**, 1-5 (2013).

76   Li, W. & Li, D. Y. On the correlation between surface roughness and work

function in copper. *Journal of Chemical Physics* **122** (2005).

77   Rohwerder, M. & Turcu, F. High-resolution Kelvin probe microscopy in corrosion science: Scanning Kelvin probe force microscopy (SKPFM) versus classical scanning Kelvin probe (SKP). *Electrochim. Acta* **53**, 290-299 (2007).

78   Zharin, A. L. & Rigney, D. A. Application of the contact potential difference technique for on-line rubbing surface monitoring (review). *Tribology Letters* **4**, 205-213 (1998).

79   Gutman, E. M. *Mechanochemistry of Materials*. Chapters 2& 4, (Cambridge International Science Publishing, 1998).

80   Zharin, A., Fishbejn, E. & Shipitsa, N. Effect of contact deformation upon surface electron work function. *Journal of Friction and Wear C/C of TRENIE I IZNOS* **16**, 66-78 (1995).

81   Han, H. Q., Shi, C. B., Xu, W. M. & Carl, C. M. Effects of strain and strain rate on electronic behavior of metal surfaces under bending and tension tests. *Materials & Design* **31**, 633-635 (2010).

82   DeVecchio, D. & Bhushan, B. Use of a nanoscale Kelvin probe for detecting wear precursors. *Review of Scientific Instruments* **69**, 3618-3624 (1998).

83   Li, W. & Li, D. Y. Effects of dislocation on electron work function of metal surface. *Materials Science and Technology* **18**, 1057-1060 (2002).

84   Bhushan, B. & Goldade, A. V. Kelvin probe microscopy measurements of surface potential change under wear at low loads. *Wear* **244**, 104-117 (2000).

85   Wang, X. Y. & Li, D. Y. Beneficial effects of yttrium on the mechanical failure and chemical stability of the passive film of 304 stainless steel. *Materials Science and Engineering: A* **315**, 158-165 (2001).

86   Wang, X. Y. & Li, D. Y. Mechanical and electrochemical behavior of nanocrystalline surface of 304 stainless steel. *Electrochim. Acta* **47**, 3939-3947 (2002).

87   Wang, X. Y. & Li, D. Y. Mechanical, electrochemical and tribological properties of nano-crystalline surface of 304 stainless steel. *Wear* **255**, 836-845 (2003).

88   Guo, L. *et al.* Effect of annealing temperature on the corrosion behavior of duplex stainless steel studied by in situ techniques. *Corrosion Sci.* **53**, 3733-3741 (2011).

89   Bettini, E., Kivisäkk, U., Leygraf, C. & Pan, J. Study of corrosion behavior of a 22% Cr duplex stainless steel: Influence of nano-sized chromium nitrides and exposure temperature. *Electrochim. Acta* **113**, 280-289 (2013).

90   Oernek, C. & Engelberg, D. L. Correlative EBSD and SKPFM characterisation of microstructure development to assist determination of corrosion propensity in grade 2205 duplex stainless steel. *J Mater Sci* **51**, 1931-1948 (2016).

91   Schmutz, P. & Frankel, G. Corrosion Study of AA2024-T3 by Scanning Kelvin Probe Force Microscopy and In Situ Atomic Force Microscopy Scratching. *Journal of the Electrochemical Society* **145**, 2295-2306 (1998).

92   Song, Q. N., Zheng, Y. G., Ni, D. R. & Ma, Z. Y. Studies of the nobility of phases using scanning Kelvin probe microscopy and its relationship to corrosion behaviour of Ni–Al bronze in chloride media. *Corrosion Sci.* **92**, 95-103 (2015).

93   Umeda, J., Nakanishi, N., Kondoh, K. & Imai, H. Surface potential analysis on initial galvanic corrosion of Ti/Mg-Al dissimilar material. *Materials*

Chemistry and Physics **179**, 5-9 (2016).

94   Oprea, A., Bârsan, N. & Weimar, U. Work function changes in gas sensitive materials: Fundamentals and applications. *Sensors and Actuators B: Chemical* **142**, 470-493 (2009).

95   Rezali, F. A. M., Rasid, M. A. S. A., Othman, N. A. F., Hatta, S. W. M. & Soin, N. Work Function Tuning and Doping Optimization of 22-nm HKMG Raised SiGe/SiC Source–Drain FinFETs. *Journal of Electronic Materials* **46**, 1567-1575 (2017).

96   Yoo, G., Hong, S., Heo, J. & Kim, S. Enhanced photoresponsivity of multilayer MoS2 transistors using high work function MoOx overlayer. *Applied Physics Letters* **110**, 053112 (2017).

97   Hossain, M. I. & Aïssa, B. Effect of Structure, Temperature, and Metal Work Function on Performance of Organometallic Perovskite Solar Cells. *Journal of Electronic Materials* **46**, 1806-1810 (2017).

98   Wang, W. *et al.* Solid-Solution Hardening in Mg-Gd-TM (TM = Ag, Zn, and Zr) Alloys: An Integrated Density Functional Theory and Electron Work Function Study. *JOM*, 1-9 (2015).

99   Wang, W. Y. *et al.* Power law scaled hardness of Mn strengthened nanocrystalline AlMn non-equilibrium solid solutions. *Scr. Mater.* **120**, 31-36 (2016).

100   Lu, H. & Li, D. Correlation between the electron work function of metals and their bulk moduli, thermal expansion and heat capacity via the Lennard–Jones potential. *physica status solidi (b)* **251**, 815-820 (2014).

101   Shu, Z. & Davies, G. J. Calculation of the Lennard-Jones N-M Potential-Energy Parameters for Metals. *Physica Status Solidi a-Applied*

Research **78**, 595-605 (1983).

102   Drebushchak, V. A. & Turkin, A. I. Relationship Between Heat Capacity and Thermal Expansion Derived from the Lennard–Jones Potential. *Journal of Thermal Analysis and Calorimetry* **65**, 745-753 (2001).

103   Verlet, L. Computer" experiments" on classical fluids. I. Thermodynamical properties of Lennard-Jones molecules. *Physical Review* **159**, 98 (1967).

104   Kaye, G. W. C. & Laby, T. H. *Tables of physical and chemical constants*. 15 edn,   (Longman, 1993)

105   Eberhart, J. G. & Horner, S. Bond-Energy and Surface-Energy Calculations in Metals. *Journal of Chemical Education* **87**, 608-612 (2010).

106   R, A. & Jesuit.S. Relation of Elastic Modulus to Thermal Expansion Coefficient in Elastic and Viscoelastic Materials, in *SEM Annual Conference & Exposition on Experimental and Applied Mechanics* (2005).

107   Lu, H., Huang, X. & Li, D. Understanding the bond-energy, hardness, and adhesive force from the phase diagram via the electron work function. *Journal of Applied Physics* **116**, 173506 (2014).

108   Sher, A., van Schilfgaarde, M., Chen, A.-B. & Chen, W. Quasichemical approximation in binary alloys. *Physical Review B* **36**, 4279-4295 (1987).

109   Swalin, R. A. *Thermodynamics of Solids*. pp. 141, 172 (John Wiley, 1972).

110   DeHoff, R. T. *Thermodynamics in Materials Science*. pp. 191, 275 (McGraw-Hill, 1993).

111   Frankel, G. *et al.* Potential control under thin aqueous layers using a Kelvin Probe. *Corrosion Sci.* **49**, 2021-2036 (2007).

112   Li, W. & Li, D. Y. Characterization of interfacial bonding using a scanning Kelvin probe. *Journal of Applied Physics* **97**, 014909 (2005).

113   Buckley, D. H. *Surface Effects in Adhesion, Friction, Wear and Lubrication*. Chapter 5 (Elsevier, 1981).

114   Sikorski, M. E. The adhesion of metals and factors that influence it. *Wear* **7**, 144-162 (1964).

115   Lu, H., Hua, G. & Li, D. Dependence of the mechanical behavior of alloys on their electron work function—An alternative parameter for materials design. *Applied Physics Letters* **103**, 261902 (2013).

116   Rothschild, J. A. & Eizenberg, M. Work function calculation of solid solution alloys using the image force model. *Physical Review B* **81**, 224201 (2010).

117   Denton, A. R. & Ashcroft, N. W. Vegard's law. *Physical Review A* **43**, 3161-3164 (1991).

118   Mott, N. F. & Nabarro, F. R. N. An attempt to estimate the degree of precipitation hardening, with a simple model. *Proceedings of the Physical Society* **52**, 86-89 (1940).

119   Mott, N. & Nabarro, F. Report on strength of solids. *Physical Society, London*, 1-19 (1948).

120   Fleischer, R. L. Substitutional solution hardening. *Acta Metallurgica* **11**, 203-209 (1963).

121   Gypen, L. A. & Deruyttere, A. The combination of atomic size and elastic modulus misfit interactions in solid solution hardening. *Scripta Metallurgica* **15**, 815-820 (1981).

122   Fleischer, R. L. Substitutional solid solution hardening of titanium. *Scripta Metallurgica* **21**, 1083-1085 (1987).

123   Harris, B. Solution hardening in niobium. *physica status solidi (b)* **18**,

715-730 (1966).

124 Yasi, J. A., Hector Jr, L. G. & Trinkle, D. R. First-principles data for solid-solution strengthening of magnesium: from geometry and chemistry to properties. *Acta Materialia* **58**, 5704-5713 (2010).

125 Davis, J. R. *Copper and copper alloys*. (ASM international, 2001).

126 Lide, D. Handbook of Chemistry and Physics, (CRC Press, 2005).

127 Čižek, L., Kratochvíl, P. & Smola, B. Solid solution hardening of copper crystals. *J Mater Sci* **9**, 1517-1520 (1974).

128 Akhtar, A. & Teghtsoonian, E. Substitutional solution hardening of magnesium single crystals. *Philos. Mag.* **25**, 897-916 (1972).

129 Lu, H. *et al.* Electron work function–a promising guiding parameter for material design. *Scientific Reports* **6**, 24366 (2016).

130 Kresse, G. & Furthmüller, J. Efficiency of ab-initio total energy calculations for metals and semiconductors using a plane-wave basis set. *Computational Materials Science* **6**, 15-50 (1996).

131 Kresse, G. & Furthmüller, J. Efficient iterative schemes for ab initio total-energy calculations using a plane-wave basis set. *Physical Review B* **54**, 11169 (1996).

132 Kresse, G. & Joubert, D. From ultrasoft pseudopotentials to the projector augmented-wave method. *Physical Review B* **59**, 1758 (1999).

133 Perdew, J. P., Burke, K. & Ernzerhof, M. Generalized Gradient Approximation Made Simple. *Physical Review Letters* **77**, 3865-3868 (1996).

134 Monkhorst, H. J. & Pack, J. D. Special points for Brillouin-zone integrations. *Physical Review B* **13**, 5188 (1976).

135   Ravindran, P. *et al.* Density functional theory for calculation of elastic properties of orthorhombic crystals: application to TiSi 2. *Journal of Applied Physics* **84**, 4891-4904 (1998).

136   Swartzendruber, L. J., Itkin, V. P. & Alcock, C. B. The Fe-Ni (iron-nickel) system. *JPE* **12**, 288-312 (1991).

137   Yang, C. W., Williams, D. B. & Goldstein, J. I. A revision of the Fe-Ni phase diagram at low temperatures (<400 °C). *JPE* **17**, 522-531 (1996).

138   Cacciamani, G. *et al.* Critical evaluation of the Fe–Ni, Fe–Ti and Fe–Ni–Ti alloy systems. *Intermetallics* **14**, 1312-1325 (2006).

139   Cacciamani, G., Dinsdale, A., Palumbo, M. & Pasturel, A. The Fe–Ni system: Thermodynamic modelling assisted by atomistic calculations. *Intermetallics* **18**, 1148-1162 (2010).

140   Howald, R. A. The thermodynamics of tetrataenite and awaruite: A review of the Fe-Ni phase diagram. *Metall and Mat Trans A* **34**, 1759-1769 (2003).

141   Mishin, Y., Mehl, M. J. & Papaconstantopoulos, D. A. Phase stability in the Fe-Ni system: Investigation by first-principles calculations and atomistic simulations. *Acta Materialia* **53**, 4029-4041 (2005).

142   Bando, Y. The formation of superstructure of Fe3Ni in fine particles. *Journal of the Physical Society of Japan* **16**, 2342 (1961).

143   Mohri, T. & Chen, Y. First-principles investigation of L1 0-disorder phase equilibria of Fe–Ni,–Pd, and–Pt binary alloy systems. *Journal of Alloys and Compounds* **383**, 23-31 (2004).

144   Yang, Z., Lu, H., Liu, Z., Yan, X. & Li, D. Effect of particle size on the surface activity of TiC-Ni composite coating via the interfacial valence electron localization. *RSC Advances* **6**, 18793-18799 (2016).

145   Mosleh-Shirazi, S., Hua, G., Akhlaghi, F., Yan, X. & Li, D. Interfacial valence electron localization and the corrosion resistance of Al-SiC nanocomposite. *Scientific Reports* **5**, 18154 (2015).

146   Li, W. & Li, D. Y. Effect of grain size on the electron work function of Cu and Al. *Surf. Rev. Lett.* **11**, 173-178 (2004).

147   Lo, W. J. & Somorjai, G. A. Temperature-dependent surface structure, composition, and electronic properties of the clean SrTiO3 (111) crystal face: Low-energy-electron diffraction, Auger-electron spectroscopy, electron energy loss, and ultraviolet-photoelectron spectroscopy studies. *Physical Review B* **17**, 4942-4950 (1978).

148   Zhu, D. B., Liu, C. M., Han, T., Liu, Y. D. & Xie, H. P. Effects of secondary β and γ phases on the work function properties of Cu–Be alloys. *Appl. Phys. A*, **120**, 1023-1026 (2015).

149   Abbasi, M., Taheri, A. K. & Salehi, M. T. Growth rate of intermetalliccompounds in Al/Cu bimetal produced by cold roll welding process. *J. Alloy and Compd.* **319**, 233-241 (2001).

150   Fedorov, M. I., Prokofeva, L. V., Pshenay-Severin, D. A., A.A.Shabaldin & Konstantinov, P. P. New Interest in Intermetallic Compound ZnSb. *J. Electron.Mater.* **43**, 2314-2319 (2014).

151   T.L.Anderson. *Fracture Mechanics Fundamentals and Applications*. 3 edn, Chapter 2, (CRC Press, Taylor & Francis Group, 2005).

152   Guo, L., Li, M., Zhang, Y. & Ye, F. Improved Toughness and Thermal Expansion of Non-stoichiometry Gd2‒xZr2+xO7+x/2 Ceramics fo r Thermal Barrier Coating Application. *Journal of Materials Science & Technology* **32**, 28-33 (2016).

153   Wang, X. *et al.* Mechanical properties and damage tolerance of bulk Yb 3 Al 5 O 12 ceramic. *Journal of Materials Science & Technology* **31**, 369-374 (2015).

154   Nastic, A. *et al.* Instrumented and Vickers Indentation for the Characterization of Stiffness, Hardness and Toughness of Zirconia Toughened Al 2 O 3 and SiC Armor. *Journal of Materials Science & Technology* **31**, 773-783 (2015).

155   Li, W. & Li, D. Y. Effect of surface geometrical configurations induced by microcracks on the electron work function. *Acta Materialia* **53**, 3871-3878 (2005).

156   Case, E. & Kim, Y. The effect of surface-limited microcracks on the effective Young's modulus of ceramics. *J Mater Sci* **28**, 1885-1900 (1993).

157   Laws, N. & Brockenbrough, J. The effect of micro-crack systems on the loss of stiffness of brittle solids. *International journal of solids and structures* **23**, 1247-1268 (1987).

158   Kachanov, M. Effective Elastic Properties of Cracked Solids: Critical Review of Some Basic Concepts. *Applied Mechanics Reviews* **45**, 304-335 (1992).

159   Chudoba, T., Griepentrog, M., Dück, A., Schneider, D. & Richter, F. Young's modulus measurements on ultra-thin coatings. *Journal of Materials Research* **19**, 301-314 (2004).

160   Musil, J., Kunc, F., Zeman, H. & Poláková, H. Relationships between hardness, Young's modulus and elastic recovery in hard nanocomposite coatings. *Surface and Coatings Technology* **154**, 304-313 (2002).

161   Chiu, C.-C. & Case, E. D. Elastic modulus determination of coating layers

as applied to layered ceramic composites. *Materials Science and Engineering: A* **132**, 39-47 (1991).

162   Case, E. & Glinka, C. Characterization of microcracks in YCrO3 using small-angle neutron scattering and elasticity measurements. *J Mater Sci* **19**, 2962-2968 (1984).

163   Smith, D. T. & Wei, L. Quantifying local microcrack density in ceramics: A comparison of instrumented indentation and thermal wave techniques. *Journal of the American Ceramic Society* **78**, 1301-1304 (1995).

164   Radin, C. Random close packing of granular matter. *Journal of Statistical Physics* **131**, 567-573 (2008).

165   Obraztsov, A. N., Volkov, A. P., Boronin, A. I. & Kosheev, S. V. Defect induced lowering of work function in graphite-like materials. *Diamond and Related Materials* **11**, 813-818 (2002).

166   Ferrante, J. & Smith, J. R. Theory of the bimetallic interface. *Physical Review B* **31**, 3427 (1985).

167   Rose, J. H., Ferrante, J. & Smith, J. R. Universal Binding Energy Curves for Metals and Bimetallic Interfaces. *Physical Review Letters* **47**, 675-678 (1981).

168   Ferrante, J. & Smith, J. R. Theory of metallic adhesion. *Physical Review B* **19**, 3911 (1979).

169   Li, L. & Li, D. Y. Understanding the influence of microstructure features on the erosion resistance of low-carbon pipeline steel through computational simulation. *Wear* **301**, 70-75 (2013).

170   Tsui, B.-Y. & Huang, C.-F. Wide range work function modulation of binary alloys for MOSFET application. *Electron Device Letters, IEEE* **24**, 153-155

(2003).

171   Wang, J. *et al.* Explore the electron work function as a promising indicative parameter for supplementary clues towards tailoring of wear-resistant materials. *Materials Science and Engineering: A* **669**, 396-402 (2016).

172   Scandian, C., Boher, C., de Mello, J. D. B. & Rézaï-Aria, F. Effect of molybdenum and chromium contents in sliding wear of high-chromium white cast iron: The relationship between microstructure and wear. *Wear* **267**, 401-408 (2009).

173   Pellizzari, M., Cescato, D. & De Flora, M. Hot friction and wear behaviour of high speed steel and high chromium iron for rolls. *Wear* **267**, 467-475 (2009).

174   Filipovic, M., Kamberovic, Z., Korac, M. & Gavrilovski, M. Correlation of microstructure with the wear resistance and fracture toughness of white cast iron alloys. *Metals and Materials International* **19**, 473-481 (2013).

175   Tang, X. *et al.* Microstructure of high (45wt.%) chromium cast irons and their resistances to wear and corrosion. *Wear* **271**, 1426-1431 (2011).

176   Petrakov, O. & Poddubnyi, A. Structure of wear-resistant alloyed white irons. *Met Sci Heat Treat* **49**, 409-411 (2007).

177   Coronado, J. Effect of (Fe, Cr) 7 C 3 carbide orientation on abrasion wear resistance and fracture toughness. *Wear* **270**, 287-293 (2011).

178   Archard, J. F. Contact and Rubbing of Flat Surfaces. *Journal of Applied Physics* **24**, 981-988 (1953).

179   Tjong, S. C. & Lau, K. C. Abrasive wear behavior of TiB2 particle-reinforced copper matrix composites. *Materials Science and Engineering: A* **282**, 183-186 (2000).

180 Eberhart, M. E., Latanision, R. M. & Johnson, K. H. Overview no. 44: The chemistry of fracture: A basis for analysis. *Acta Metallurgica* **33**, 1769-1783 (1985).

181 Barinov, S. On brittle-to-ductile transition in covalent diamond-like and ionic rock salt structure solids. *Journal of materials science letters* **16**, 212-214 (1997).

182 Griffiths, D. J. & College, R. *Introduction to electrodynamics*. Vol. 3 (Prentice Hall Upper Saddle River, NJ, 1999).

183 Gilman*, J. Possible role of dispersion forces in fracture. *Philos. Mag.* **85**, 2799-2807 (2005).

184 Hua, Z., An, B., Iijima, T., Gu, C. & Zheng, J. The finding of crystallographic orientation dependence of hydrogen diffusion in austenitic stainless steel by scanning Kelvin probe force microscopy. *Scr. Mater.* **131**, 47-50 (2017).